Quantitative Water Surface Flow Visualization by the Hydraulic Analogy

Ziyaad Arendze

A research report submitted to the Faculty of Engineering and the Built Environment, University of the Witwatersrand, in partial fulfilment of the requirements for the degree of Master of Science in Engineering.

Johannesburg, 2006

Dedicated to my parents,
Faried and Nuzly.

Declaration

I declare that this research report is my own, unaided work. It is being submitted for the degree of Master of Science in the University of the Witwatersrand, Johannesburg. It has not been submitted before for any degree or examination in any other University.

_____

Ziyaad Arendze

_____ day of _____ _____

Abstract

A qualitative and quantitative study of the hydraulic analogy; that is the analogy between flow with a free surface and two dimensional compressible gas flow, is described. The experimentation was done using a water table, and results are compared with Computational Fluid Dynamic (CFD) results for actual free surface flow models, and a fictitious gas model. Different test cases are considered (i) a wedge moving at steady supersonic/supercritical speeds of Froude or Mach number equal to 2.38, 3.12 and 4.31 (ii)unsteady motion of a wedge accelerating to supersonic speeds and then decelerating. Quantitative results for the experimental case are achieved by using a colour encoding slope detection technique. Qualitatively, with respect to wave angles, the fictitious gas case shows the best agreement to the experimental case, but at higher Froude/Mach numbers the free surface models also show good agreement. Quantitatively, with respect to wave location and depth profile, the free surface models show better agreement to the experimental case. For the unsteady case the resulting flow patterns are quite similar for the two cases considered, namely the experimental and free surface CFD cases.

Acknowledgements

I wish to express my appreciation to Professor B.W. Skews, my supervisor, for his guidance and support.

I wish to thank the National Research Foundation (NRF), and also Professor B.W. Skews again, as a grant holder for the aforementioned foundation, for the financial support during this project.

I also wish to thank Mr. Dannie de Kock, from the local FLUENT support team, for his advice on using FLUENT.

Contents

List of Figures

List of Tables

Nomenclature

c_p : specific heat at constant pressure
c_v : specific heat at constant volume
γ : specific heat ratio, ratio of c_p to c_v
T : absolute temperature
ρ : density
p : pressure
h : enthalpy
σ : surface tension
a : speed of sound
v : velocity of flow
d : water depth
M : Mach number
Fr : Froude number
g : acceleration due to gravity
x,y : rectangular coordinate axes
u,v : components of velocity in x-direction and y-direction respectively.
ϕ : velocity potential in two dimensional flow
λ : wavelength of surface waves
c : velocity of propagation of surface waves
β, θ : angle
r : maximum radius of source screen

Subscripts:

No subscript : any value of variable
0 : value at stagnation (v=0)
max : maximum value of variable
x : partial derivative with respect to (w.r.t) x
y : partial derivative w.r.t y

Chapter 1

Introduction

Today, many aircraft are capable of travelling at supersonic speeds. As a result, the study of shock waves interactions has become more important. The interaction between the noise, caused by an aircraft travelling supersonically, and the ground, as well as an aircraft flying close to another aircraft, which is travelling supersonically, is of particular relevance [7]. The testing of shock waves is normally done in a wind tunnel. For unsteady or accelerating motions, however, this cannot be done. This is also a very expensive way of testing, especially if testing is done at speeds greater than Mach one.

For two physical processes to be analogous, the mathematical equations which govern them have to be equivalent. Pairs of analogous quantities may then be defined based on their respective positions in the basic equations. Analogy methods become useful when a physical or mechanical process analogous to a fluid-mechanical problem, generates a visible pattern from which a conclusion may be drawn regarding the flow pattern of the fluid-mechanical problem. This allows the visualization of a certain flow pattern indirectly by means of its physical analogy. An example of such an analogy is the hydraulic analogy, also known by the respective experimental facility as "free surface water table" [9].The hydraulic analogy is the analogy between the shallow flow of a liquid with a free surface and the two-dimensional flow of a compressible gas.

A more cost effective way of simulating shock wave interactions, in terms of time, money and expertise, is by using a water table or ripple tank, for qualitative studies. Qualitatively, many features of gas flow with shock waves, can easily be simulated, as shown in figure (1.1). For many problems, such as unsteady motion, it is the only practical method available. The wave phe-

nomena in water can be often be seen directly, so the need for sophisticated equipment such as high speed schlieren photography, holography and interferometry, needed for wind tunnel and shock tube testing, are not needed [10]. As a result, from a research perspective, it contributes to the assumption of flow patterns, aiding in the development of theoretical solutions for these flow patterns [8]. From an educational perspective, the water table is often used as a tool for the understanding of compressible flows and is often seen in many aerodynamics laboratories [11].

The hydraulic analogy has been known for some time with Mach [12] first commenting on it and the mathematical development by Jouget [13] following a few years later. The analogy has therefore been applied to a wide variety of problems in gas dynamics. (A few examples are discussed in Appendix A.) More recently the focus has shifted to visualization techniques enabling quantitative research to be done. Presently, advances in computer software, namely, in computational fluid dynamics (CFD) software, has enabled shallow water flow to be modelled.

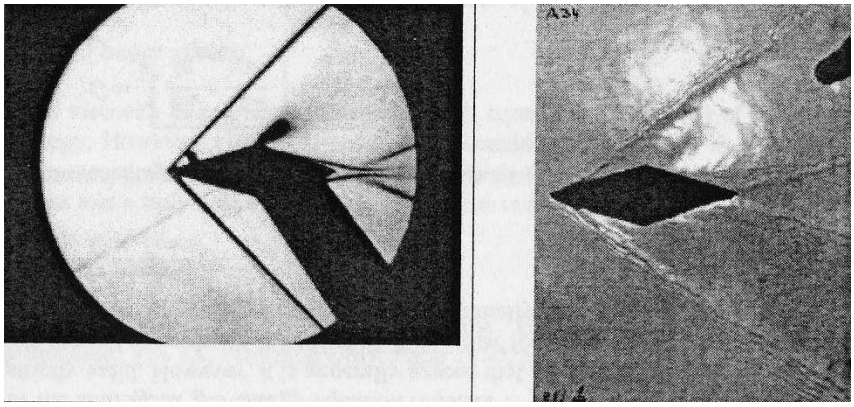

Figure 1.1: A supersonic aerofoil in a wind tunnel (left) and on a water table (right)[6]

Chapter 2

Objectives

- To optimize the optical system of the water table.
- To model the flow in CFD, using FLUENT®, a commercially available general purpose CFD software.
- To compare the CFD results with actual test results.

Chapter 3

Hydraulic Analogy

3.1 Theoretical Background

The mathematical form of the analogy was derived by Jouget [13] and later by Riabouchinsky [14]. The following is a condensation of the theory and mathematical development of the hydraulic analogy as given by Prieswerk [15, 16] and is taken from Orlin et al. [17].

The two assumptions made in the mathematical development are:

1. The flow is irrotational.
2. The vertical accelerations at the free surface are negligible compared to the acceleration due to gravity. The pressure in the fluid at any point therefore only depends on the height of the free surface above that point.

The analogy between the flow of water with a free surface and the flow of a compressible gas may be obtained by setting up the energy equations for each. From the energy equation for water, the velocity is

$$V^2 = 2g(d_0 - d) \tag{3.1}$$

and

$$V_{max} = \sqrt{2gd_0} \tag{3.2}$$

The corresponding equations for a gas are

$$V^2 = 2g(h_0 - h) = 2gc_p(T_0 - T) \tag{3.3}$$

and

$$V_{max} = \sqrt{2gh_0} = \sqrt{2gc_pT_0} \tag{3.4}$$

Therefore, if the ratio V/V_{max} for a gas is equated to V/V_{max} for water,

$$\frac{\rho}{\rho_0} = \frac{d}{d_0} = \frac{T}{T_0} \tag{3.5}$$

or

$$\frac{d}{d_0} = \frac{T}{T_0} \tag{3.6}$$

The equation of continuity for water is

$$\frac{\delta(ud)}{\delta x} + \frac{\delta(vd)}{\delta y} = 0 \tag{3.7}$$

The continuity equation for two-dimensional gas flow is

$$\frac{\delta(u\rho)}{\delta x} + \frac{\delta(v\rho)}{\delta y} = 0 \tag{3.8}$$

From equations 3.7 and 3.8, a further condition to the analogy may be derived

$$\frac{d}{d_0} = \frac{\rho}{\rho_0} \tag{3.9}$$

Since for adiabatic isentropic flow in the gas

$$\frac{\rho}{\rho_0} = \left(\frac{T}{T_0}\right)^{\frac{1}{\gamma-1}} \tag{3.10}$$

where

$$\gamma = \frac{c_p}{c_v} \tag{3.11}$$

i.e. the ratio of specific heat at constant pressure, c_p, to specific heat at constant volume, c_v.

Since, in the analogy, from equations 3.6 and 3.9

$$\frac{\rho}{\rho_0} = \frac{d}{d_0} = \frac{T}{T_0} \tag{3.12}$$

then

$$\frac{T}{T_0} = \left(\frac{T}{T_0}\right)^{\frac{1}{\gamma-1}} \tag{3.13}$$

and therefore the analogy requires that $\gamma = 2$.

From the relation

$$\frac{p}{p_0} = \left(\frac{\rho}{\rho_0}\right)^{\gamma} \tag{3.14}$$

it may be seen that, since $\gamma = 2$,

$$\frac{p}{p_0} = \left(\frac{d}{d_0}\right)^{2} \tag{3.15}$$

The velocity potential for water is given by the equation

$$\phi_{xx}\left(1 - \frac{{\phi_x}^2}{gd}\right) + \phi_{yy}\left(1 - \frac{{\phi_y}^2}{gd}\right) - 2\phi_{xy}\frac{\phi_x\phi_y}{gd} = 0 \tag{3.16}$$

and the corresponding equation for a gas is

$$\phi_{xx}\left(1 - \frac{{\phi_x}^2}{a^2}\right) + \phi_{yy}\left(1 - \frac{{\phi_y}^2}{a^2}\right) - 2\phi_{xy}\frac{\phi_x\phi_y}{a^2} = 0 \tag{3.17}$$

Therefore for identical expressions,

$$\frac{gd}{2gd_0} = \frac{a^2}{2gh_0} \tag{3.18}$$

From equations 3.16 and 3.17 it is seen that the velocity $(gd)^{\frac{1}{2}}$ in the liquid flow corresponds to the speed of sound in the gaseous flow. The value of $(gd)^{\frac{1}{2}}$ is the velocity of propagation of gravity waves, where the wavelengths are large in comparison to the water depth. Under certain conditions, the velocity of the flow in the water may strongly decrease for short distances and the depth

may increase. This is called a hydraulic jump and is analogous to a shock wave in two-dimensional compressible gas flow.

The criterion for the dynamic similarity of the two wave propagations is the ratio of the free stream velocity to the wave propagation velocity [18]. Therefore, for water, from the velocity of wave propagation, $(gd)^{\frac{1}{2}}$, and equation 3.1,

$$\frac{V}{(gd)^{\frac{1}{2}}} = \left(\frac{2(d_0 - d)}{d}\right)^{\frac{1}{2}} = F \tag{3.19}$$

where F is the Froude number.

For a gas,

$$M = \frac{V}{a} \tag{3.20}$$

where M is the Mach number.

The analogy is summarized in table (3.1).

Table 3.1: Summary of the Hydraulic Analogy

Two-Dimensional Gas Flow	Water Flow
Density ratio, $\frac{\rho}{\rho_0}$	Water depth ratio, $\frac{d}{d_0}$
Temperature ratio,$\frac{T}{T_0}$	Water depth ratio, $\frac{d}{d_0}$
Pressure ratio, $\frac{p}{p_0}$	Square of water depth ratio, $\left(\frac{d}{d_0}\right)^2$
Velocity of sound, a	Wave velocity, $(gd)^{\frac{1}{2}}$
Mach number, M	Froude number, F
Shock wave	Hydraulic jump

3.2 Analysis

There were however assumptions made to arrive at this result. These assumptions restrict the application of the analogy for quantitative research.

The analogy applies only to a perfect gas with $\gamma = 2$, and neither air nor any other gas has a specific heat ratio of 2. An inherent assumption that the flow is isentropic is not valid for discontinuities. Actual fluid effects are not

considered in the development of the analogy, and are different for the two types of flow. [8, 19]
The actual propagation velocity of a surface wave in water is given by

$$c = \sqrt{\left(\frac{g\lambda}{2\pi} + \frac{2\pi\sigma}{\rho\lambda}\right) \tanh \frac{2\pi d}{\lambda}} \tag{3.21}$$

If $\sigma = 0$, and $d \ll \lambda$ we can assume that

$$c = \sqrt{gd} \tag{3.22}$$

As mentioned before, this term represents the propagation speed of only the gravity waves. The second term in braces of equation 3.21 represents the smaller capillary waves. The surface wave is however a summation of previous disturbances of all wavelengths. Therefore, not only the big wavelengths can be considered, since the smaller wavelengths make a contribution to the bigger wavelengths. In general the propagation velocity decreases with wavelength, due to the capillary waves, and increase again due to gravity. The height at which the $tanh\ \frac{2\pi d}{\lambda}$ term compensates the height at which the water is rising, can be found though. This would mean that at this height, propagation speed is constant with wavelength, outside the capillary wave region. This height is calculated to be $4.7\,mm$, but it is concluded that a height between $4\,mm$ and $6\,mm$ is acceptable [6] .

Extensive research has been done to determine the optimal height. Black and Mediratta [18] find this height to be $0.5\,inch\,(12.7mm)$ and suggest that a depth of $1\,inch\,(25.4mm)$ should be allowed for when designing a new water channel. Their argument is that at a greater depth, the boundary layer is likely to be proportionally smaller part of the measured depth. Orlin et al. [17] have examined different flow patterns created by the same body at the same Froude number for different depths, varying from $0.5\ inch(12.7mm)$ to $2\,inches\,(50.8mm)$. By comparing these flow patterns to that of a cylinder in a high speed wind tunnel, the best agreement is found to be between $0.75\,inch\,(19.05mm)$ and $1\,inch\,(25.4mm)$.

Laitone [20] suggests that for ordinary tap water, if a height of $0.25\,inch$ ($6.35mm$) is chosen, the wave velocity will be independent of the wavelength, except for the small capillary waves. Shapiro [21] finds the optimal height to be $5mm$. This is also based on the fact that the wave velocity is independent of the wavelength at this height. This was done graphically by observing that the curve of wave speed as a function of wave length, at this height, has only a weak minimum and approaches the horizontal for very short wavelengths. This concept is elaborated on by Gupta [22] and the optimal height from Laitone is found analytically.

Other restrictions which apply to the hydraulic analogy are that it can only be applied to one or two dimensional flows. Certain effects also have no counterpart in the gaseous case. Effects such as bottom flow boundary layers, the periodicity of gravity waves, and that there are two types of hydraulic jumps; undular and regular. The simplicity of the method is also due to the fact that the ratio of velocity of sound in air to the velocity of propagation of gravity waves in shallow water, which are analogous, is a factor of 1000. The transient process is thus slowed downed 1000 times and therefore high speed photographic equipment not necessary. [8, 9]

Chapter 4

Pressures fields due to moving bodies

The following chapter is adapted form Lilley et. al. [7]

4.1 Bodies moving with constant supersonic speed

Consider a body which sends out spherical pulse waves moving at sonic speed. If this body is accelerated from rest to a subsonic speed, the emitted pulse waves will move both upstream and downstream of the body. The waves moving upstream of the body will act as a warning to the air ahead that the body is approaching.

If this body now moves at a constant supersonic speed, the pulse waves which are emitted cannot move upstream of the body, since they are moving at sonic speed; less than that of the body. These pulse waves form envelopes and the surfaces generated are called Mach waves. A Mach wave across which there is an infinitesimal increase in pressure is referred to as a compression wave. An expansion wave is the opposite, with a decrease in pressure across the wave. The angle of the Mach wave relative to the direction of the flow is called the Mach angle. Since the pulses are emitted at sonic speed, the velocity normal to a Mach wave is sonic.

The induced flow over the body cannot be generated by Mach waves only, as finite increases in pressure and changes in direction are required. As a result,

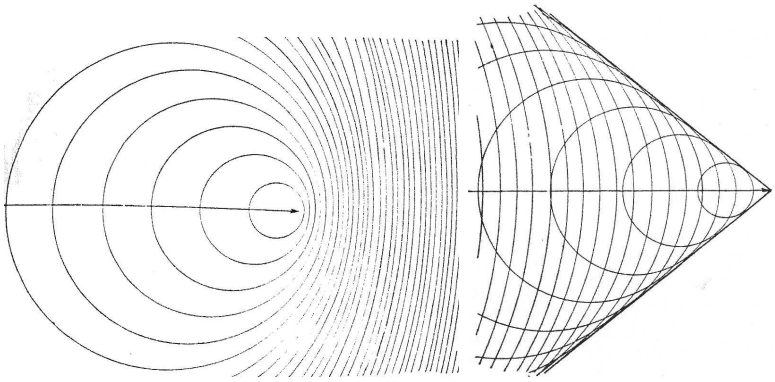

Figure 4.1: Wave patterns for a particle moving at steady subsonic speed [7]

Figure 4.2: Wave patterns for a particle moving at steady supersonic speed [7]

bow waves and tail waves of finite amplitude are found attached to the front and the rear of the body respectively. These are shock waves and can be regarded as envelopes of compression Mach waves. The bow wave is formed ahead of the body and will become attached to the body, only if the nose is sharp. The bow and tail waves formed around a two-dimensional body will be straight only if, the velocity of the body is constant, the body moves in a straight line, and the flow behind the body is supersonic relative to the body. Expansion waves are formed between the bow and tail waves. If the body is curved, it is continuous, and if the body has sharp edges, expansion waves form as a fan from the sharp edges. The interaction of the expansion waves and the shock waves reduces the strength of the shock waves.

4.2 Bodies accelerating or retarding

Continuing with the example of a body emitting spherical pulse waves at sonic speed. Recalling that the velocity normal to the Mach wave is sonic, for an accelerating body, the Mach wave is concave in the direction of motion focusing at the centre of curvature. After this point, the Mach wave curvature becomes convex in the direction of motion. The Mach waves form a closed loop. For a body of finite size, however, the field of flow ahead of it prevents the formation of a concave bow wave. The expected shock formation for a body accelerating from subsonic speed to supersonic speed is a bow wave ahead of, or attached to the nose of the body, separated from the tail wave by expansion waves.

If the body is now retarded to subsonic speeds, the Mach waves form a convex curvature moving forward ahead of the body since the velocity of the Mach waves is now greater than that of the body. The rear Mach wave is also convex and will eventually also move ahead of the body, with the Mach waves again forming a closed loop. The expected shock formation in front of a body retarded from supersonic speed to subsonic speed is also a bow wave ahead of, or attached to the nose of the body, separated from the tail wave by expansion waves.

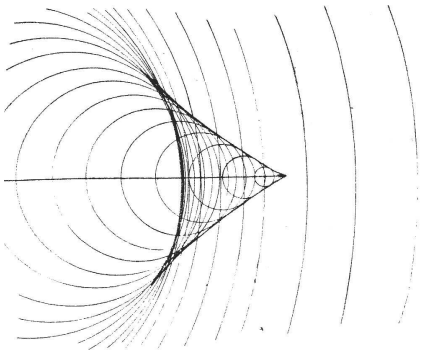

Figure 4.3: Wave patterns for a particle accelerating from subsonic to supersonic speed [7]

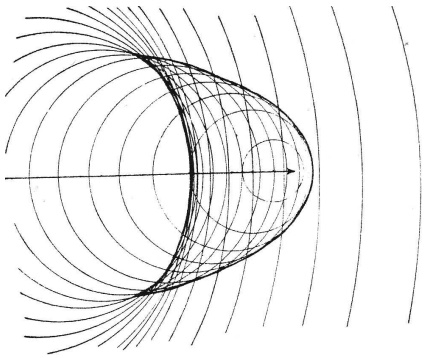

Figure 4.4: Wave patterns for a particle retarding from supersonic to subsonic speed [7]

Chapter 5

Flow Visualization

5.1 Optics Theory

Before the flow visualization techniques can be discussed, a few optical principles are introduced. A description of radiometry (which describes and measures radiation (light) and its interaction with matter) is given in Appendix B.

5.1.1 Reflection [1]

When a beam of light strikes a flat surface, the angle of incidence is the angle made by the incident beam and the normal to the surface. The angle of reflection is the angle the reflected beam makes with the normal to the surface. For flat surfaces, the angle of the incidence and the angle of reflection lie in the same plane with the normal, and the angle of incidence equals the angle of reflection.

5.1.2 Snell's Law/Refraction [1]

When light passes from one medium to another some of the incident light is reflected at the interface between the two mediums, while most of the light passes through into the next medium. If the ray is incident at an angle (other than perpendicular) to a surface, the ray is bent as it enters the new medium. This bending is called refraction. The angle the incident ray makes with the normal is called the angle of incidence and the angle the transmitted beam makes with the normal is called the angle of refraction. The two angles are

related by the following equation,known as Snell's law,

$$n_1 \sin\theta_1 = n_2 \sin\theta_2 \tag{5.1}$$

where n_1 and n_2 are the respective refractive indices of the optical materials. The refractive index of a medium is related to the speed of light in that medium, and when light travels from one medium into another medium, with lower index of refraction (where the speed of light is greater), the ray is bent away from the normal.

5.1.3 Total Internal Reflection [2]

Total internal reflection occurs when light travels from a medium of given index of refraction into another medium of lower index of refraction. The critical angle when total internal reflection occurs is given by

$$\sin\theta_c = \frac{n_1}{n_2} \tag{5.2}$$

where $n_1 > n_2$ and θ_c is the critical angle.

5.1.4 The Fresnel lens [3]

It is well known that the contour of the refracting surface of a conventional lens defines its focusing properties. The bulk of material between the refracting surface has no effect, other than increasing absorption losses, on the optical properties of the lens. In a Fresnel lens, this bulk of material is reduced by extracting a set of coaxial annular cylinders of material. The contour of the curved surface is thus approximated by right circular cylindrical portions, intersected by conical portions called "grooves". The curvature of these "grooves", similar to the conventional lens, is nearly parallel to the plane face at the centre of the lens, and steeper toward the outer edge of the lens. The curvature of these grooves corresponds to the inclination of the original aspheric lens, translated toward the plano surface of the lens, being slightly different to accomadate for this translation, as shown in figure (5.1).

A problem with conventional spherical lenses, is longitudinal spherical aberration. This occurs when different annular sections of the lens bring light rays to focus at different points along the optical axis. The problem is corrected with

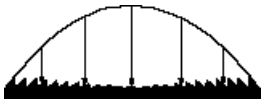

Figure 5.1: The profile of a Fresnel lens opposed to a spherical lens[3]

an aspheric lens, where the contour of the lens is corrected so as to bring all the light rays to focus at a single point on the optical axis. This problem is not encountered with a Fresnel lens, which is made from the beginning with the correct aspheric profile. The thinness of Fresnel lenses also reduces absorption losses and the associated difference in absorption losses occurring across the lens profile.

Unlike commonly used biconvex lenses, with the same curvature on both sides, Fresnel lenses are almost always plano-convex. For a biconvex lens the optical properties are symmetric but a Fresnel lens(a plano-convex lens) shows asymmetric behavior.The correct orientation of the lens is crucial to its performance. The correct orientation of a Fresnel lens is grooves facing toward the collimated beam, and the plano side facing the source. If reversed, the on axis performance of the lens suffers.

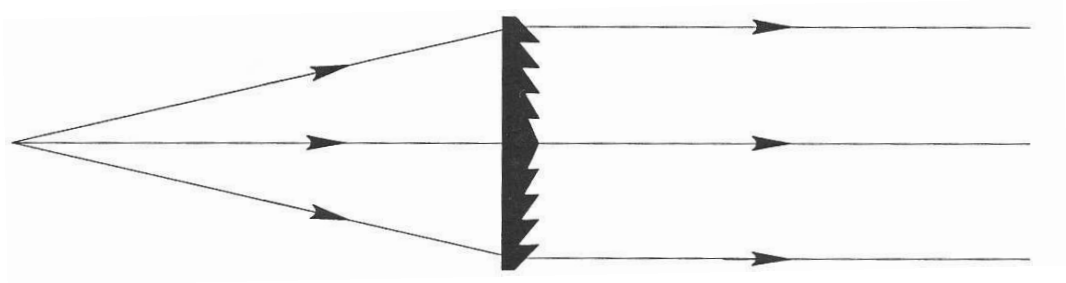

Figure 5.2: A Fresnel lens used to make a collimated beam. [3]

5.1.5 Telecentric Illumination system [4]

A telecentric illumination system is used to convert a radiance distribution into parallel beams. This forms the basis of many surface slope measurement techniques. A light source is put into focus of a large lens (Fresnel lenses are normally used). The rays emitted from a single point at the focal plane, is converted into a parallel beam of light upon passing through the lens. The angle made by this parallel beam is determined by the position on the focal

plane. If the distance from the focal plane is r and the focal length is f, the angle β of propagation of the emmited beam is,

$$\beta = \arctan\left(\frac{r}{f}\right) \tag{5.3}$$

If the radiance of the light source, is isotropic within the cone gathered by the lens, then the parallel beam will have constant intensity emitted for each angle. A spatial variation of the radiance distribution could be represented using colour, by placing the appropriate filter at the focal plane.

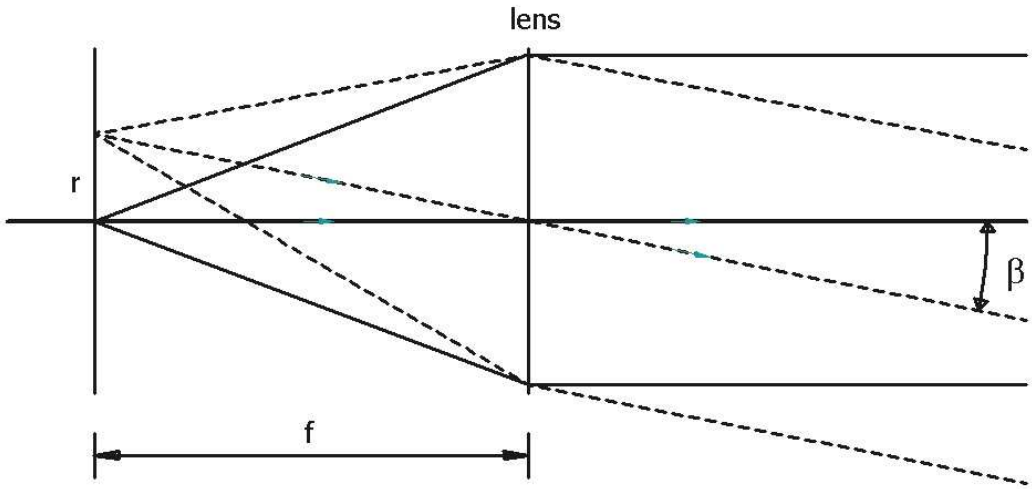

Figure 5.3: The telecentric illumination system

5.2 Flow Visualization Techniques

Matthews [23] has commented on the design of the water channel as an instrument for the investigation of compressible flow phenomena. The comments made about the optical system are given below.

Since the slope of the water surface will bend light, just as a density gradient would bend light in air, the same optical methods may be used for visual observation of the flow. Although the same principles are used, the operational characteristics of the system with the channel can be expected to be different due to the greater bending of light in water. The requirements on the optical system for the water channel is therefore less severe as opposed to the optical system for air. The Schlieren system presents the problem of reducing its sen-

sitivity to such an extent that the range of contrast found in the image will be representative of the entire range of slopes of the water surface. Shadowgraph systems are used instead of Schlieren systems due to their simplicity and lower sensitivity. While shadowgraph and schlieren systems produce quality images for qualitative purposes, they are limited in their capability for quantitative analysis.

Most water table surfaces are made from glass so that diffuse lighting, from an illuminated ground glass screen, beneath the table, is used [11]. The type of visualization technique employed depends on the desired type of tests to be performed, the available facilities, and the model flow speeds. [24]

The quantitative analysis of flow patterns with conventional flow visualization techniques has proven to be difficult. The most basic form of depth measurement is to physically measure the depth, using a contact type gauge or probe. This is the method used by Orlin et al. [17] to determine the depth at which the best agreement is found for the flow around a cylinder in shallow water, and the respective flow in a high speed wind tunnel. Rao [25] uses an electrical contact probe to measure the liquid film thickness, i.e. the depth, for a circular hydraulic jump. A circular hydraulic jump often occurs on a horizontal plate, when a vertical liquid jet impinges on the plate. The resulting flow is a thin film flowing radially outward and at some distance a circular hydraulic jump occurs. In this case, for the initial thin film, the electrical probe is accurate, because the depth is fairly uniform. After the circular hydraulic jump however, waves occur at the surface, which is no longer uniform, so depth measurements with a probe become cumbersome. Readings were thus averaged out over the amplitude of the waves. Therefore, for the measurements of depth at a point, the contact probe is ideal, but for surfaces which are wavy and have large areas, i.e. simultaneous multiple locations in the flow, the probe is not practical. Also for the hydraulic analogy, the flow patterns are of interest, and a probe would disturb the flow by introducing capillary waves.

Depth measurements can also be obtained with non-intrusive optical techniques. An advantage of quantitative flow visualization by optical methods, is that the depth measurement, as well as the flow visualization occur simultaneously and separate apparatus for each is not required. Optical methods are based on the analysis of the optical distortion created at the fluid surface

either by reflection at the surface, or refraction from transmission through the surface. Yamamoto et al. [26] have used inclined grid Moiré topography to visualize water depth distribution. The Moiré grid is placed inclined against the water table above the water surface, with the light source also above the water surface. It therefore operates on the principle of reflection at the water surface. Images are taken for the still water surface, where the grid appears parallel. For the disturbed water surface, there is a deviation from parallel. This deviation of fringes is used to estimate the height of the water surface. A similar technique has been described by Pal [24]. A grid comprising of alternating clear and dark bands is placed beneath the glass sheet of the water table, the table being illuminated from below. This technique is therefore based on refraction at the water surface. For the undisturbed flow the bands appear parallel, but for the disturbed flow there is distortion of the bands. This distortion is said to correspond to an optical prism with its axis placed on the wavefront. No quantitative depth measurements were carried out by Pal, but later Rani [27] used the technique for quantitative studies.

Rani considered three different types of theoretical prisms(isosceles flat-topped, scalene flat-topped and rounded-topped) and inferred the depth from the prism geometry. The flow considered, was flow around a wedge and results were compared with depth gauge measurements. The best agreement with physical measurement was 11% with the round-topped prism. The disadvantage of this technique is that wave surface slope is simplified to fit either one of the prism shapes (which are all symmetrical), and a wavy water surface as a result of a disturbance, is more complicated, comprising different combinations of different slopes.

A large amount of research has also been done on slope sensing of wind-wave interactions, in the field of oceanography. Many of these methods can be adapted for water table studies.

Roesgen et al. [28] have suggested a technique for measuring the surface slope at the air-water interface using a microlens array. The microlens array optically samples the fluid surface at a large number of measurement points in parallel. The image of the lenslet array is recorded by a (Charged Coupled Device) CCD video camera at the focal plane of the lenslet array, producing 4000 data points for each video frame. It works on the principle of a Hartmann-Shack

sensor which is simply an array of lenses to locally sample the slope of incoming waves. A locally collimated beam of light is imaged into the focal plane of the lenslets. The lateral displacement of the images (focal spots) from the optical axis of each lenslet changes when the local angle of incidence changes, and is thus used to determine the surface slope at the wavefront. The surface slope is then integrated to find the local height. The technique is quite accurate, with surface slope variations of less than $10^{-}3$ radians being resolved, with corresponding height variations of less than 10 microns. The area being processed is quite small however, with an area of $20 \times 20mm^2$, and the technique is more suited to the time-resolved imaging of capillary wave dynamics, rather than gravity waves. This area is limited by the size of the CCD chip in the CCD camera.

Another oceanographic technique, also based on the deflection of a collimated beam passing through the water surface, has been developed by Zhang and Cox [29]. A camera is placed vertically far above the water surface such that it only receives vertical rays passing through the water surface from a source below. The source is a translucent coloured screen placed below, and at the focal length of a large lens, all beneath the water surface. Each slope therefore has a specific colour from one point of origin on the colour screen. With a two-dimensional colour screen the gradient of the entire surface slope in the field of view of the camera can be detected. It is the adaption of this technique, which has led to the development of the colour encoded flow visualization technique. This is the technique employed to the water table used for this research project.

5.3 The colour encoded visualization technique applied to the hydraulic analogy

This technique by Zhang and Cox has been applied by Skews [11] to the water table. Instead of the light source and lens being underwater, the light source and lens are now placed beneath the glass surface of the water table; with the water flowing over the glass surface. The technique is also fundamentally similar to the two-dimensional schlieren system, where colour is used to indicate the direction of the gradient. The main advantage of this technique over the techniques mentioned above is that the gradient of the entire surface is accurately defined since one colour represents one slope. Thus each pixel in

the image could give details about the slope at that pixel depending on the colour there.

A camera is placed far above the water surface, so that only vertical rays enter the camera after passing through the water surface. The table is illuminated from below. A diffusely transmitting colour mask is uniformly illuminated from below, and at each point on the source, a cone of light rays of specific colour is generated. A lens is placed at its focal distance from the source, illuminating the entire lens area. After passing through the lens, i.e. being refracted, the rays become collimated into a beam of parallel rays which passes through the glass base of the water table toward the water surface. This is essentially a telecentric illumination system. The angle of propagation of this broad beam depends on the location from the optical axis at the source. If colours vary along these locations from the optical axis, a multitude of different colours will be generated, all at different angles when passing through the lens. Therefore a particular slope is encoded by a particular colour. This light is again refracted by the water surface, but only waves of a certain slope will refract the rays vertically toward the camera. There is therefore a unique one-to-one relationship between the water slope and the angle of approach of an incident beam.

This process is illustrated diagrammatically in figure (5.4) If the colour is blue at the optical axis a collimated beam of blue light is created, which will only enter the camera if the water surface slope is zero. Thus the blue ray AB will be bent away from the camera at the water surface, whereas the blue rays AC and AD which originate from the same point at the source will pass into the camera since the water slope is zero where these rays pass through the surface. The same applies to the green rays EF and EG. The ray EG is refracted by the water surface into the camera, while the ray EF passes through a point where the water slope is zero (i.e. not being refracted), passing straight through the surface and bypassing the camera. Recalling that the distance between the camera and the water surface is large, any slight deviation of a ray from being emmited vertically, will bypass the camera.

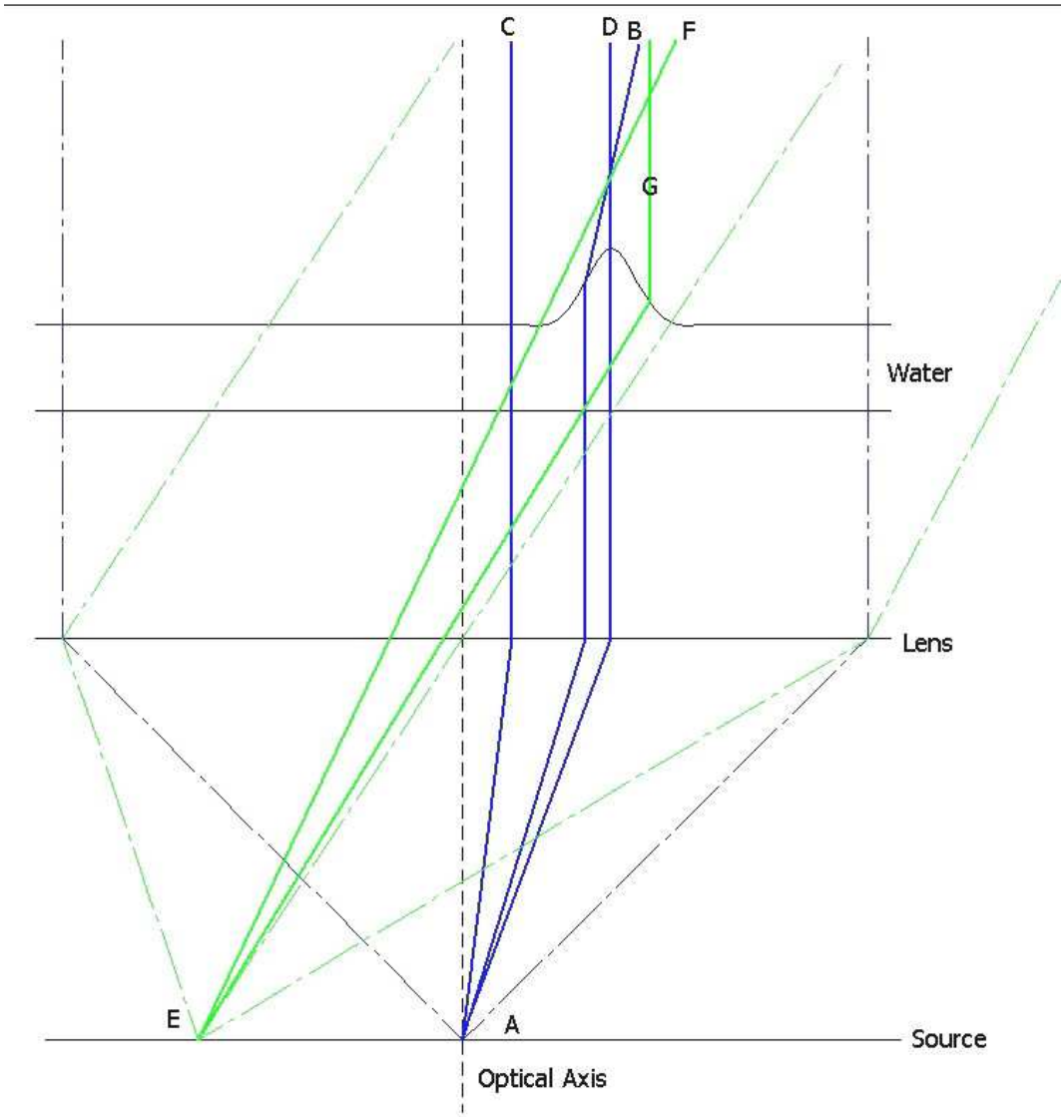

Figure 5.4: The optical principle

Chapter 6

Computational Fluid Dynamics

6.1 Introduction

The properties of any fluid flow is governed by three fundamental principles: conservation of mass, Newton's second law ($F = ma$), and conservation of energy. The equations describing these principles, are either partial differential equations or integral equations. The equations can be represented in discretized algebraic form, which can be solved to obtain approximate flow field values at discrete points in time and/or space. Computational fluid dynamics is the term describing this process, the result of which is a set of numbers as opposed to a closed form analytical solution. Just as the accuracy of experimental data depends on the quality of the tools used, so too the accuracy of a numerical solution is dependent on the quality of the discretization scheme used. [30, 31]

A critical factor in the growth of CFD has been the rapid advancement of high performance computing. CFD is an iterative process, with repetitive manipulation of numbers, which is impossible to do without the aid of a computer. The advancement of computer hardware relates to the complexity and detail of problems solved in CFD, with restrictions due to storage and execution speed.

CFD has become the third approach in the field of fluid dynamics, the other two approaches being theoretical and experimental fluid dynamics. CFD is not a substitute for these two approaches, but rather an aid in interpreting results from the other approaches, and vice-versa.

We now consider CFD applied to free surface flows. [5]

Many engineering problems exist that require accurate simulation of free surface waves. External examples are ship generated waves, wind generated and current-driven waves and waves and loads on coastal and offshore structures. An internal example is that of tank sloshing.

The primary methods of examining free surface flows has been experimental. Experimentally, stationary model tests is one of the most important and reliable methods of examining free surface flows, producing valuable information on the characteristics of this type of flow. In many situations though, it becomes difficult and costly do so. Recently, with the advent of powerful computers, analytical methods have become more important in examining free surface flows. The interest from the CFD community in free surface wave flow, in the fields of hydraulics and naval hydrodynamics, has helped broaden the applicability of analytical methods.

6.2 Solution methods for free surface waves [5]

Two types of free surface wave solution methods currently exist for the Navier-Stokes equations, (shown in Appendix C); interface tracking and interface capturing.

Interface tracking methods track the free surface by satisfying the kinematic condition and conform the grid to the interface at every time step or interval. When the grid has been conformed the Navier-Stokes equations are solved using the dynamic free surface boundary conditions at the free surface. These methods are less computationally demanding, and accurately predict the free surface. The limitations to these methods however, are that highly distorted and breaking waves cannot be solved. Sometimes it is difficult to conform a complex geometry, and grid quality could deteriorate when the grid is conformed.

Interface capturing methods capture the free-surface using one of the following methods. The marker-and-cell (MAC) method [32], captures the free surface in the domain, by tracking markers in the domain. The volume of fluid (VOF) method [33], solves a hyperbolic equation for the volume fraction. Lastly, the

level set method [34], solves for the distance from the free surface. All these methods can be used for highly distorted or breaking waves, as there is no need for grid conforming. Grid quality is thus maintained, although the method is computationally intensive. The resolution of the surface at the interface is very much dependent on the resolution of the grid at the interface, as well as the interpolation scheme used to calculate the face fluxes for the hyperbolic equations. Interface capturing methods are therefore widely used due their applicability to most free surface flow problems.

6.3 Volume of Fluid Method

The VOF technique is the interface capturing method used in FLUENT, to solve the free surface wave solution. The VOF technique is simple to implement, and provided that proper numerical techniques are used for the interface resolution and conservation of mass, momentum, and energy; the method is accurate at describing essential flow features around the free surface. It is also possible to model mass and heat transfer through the interface using the VOF method. [5]

Below is a description of the volume of fluid method taken from the FLUENT documentation. [35]

The basis of the VOF model is that two or more phases are discrete, thus not interpenetrating. Each additional phase added introduces a new variable, the volume fraction of the phase in the computational cell. In each cell, the sum of the volume fractions of all phases add up to one. The fields of all variables and properties are shared by the phases and are volume-averaged values, provided the volume fraction of each phase is known at each location. At any location in the domain, these values would either be representative of one phase, of a combination of phases, depending on the volume fraction at that location. Therefore if the q^{th} fluid has a volume fraction of α_q; if α_q=0 the cell does not contain the q^{th} fluid, if α_q=1 the cell only contains the q^{th} fluid, and if $0 < \alpha_q < 1$ the interface between the q^{th} fluid and one or more other fluids exists in that cell. All properties and variables for each cell are determined from the respective value of α_q there.

The tracking of the interface(s) between phases is done by solving the continuity equation for α_q of one or more phases. For the q^{th} phase, and considering the case of no mass transfer, this equation is

$$\frac{\partial \alpha_q}{\partial t} + \nabla \cdot \alpha_q \vec{v}_q = 0 \tag{6.1}$$

where $\vec{v}_q$ is the velocity vector of the q^{th} fluid.
This equation is not solved for the primary phase, with the primary phase volume fraction based on the following condition,

$$\sum_{q=1}^{n} \alpha_q = 1 \tag{6.2}$$

The fluid properties are determined in a similar manner. Using density as an example, for an n-phase system, the volume fraction average density is

$$\rho = \sum \alpha_q \rho_q \tag{6.3}$$

A single momentum equation is solved throughout the domain, and the resulting velocity field is shared between the phases. The volume fraction is represented by the properties of density, ρ and viscosity, μ in the momentum equation, given below,

$$\frac{\partial}{\partial t}(\rho \vec{v}) + \nabla \cdot (\rho \vec{v} \vec{v}) = -\nabla p + \nabla \cdot \left[\mu\left(\nabla \vec{v} + \nabla \vec{v}^{\,T}\right)\right] + \rho \vec{g} + \vec{F} \tag{6.4}$$

where $\vec{F}$ is the external body forces.
A limitation to the shared-fields approximation is when large velocity differences exist between phases, the velocities at the interface may not be accurate. The same approach is used for the energy equation, which is also shared between phases.

$$\frac{\partial}{\partial t}(\rho E) + \nabla \cdot (\rho E + p) = \nabla \cdot (k_{eff} \nabla T) + S_h \tag{6.5}$$

where k_{eff} is the effective thermal conductivity (also shared among phases), S_h is the contribution from radiation and other heat sources; and the temper-

ature,T, and the energy, E, are treated as mass-averaged variables,

$$E = \frac{\sum_{q=1}^{n} \alpha_q \rho_q E_q}{\sum_{q=1}^{n} \alpha_q \rho_q} \tag{6.6}$$

where E_q is based on the specific heat of that phase and the shared temperature, T.

6.3.1 Interpolation near the interface

Interpolation near the interface requires the calculation of face fluxes for the VOF model. Four schemes are available in FLUENT to do this, the donor acceptor, geometric reconstruction, Euler explicit, and implicit.

For the donor acceptor and geometric reconstruction schemes, standard interpolation techniques are used by FLUENT to obtain the face fluxes when a cell is completely filled with one of the phases. With the donor acceptor scheme, when the cell is near the interface between phases, one cell is a donor of an amount of fluid from one phase and the neighboring cell is an acceptor of the same amount of fluid. The amount of fluid that is transferred is determined from either the filled volume of the donor cell, or the free volume of the acceptor cell.

With the geometric reconstruction scheme, the interface between phases is represented using a piecewise-linear approach. It assumes that the interface is linear in each cell and uses the linear shape to determine the amount of fluid to be transferred between cells.

The Euler explicit scheme uses standard finite-difference interpolation schemes applied to the volume fraction values computed in the previous time step.

$$\frac{\alpha_q^{n+1}\rho_q^{n+1} - \alpha_q^n \rho_q^n}{\triangle t} V + \sum_f (\alpha_{q,f}^n \rho_q U_f^n) = \left[\sum_{p=1}^{n} (\dot{m}_{pq} - \dot{m}_{qp}) + S_{\alpha_q} \right] V \tag{6.7}$$

where $n + 1$ = index for new (current) time step

n = index for previous time step
$\alpha_{q,f}$ = face value of q_{th} volume fraction
V = volume of cell
U_f = volume flux through cell face, based on normal velocity

The implicit interpolation scheme, uses standard finite-difference interpolation schemes and standard scalar transport equations to obtain the volume fraction values at the current time step, as opposed to the previous time step with the Euler explicit scheme.

$$\frac{\alpha_q^{n+1}\rho_q^{n+1} - \alpha_q^n \rho_q^n}{\triangle t} V + \sum_f (\alpha_{q,f}^{n+1} \rho_q^{n+1} U_f^{n+1}) = \left[S_{\alpha_q} + \sum_{p=1}^{n} (\dot{m}_{pq} - \dot{m}_{qp}) \right] V \quad (6.8)$$

6.3.2 Surface Tension and Wall Adhesion

The VOF model in FLUENT allows the effects of surface tension and wall adhesion to be included.

Surface tension arises due to the attractive forces between molecules in a fluid. Consider a liquid in equilibrium with a gas. Intermolecular interactions in a liquid lower the internal energy. Molecules in the bulk of the liquid phase have more attractions since they are entirely surrounded by other liquid phase molecules. Molecules at the surface of the liquid experience fewer attractions, since they essentially do not have a layer of liquid molecules above them, rather the gas. As a result they have a higher internal energy as opposed to molecules in the bulk of the liquid phase. The concentration of gaseous molecules is much lower than the liquid phase molecules, such that interactions between these molecules and the liquid phase molecules at the surface can be ignored. Work is required to increase the area of the liquid-gas interface, since there would then be fewer molecules in the bulk of the liquid phase, and more at the surface layer. Due to this reason, systems tend to assume a configuration of minimum surface area. This is why a drop of liquid is spherical, since a sphere has the lowest ratio of surface area to volume.

If A is the area of the interface between phases α and β, the number of molecules at the interface is proportional to A. If A is reversibly increased by dA, the work needed to do so is also proportional to dA. If the constant of proportionality is $\sigma^{\alpha\beta}$, where subscripts indicate that this constant is dependent on

the phases, the reversible work needed to increase the interface area is $\sigma^{\alpha\beta}dA$. The quantity $\sigma^{\alpha\beta}$ is called the surface tension. [36] There are three methods of specifying the surface tension in Fluent: (i) as a constant, (ii) as a function of temperature and (iii) as a user defined function.

Wall adhesion arises due the relative magnitudes of the adhesive forces between the liquid and the solid, as well as the internal cohesive forces of the liquid. Wall adhesion effects can be included in Fluent by specifying the contact angle, $\theta_{contact}$ which is the angle between the wall and the tangent to the interface at the wall.

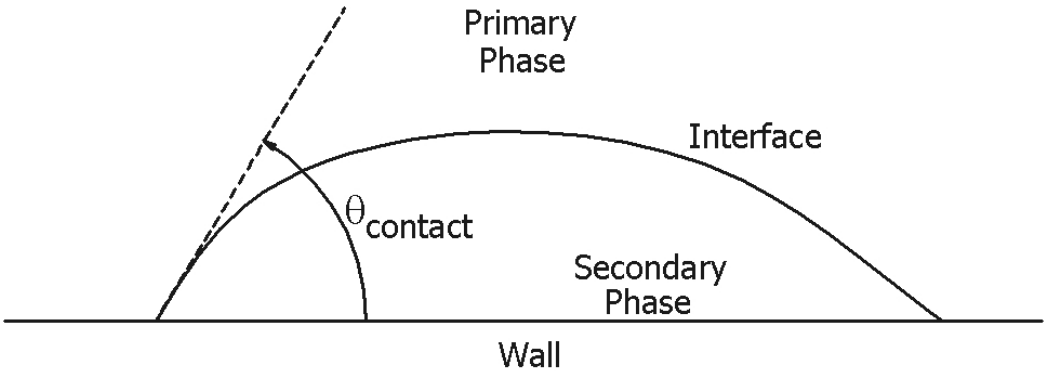

Figure 6.1: The contact angle

6.4 Dynamic Meshing

FLUENT allows the flow within moving and deforming domains to be modelled. Many methods are available in FLUENT, but the method most suited to the case of an accelerated then retarded wedge, is the dynamic mesh model. The dynamic mesh model can be used to model flows where the shape of the domain is changing with time due to motion of the domain boundaries. It is therefore applicable to rigid bodies which move with respect each other. Furthermore, different update methods exist, to update the volume mesh in the deforming regions subject to the motion defined at the boundaries. The update method most suited to our case is the dynamic layering method. A description of this method, as given in the FLUENT documentation [35] is given below.

6.4.1 Dynamic Layering Method

The dynamic layering method is used in cases where the motion is entirely linear. In prismatic (hexahedral and/or wedge) mesh zones, dynamic layering is used to create or remove layers of cells adjacent to a moving boundary. This is done based on the height of the cells in the layer adjacent to the moving surface. The dynamic mesh model in FLUENT allows you to specify an ideal layer height on each moving boundary. Based on this ideal height, the layer of cells adjacent to the moving boundary are either split or merged with the layer of cells next to it.

The factors for splitting and collapsing are specified first. The following criteria are then used to determine whether the cell layer adjacent to the moving boundary, should be split or merged with the layer of cells next to it.

- The cell layer is split if the cell height, h, is

$$h > (1 + \alpha_s)h_{ideal} \tag{6.9}$$

- The cell layer is merged if the cell height, h, is

$$h < \alpha_c h_{ideal} \tag{6.10}$$

where α_s is the split factor
α_c is the collapse factor
h_{ideal} is the ideal layer height.

There are two options for doing dynamic layering, constant height and constant ratio. With the constant height option, the cells are split to create a layer of cells with constant height h_{ideal} and a layer of cells of height $h - h_{ideal}$. With the constant ratio option, the cells are split such that locally, the ratio of the new cell heights is exactly α_s everywhere.

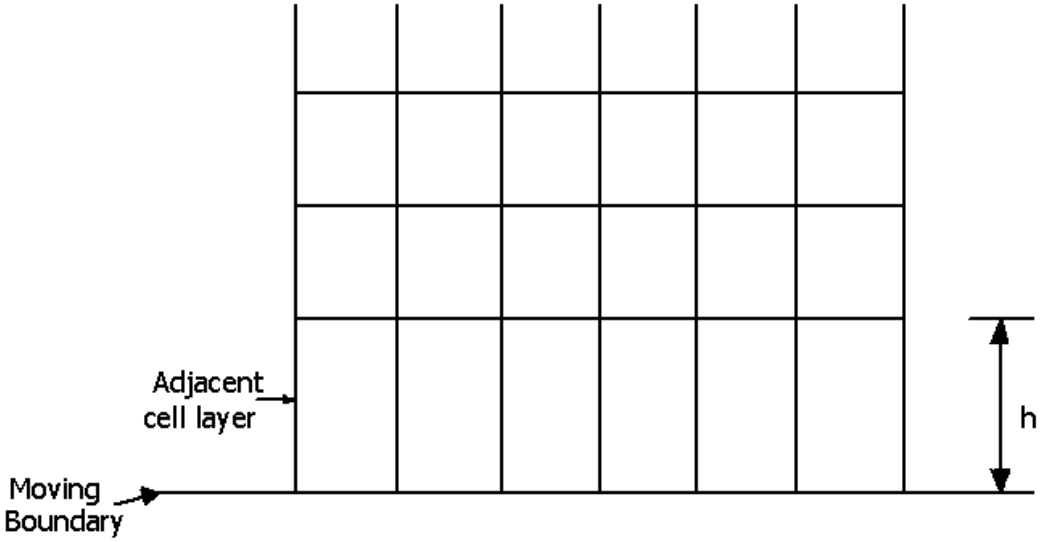

Figure 6.2: Dynamic Layering

Chapter 7

Experimental Facilities

7.1 Water Table

The water table consists of a slab of glass ($1.97\,m \times 1.5\,m$), over which water flows. The water table also consists of the following components:

- 5 water pumps
- a reservoir
- pipes
- a settling chamber
- a collection channel
- a water barrel

The total dimensions of the water table, including the collection chamber is $3.73\,m \times 1.51\,m$. Water is pumped from the reservoir into the settling chamber. An inlet valve is positioned before the settling chamber. Aluminium honeycomb core is used to settle the flow in the settling chamber. From the settling chamber the water flows over the glass slab. Test models are placed on the glass slab. Water flows downstream into the collection channel, where it flows back to the reservoir. This particular set up is for a stationary test model placed in the flow, which is referred to as static testing. Dynamic testing involves a model moving in stationary water. The terms static and dynamic refer to the wedge, and the flow would be the opposite.

For static testing, the speed of the water (and hence the Froude number) can be changed in two ways. The first way is to vary the number of pumps being

used to pump the water from the reservoir. The more pumps used, the greater the flow rate and hence the greater the speed of the water. The second way is to vary the angle of the table. The table is pivoted, and the table can be tilted by loosening two bolts, one on either side, downstream of the table. The table can then be adjusted to the desired tilt angle by using the scissor jack situated beneath the table. The jack is positioned at the downstream end of the table in the middle (across the width) of the table. The jack prevents the table from tilting forward and can be used to jack up the table to the desired angle. Once the table is at the desired angle the bolts should be fastened.

There was no referencing system for the table inclination. This is cumbersome, for when a specific Froude number is desired, and the table has to be jacked up or down a few times before the desired Froude number is achieved. To overcome this problem, a piece of masking tape, with measurements marked on it using a ruler, was fixed to the collection channel. The datum is at the base of the collection channel. The support, which rests on the jack, is then used to indicate the height of the table. This gives some estimate of the table inclination, and hence the adjustments required to obtain a desired Froude

Figure 7.1: The water table facility

number. Having a data set of inclinations with corresponding Froude numbers (see Appendix D) will simplify the experimental testing for future tests.

Figure 7.2: The masking tape marked with measurements fixed to the collection chamber

The angle of inclination of the table transverse to the direction of flow, can also be adjusted. This is done by adjusting a large thread and screw situated in the middle of (the length) of the table. Initially this was another method of adjusting the tilt of the table, but because the thread and screw is positioned on one side of the table only, the table tends to tilt toward the side where the thread and screw is positioned. The thread and screw is useful for correcting different tilt angles on either side of the table to achieve a uniform flow over the table.

Dynamic testing is also done on the water table, where the water on the glass is stationary. The water is sealed off using a removable rectangular perspex plate, which can be mounted to the table at the downstream end. It is positioned just upstream of the collection channel preventing the water from flowing into the collection channel. The plate is mounted on bolts, which are permanently fixed to the table, with butterfly nuts.

A rail and pulley system is used for dynamic testing. This system has to be placed on the table for dynamic testing. It fits into a slot at the upstream end of the table, above the reservoir. This slot spans the width of the table. At

the downstream end of the table the system rests on a piece of wood; which is placed on a metal plate, that is bolted to two beams. The two beams are hollow rectangular steel tubing welded to the sides of the table and span the width of the table.

7.2 Optical System

The optical system comprises of the following:

- a light source (comprising a maximum of four 100W incandescent light bulbs)
- a ground glass screen
- a short focal length Fresnel lens which rests on a sheet of glass 6mm thick
- colour mask (colour filter)
- 5 mirrors

The water table is illuminated from below. The light source is situated on the ground, above a mirror. Directly above the light source is a ground glass screen. This arrangement is positioned under the table. After passing through the lens the light passes through the slab of glass of the table, through the water and into the first mirror. The light gets reflected through a maximum of four more mirrors before entering the camera.

The lens used is an Edmond Optics, $35\,inch\,(889\,mm)$ diameter, Fresnel lens. The focal length is $30\,inches\,(762\,mm)$, the refractive index of the lens material is 1.49, the lens is $\frac{1}{8}\,inch\,(3.175\,mm)$ thick and has 50 grooves per inch.

The colour mask is made from concentric bands (rings) of cellophane sheets of different colour. Each band has a uniform thickness. The largest ring of the mask has a radius which is limited to the size of the ground glass screen. Since the ground glass screen is square and the colour mask is circular, the region between the edge of the ground glass screen and the largest colour band, is blocked out with black cardboard. All the colour bands and the black cardboard are stuck to a transparent sheet of plastic using clear cellophane tape, making the colour mask easier to move and colour bands positions consistent.

Figure 7.3: The Fresnel lens situated beneath the water table

Figure 7.4: The colour mask

7.3 Camera

The components of the camera and their respective functions are [4]:

- A lens to collect the appropriate type of radiation emitted from an object of interest, to form an image of the real object.
- A semiconductor device (charged coupled device, CCD) which converts the irradiance (see Appendix B) at the image plane to an electrical signal.

The camera used was a CCD camera, with a 300 mm, 1:5,5 Cosmicar television lens. The image is focused into the camera from the last mirror.

Figure 7.5: The camera

7.4 Image Capturing Equipment

The purpose of a frame grabber is to convert an electric signal from the camera into a digital image that can be processed on a personal computer. [4] The camera is connected to two video machines and a monitor. A computer, with a separate monitor, is connected to one of the video machines through the input port of the video card installed in the computer. This enables still images, as well as video clips to be captured and stored on the hard drive of the computer. Wincam® software was used to capture the images and video clips. This software also allowed for live footage to be shown on the computer. The advantage being that for stationary test cases, the images can be saved directly on the computer, and do not have to be recorded on video first, as would be the case for dynamic tests. Dynamic tests have to be recorded on video first, due to the delay from the computer when capturing live video footage.

Figure 7.6: The image capturing equipment

7.5 Test Model

An aluminium wedge was used for the tests. The wedge has a 20° apex angle, a chord of 116,7 mm and a thickness of 30 mm.

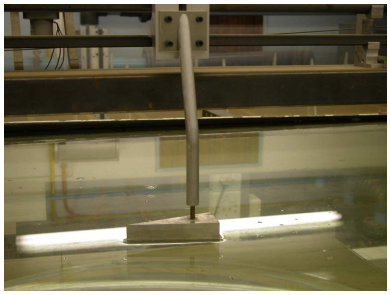

Figure 7.7: The wedge model

7.6 Measuring Apparatus

A micrometer depth gauge was used to measure the depth of the water to an accuracy of $\pm 0.02\,mm$. The gauge is mounted on a steel plate, which is in turn mounted on two wedges on either side of the plate. The system is arranged such that the axis of symmetry of the wedges is parallel to the flow, and the flow direction is from the leading edge to the trailing edge of the wedge. The probe of the gauge is then lowered into the flow and upon touching the water surface, the water depth can be read off.

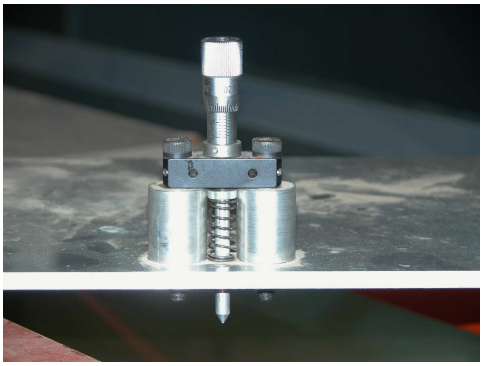

Figure 7.8: The micrometer depth gauge

A stopwatch and measuring tape was used for determining the velocity of the flow.

Chapter 8

Experimental Procedure

8.1 Stationary Wedge/Static Testing

Before setting up, it is important to know what range of Froude numbers are to be investigated. Higher Froude numbers would require the table to be at larger inclinations. When increasing the inclination of the table, it is recommended to do so when the settling chamber is empty. The settling chamber is emptied by opening the inlet valve when the pumps are switched off. The water in the reservoir is at a higher elevation than the water barrel, therefore the water will flow back into the water barrel.

Since the table is pivoted, the torque, from the weight of the water in the settling chamber, would have to be overcome first, before the table inclination can be increased. When decreasing the inclination of the table, this torque aids in jacking up the table, although at times the table may move to a higher inclination than desired, and the table would have to be moved down again. Once the table is at the desired inclination, the two bolts, one on either side of the table are tightened, securing the table in that position.

The inlet valve is then opened, and the desired number of pumps can be turned on. Once the flow is steady, the water depth is measured using the micrometer depth gauge. For minor adjustments to the flow, the inlet valve can be partially closed to control the flow rate. Situations where this is useful, is when a Froude number close to 1, or a specific water depth is desired. If a specific height is desired, the flow should reach steady state first before a depth reading can be taken.

The velocity readings can then be computed and a Froude number can be calculated. The velocity readings were computed by measuring the time it takes a small floating polystyrene object to cover a distance of $1\,m$ in the flow. This distance was marked off on either side of the table and a piece of string was fastened span wise across the table (i.e. perpendicular to the flow). This enables time readings to be taken regardless of the span wise location of the floating object in the flow, noting that the flow is largely one-dimensional. The average of ten time readings were used for the velocity computation.

The light source, camera and image capturing equipment should be switched on. Finally the wedge is placed in the flow, and the resulting image can be captured and saved on the computer hard drive.

8.2 Moving Wedge/Dynamic Testing

The table should be adjusted to be horizontal. A spirit level is useful for determining when the table is horizontal. The table is sealed off by fixing the rectangular perspex plate at the downstream end of the table. The rail system is then placed on the table. The pumps are then switched on to allow the table to be covered with a layer of water. The inlet valve should be closed so as to maintain a constant water depth.

To avoid an overflow on the table, the pumps should be switched off before the desired water depth has been reached. A small valve situated at the downstream end, beneath the table, allows water to flow out from the table. The flow rate from the valve is much lower than when the table fills up. This valve is also used for minor adjustments in water depth. The last option for clearing water from the table is to leave the inlet valve open after switching the pumps off to empty the settling chamber.

The wedge model is now mounted on the rail and pulley system. It is advisable to eliminate all external light sources when doing dynamic testing. Since the field of view is larger than the static case, there would be better contrast with external light sources eliminated, making the waves easier to see.

Chapter 9

Analysis

9.1 Optical System

Optimizing the optical system means finding the source of interference present in images obtained from the water table. The optical system was analysed with a geometrical optical analysis, using ray tracing. A single ray is isolated, and the path it follows upon passing through the entire system, starting from the source until exiting the water surface, is found. As explained earlier in the colour encoded flow visualization technique, only a ray being emitted vertically would enter the camera, so an analysis between the water surface through the mirrors and into the camera, is not necessary.

An important factor, influencing the entire system, hence the analysis, had to be determined first. This was the focal length of the Fresnel lens. The focal length of the lens was found by focusing rays of light from the sun, and measuring the focal length. Rays from the sun can be assumed to be parallel, due to the large distance between the sun and the earth, creating the perfect collimated beam of light. This was done at midday, when the sun is at its zenith. The focal length was found to be $784\,mm$ as opposed to $762\,mm$ given by the manufacturer of the lens. A focal length of $784\,mm$ was used in all subsequent analysis.

Starting with a point at the source, from the telecentric illumination system theory, the distance of this point from the optical axis will determine the angle between the ray and the optical axis when the ray exits the lens. From equation (5.3), this angle is,

$$\beta = \arctan\left(\frac{r}{f}\right)$$

The size of the source, determines the maximum angle β can be. For this system, the maximum radius on the source screen is $r = 450\,mm$ and the focal length of the lens is $784\,mm$. Substituting values for the system, this angle is calculated to be 29.98°.

After passing through the lens the ray propagates, through air, toward the glass surface. Applying Snell's law at the air-glass interface, the angle of the ray, to the normal, in the glass is found.

$$n_2 \sin\theta_1 = n_1 \sin\beta \tag{9.1}$$

therefore

$$\theta_1 = \arcsin\left(\frac{n_1}{n_2}\sin\beta\right) \tag{9.2}$$

where n_1 and n_2 are the refractive indices of air and glass respectively.

With the ray still in the glass, it propagates toward the water surface. Applying Snell's law at the glass-water interface, the angle of the ray to the normal, in the layer of water is found.

$$n_3 \sin\theta_2 = n_2 \sin\theta_1 \tag{9.3}$$

therefore

$$\theta_2 = \arcsin\left(\frac{n_2}{n_3}\sin\theta_1\right) \tag{9.4}$$

where n_3 is the refractive index of water.

The ray is now in the water, and propagating toward the water surface. The angle at which the ray is emitted, is now also dependent on the slope of the water, which is not always plane, as the other surfaces. The normal to a plane surface is perpendicular to it, so for a sloping surface, a line perpendicular to the tangent at the point of interest, would be the normal at that point. The incidence angle is measured from this normal. The angle of the ray when exiting the water surface is found by applying Snell's law at the water-air interface.

$$n_1 \sin\theta_3 = n_3 \sin\acute{\theta_2} \tag{9.5}$$

where

$$\acute{\theta_2} = \theta_2 - \theta_w \tag{9.6}$$

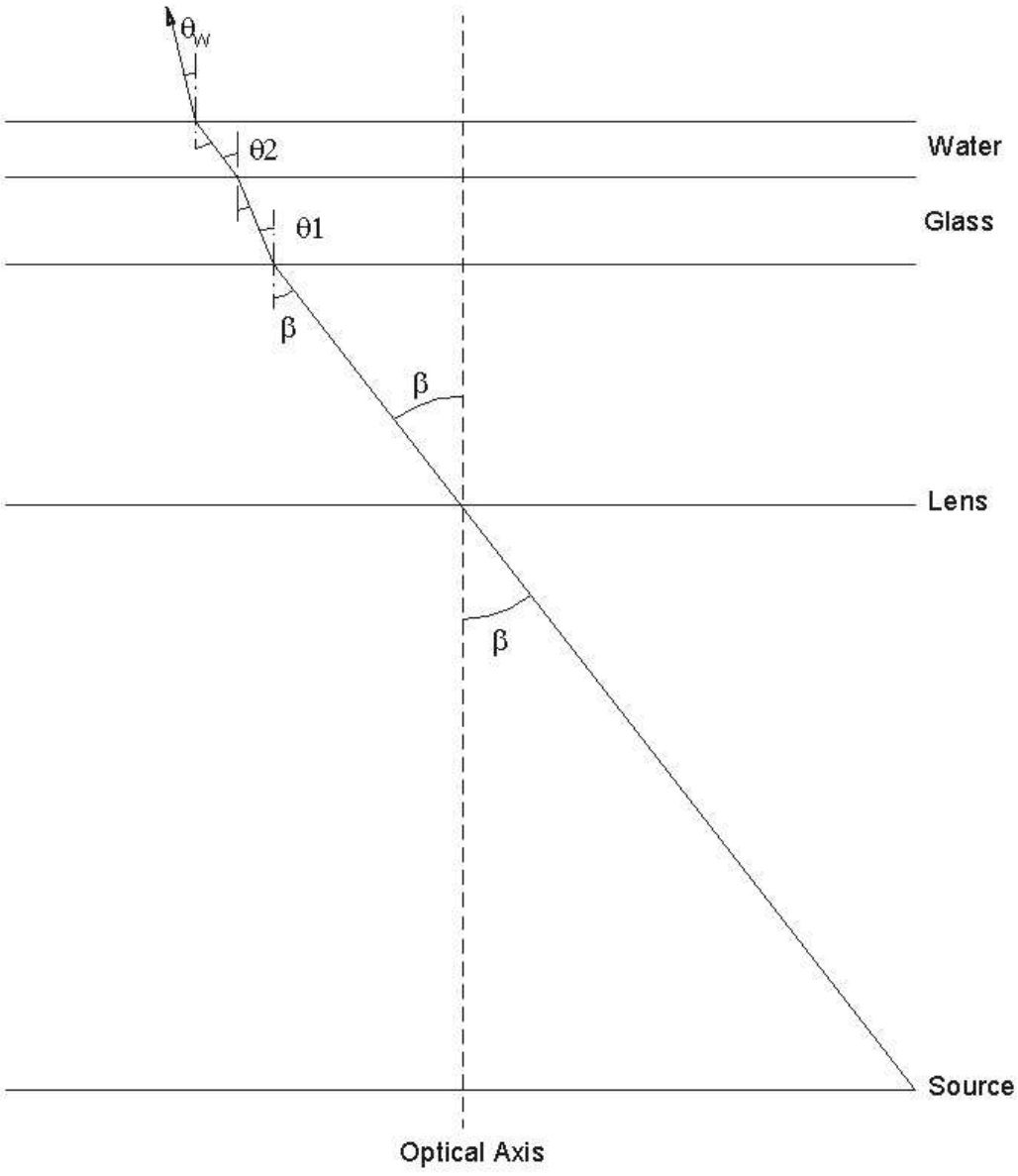

Figure 9.1: The path of a ray when passing through the optical system

and θ_w is the slope of the water and $-\frac{\pi}{2} \leq \theta_w \leq \frac{\pi}{2}$.
Therefore

$$\theta_2 = \arcsin\left(\frac{n_2}{n_3}\sin\acute{\theta_2}\right) \tag{9.7}$$

The limiting factor to these angles is total internal reflection. The critical angle at the lens-air interface is 42.16°, at the glass-water interface is 61.28°, and at the water air interface is 48.61°.The field of view is restricted to the area where all the coloured beams overlap. This is influenced by the size of the lens, the size of the source screen, and the distance of the lens from the water surface.

The entire process has been programmed in MATLAB. The inputs to the program are the distance from the optical axis, and the slope at the water surface. The outputs are the angle of the ray at exit and the location of the point of exit from the optical axis. The code appears in Appendix E.

The maximum angle the apparatus can detect, is dependent on the size of the source screen, as this influences the maximum angle of incidence a ray can have. The maximum radius on the source screen is $r = 450\,mm$. This means that a ray from this point will be at an angle of 21.98° to the vertical when in the layer of water, and the slope of the water surface would have to be

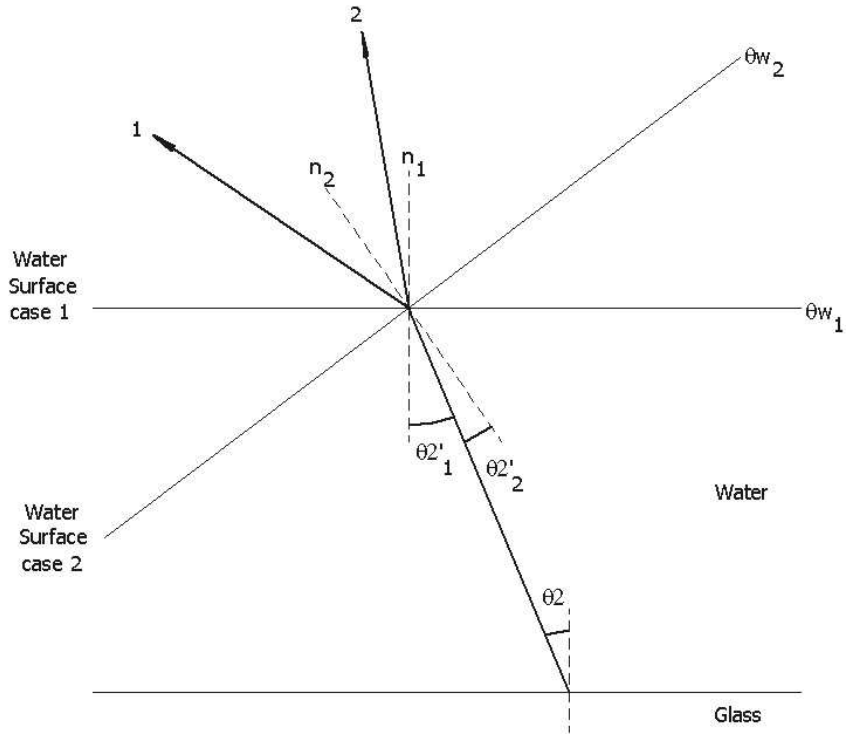

Figure 9.2: The influence of the water slope on the emitted ray

64.89° for this ray to be emmited vertically. This is the maximum angle the apparatus can detect (MATLAB code also in Appendix E).

Due to the lens being of such a large diameter, only supported around its circumference, the lens sagged under its own weight. This had adverse effects on the performance of the lens, as can be expected, because the curvature of the lens has changed, changing the focusing properties of the lens. To correct this problem, a sheet of glass $6mm$ thick was placed under the lens, keeping the lens plane. This does not adversely affect the system. It does introduce another constraint though, and that is a critical angle of 78.6° at the glass-lens interface.

The orientation of the lens was also examined, and compared with technical images from the manufacturer's specification sheet. It was discovered that the lens was not used correctly, in that it was facing the wrong direction. The ideal use of a Fresnel lens is to create a collimated beam of light, which was the intended use of the lens, but how it was set up, the lens was focusing light somewhere between the water table and the first mirror. Images for the two cases shown in figure (9.3) and (9.4) below. This was evidently the cause of the interference seen in the images.

Figure 9.3: Correct orientation

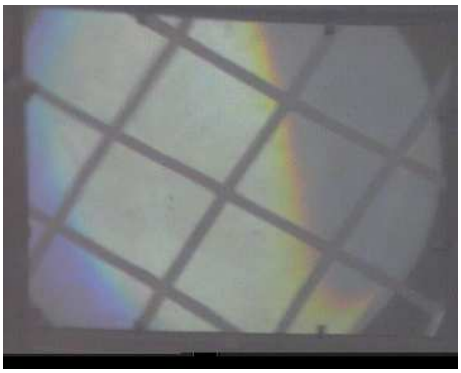

Figure 9.4: Incorrect orientation

9.2 Computational Fluid Dynamics

9.2.1 Fictitious gas with $\gamma = 2$

Grid generation

The grid was generated in GAMBIT, the mesh generation program accompanying FLUENT (all subsequent grids, i.e. for VOF were modelled using the same program). The system is symmetric, so only half the system was modelled. The domain extents are $-1.1m \leq x \leq 0m$ and $0m \leq y \leq 0.8m$. The leading edge of the wedge is $0.5m$ from the origin, and the width of the wedge at the trailing edge is $20\,mm$, half its actual width. The grid has 98 256 cells in one cell zone. Due to the simple shape of domain, the grid is a structured grid, composed entirely of quadrilateral cells, with minimum and maximum face areas of $2.92 \times 10^{-3}\,m^2$ and $3.00 \times 10^{-3}\,m^2$ respectively. The grid is shown in figure (9.5) below, with a close up of the grid around the wedge in figure (9.6). Flow is from right to left and the origin is at the bottom right hand corner of the grid.

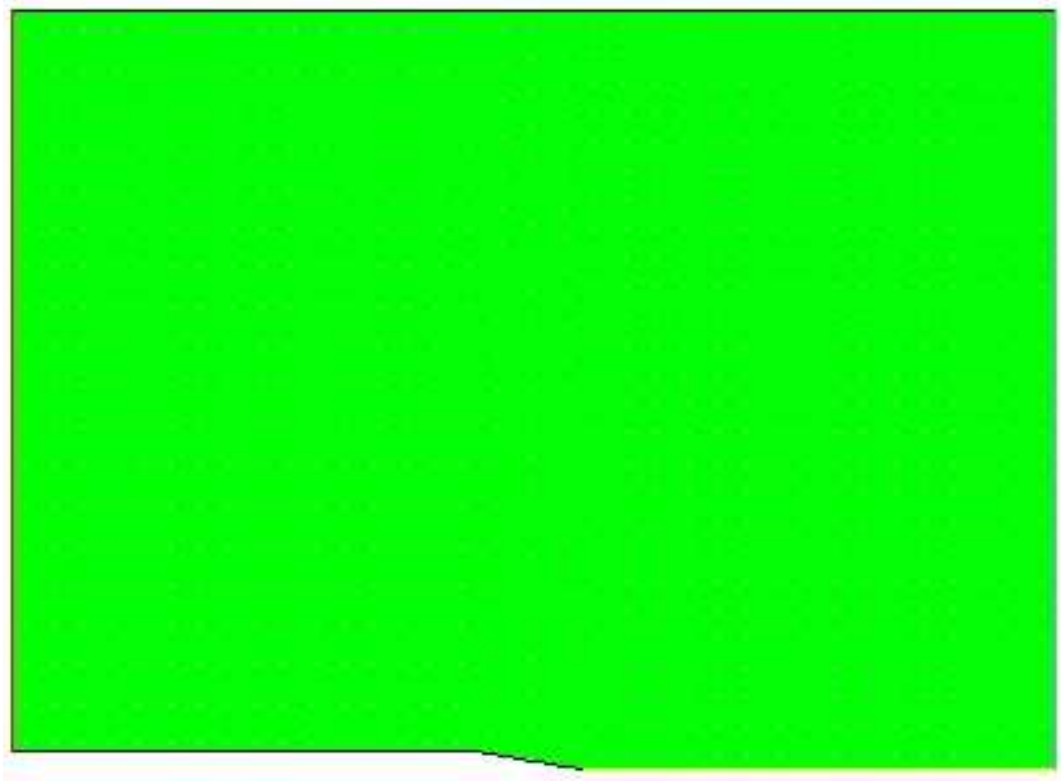

Figure 9.5: Grid for the fictitious gas case

The grid generation process was an iterative procedure, leading to the selection of the final grid shown above. The initial mesh was modelled with the actual wedge shape. When running simulations with this set-up the solution diverges, due to wake at the rear of the wedge. The trailing edge of the wedge was then extended (parallel to the symmetry plane of the wedge) to the boundary. Actual wedge dimensions were used. The initial meshes were also coarser and the domain was smaller than the final mesh.

The boundary types of the grid are as follows:

i The pressure-inlet and pressure-outlet are the right and left edges of the domain, respectively, (the direction of flow is from right to left).

ii A symmetry plane extending from the origin to the leading edge (apex) of the wedge.

iii The wedge, which includes the edge starting from the rear of the wedge and extending to the outlet, is modelled as a wall.

iv The edge opposite to the wedge is also modelled as a wall.

Modelling the flow

The material properties of the fictitious gas have to be entered in FLUENT. In FLUENT, γ is not entered explicitly, but rather the molecular weight and the specific heat at constant pressure is entered. FLUENT then solves for gamma

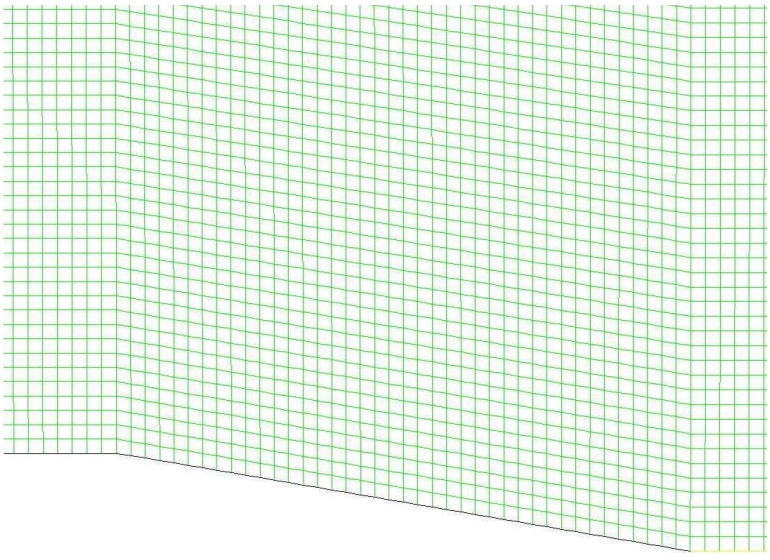

Figure 9.6: Close up of the grid around the wedge

based on these values. These values had to be found for the fictitious gas.

From equation 3.11, it is known that

$$\gamma = \frac{c_p}{c_v}$$

Another equation relating the specific heat at constant pressure and the specific heat at constant volume is

$$c_{p_{mol}} - c_{v_{mol}} = \mathcal{R} \tag{9.8}$$

where $\mathcal{R}$ is the universal gas constant and $\mathcal{R} = 8.31\, J/(mol\, K)$. The subscripts indicate that this equation is valid on a molar basis. Therefore if M is the molecular weight of a gas, with units g/mol, then

$$c_p = \frac{c_{p_{mol}}}{M} \tag{9.9}$$

$$c_v = \frac{c_{v_{mol}}}{M} \tag{9.10}$$

$$R = \frac{\mathcal{R}}{M} \tag{9.11}$$

where R is the specific gas constant, with a different value for different gases. Equation 9.8 can therefore be represented for a specific gas, by dividing throughout by the molecular weight of the gas, as

$$c_p - c_v = R \tag{9.12}$$

The value of R for air is $287\, J/(kgK)$.

For the fictitious gas, we can find $c_{p_{mol}}$ and $c_{v_{mol}}$, since we essentially have two equations, (3.11) and (9.8), and the two unknowns, $c_{p_{mol}}$ and $c_{v_{mol}}$. This is not useful though, if M is unknown. Since M is a measured property of a gas, there is no way of determining M for the fictitious gas. Instead of arbitrarily guessing what M is, the following analytical approach was used.

Since M is unknown, we assume it to be the same as for air, $28.97\, kg/kmol$. We then calculate what c_p is for $\gamma = 2$, and get $c_p = 574\, J/(kg\, K)$. We then do the opposite, and assume c_p is the same as for air, $1006.43\, J/(kg\, K)$. We then calculate what M is for $\gamma = 2$, and get $M = 16.52\, kg/kmol$. For both cases

then, $\gamma = 2$. To observe how FLUENT handles material properties, these two different cases were simulated with the same conditions in FLUENT, and the results were exactly the same. The first case was then used for all simulations for a fictitious gas with $\gamma = 2$. The MATLAB code for the two cases appear in Appendix E.

Pressure and temperature are needed to specify the flow conditions in FLUENT. These quantities are dependent on γ and Mach number.

The pressure is given by

$$p_0 = p_s\big(1 + \frac{\gamma - 1}{2}M^2\big)^{\frac{\gamma}{\gamma - 1}} \tag{9.13}$$

where p_0= total (stagnation) pressure
p_s= static pressure, assumed to be $101325Pa$
M= Mach number

The temperature is given by

$$T_0 = T\big(1 + \frac{\gamma - 1}{2}M^2\big) \tag{9.14}$$

where T_0= total (stagnation) temperature
T = operating temperature, assumed to be $300K$
M= Mach number

These equations were used to find the pressure and temperature at the different Mach numbers for $\gamma = 2$. A small program was written in MATLAB to do so, with the input being the Mach number and the outputs being total pressure and total temperature. The code appears in Appendix E.

The values of pressure and temperature are then used to set the boundary conditions which specify the flow. At the pressure inlet boundary, the total pressure, total temperature and static pressure are entered. At the outlet the inputs are total temperature and static pressure. Since the absolute pressure is the sum of the gauge pressure and operating pressure, the operating pressure is set to zero, so the absolute and gauge pressures are equivalent, since FLUENT always uses gauge pressure. The operating pressure is also less significant at

higher Mach numbers. [35].

Post-Processing

For all the cases investigated, a plane $5mm$ from the rear end of the wedge, parallel to the flow, was used to compare the different depth- and pressure ratios. Since the fictitious gas case is 2-dimensional, instead of using a plane a line at the same location was used. Values of density values were then taken from along this line, and density ratios were calculated.

9.2.2 Shallow water free surface flow (VOF case)

Grid Generation

Only half the system was modelled, due to symmetry. The domain extents are $0\,m \leq x \leq 0.3\,m$, $0\,m \leq y \leq 0.8\,m$ and $0\,m \leq z \leq 0.2\,m$. The leading edge of the wedge is $0.2\,m$ from the origin, and the width of the wedge at the trailing edge is $20\,mm$, half its actual width. The grid has 61 435 cells in one cell zone. Due to the simple shape of the domain, the grid is a structured grid, composed entirely of hexagonal cells, with minimum and maximum cell volumes of $1.14 \times 10^{-7}\,m^3$ and $1.00 \times 10^{-6}\,m^3$ respectively. The grid is shown in figure (9.7) below, with a close up of the grid around the wedge in figure (9.8). Flow is from bottom to top and the origin is at the centre of the bottom plane of the grid.

There is a difference of an order of magnitude in the minimum and maximum cell volumes, because the grid was adapted in FLUENT. During grid adaption, a hexagonal cell is divided into four smaller hexagonal cells. The initial mesh, generated in GAMBIT, had uniform cell sizes. Running a simulation with this mesh did not produce satisfactory results, as can be expected, since the water depth was half that of the cell size, and resulting flow patterns cannot be seen. The co-ordinates of the adapted domain are $0\,m \leq x \leq 0.3\,m$, $0\,m \leq y \leq 0.8\,m$ and $0\,m \leq z \leq 0.01\,m$, i.e. twice the water depth. Resulting flow patterns are clearly seen with the adapted grid.

For the volume of fluid case, the actual wedge profile was modelled, as opposed to the fictitious gas case, where the rear edge of the wedge is extended until the

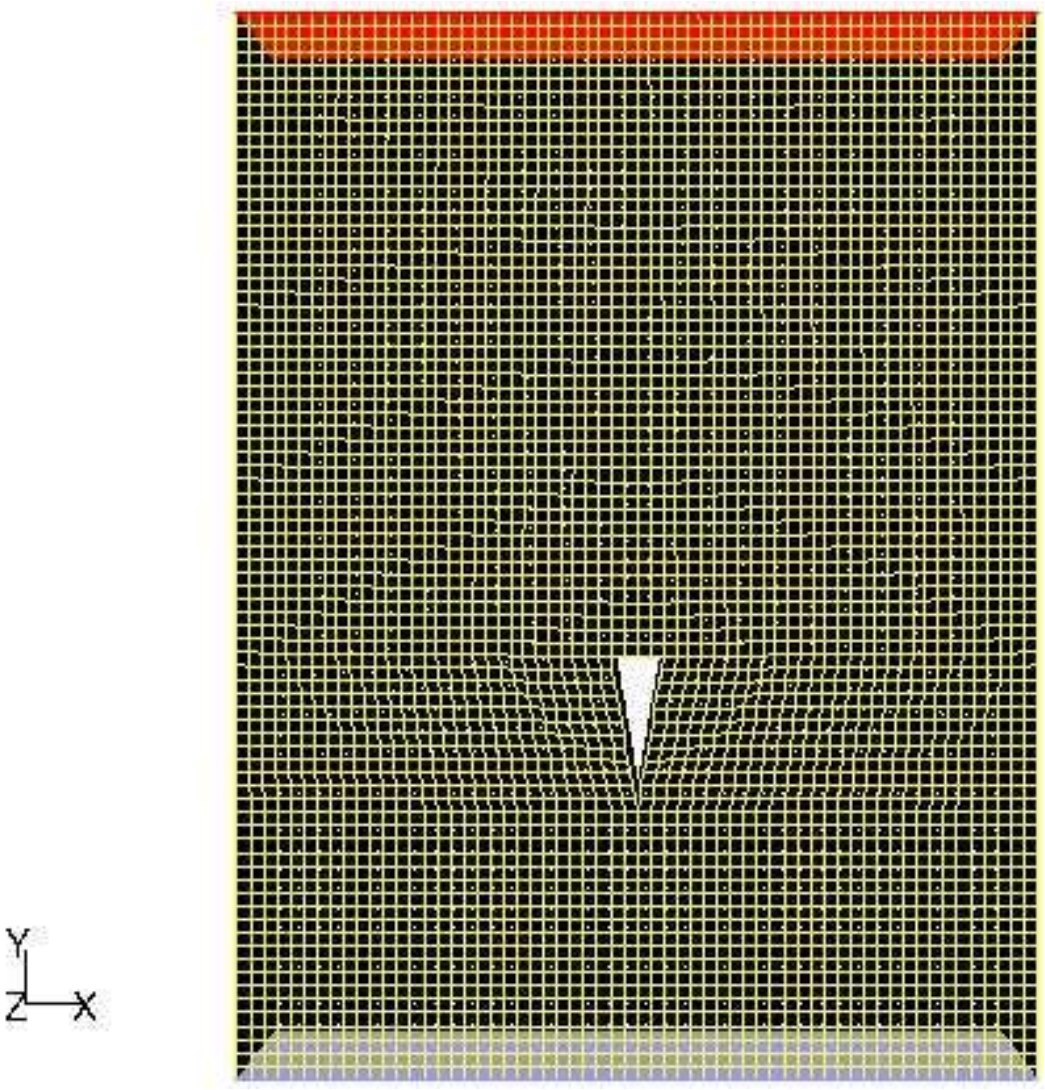

Figure 9.7: The grid for the stationary wedge case

domain boundary parallel to the flow. This did not have any adverse effects, as is the case with the fictitious gas where divergence occurs, and is suitable for VOF cases. All subsequent VOF cases were modelled with the actual wedge shape as well as actual wedge dimensions. The domain was extended at the rear of the wedge, so the outlet boundary conditions did not interfere with the flow patterns.

The boundary types of the static wedge VOF case are similar to the compressible gas case, except that for the VOF case the grid is three dimensional, so edges in the two-dimensional gas case are equivalent to faces in the three-dimensional VOF case. The boundary types of the grid (see figure (9.7)) are as follows:

- the pressure inlet boundary type has been specified for the face at the lower end of the domain, transverse to the flow direction.
- the symmetry boundary type has been specified for the face at the centre of the domain, extending from the origin to the apex of the wedge, parallel to the flow.

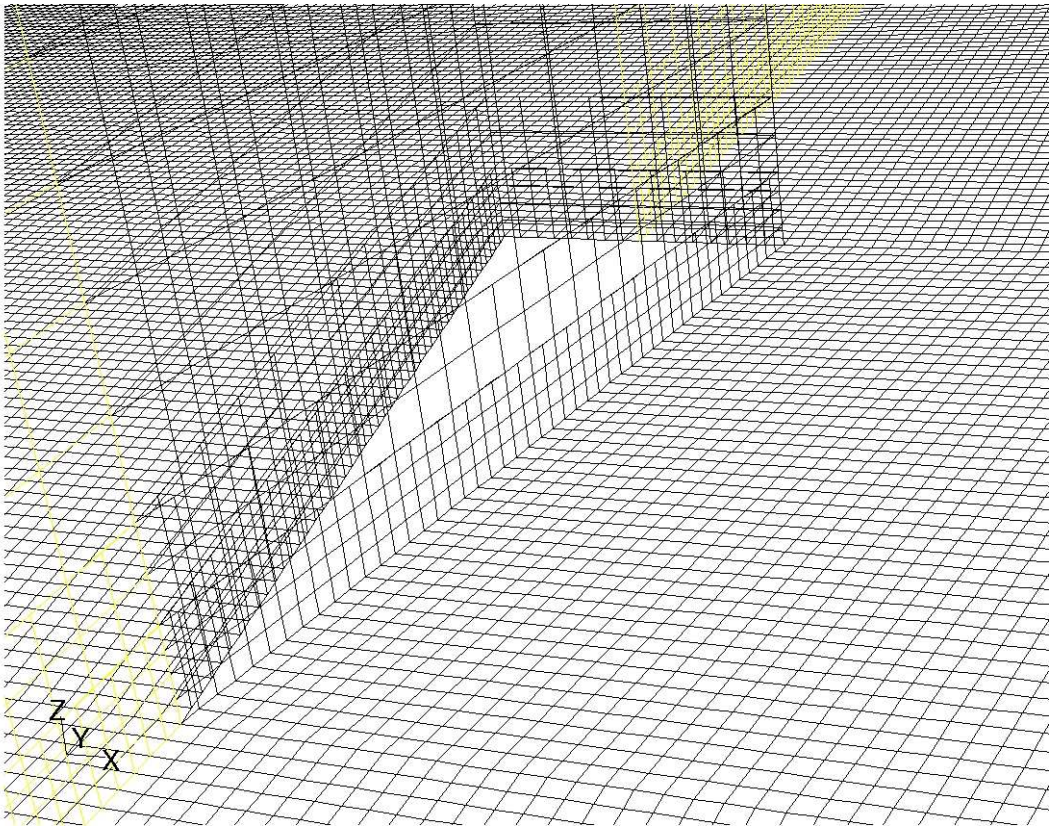

Figure 9.8: Close up of the grid around the wedge

- the wall boundary type has been selected for the wedge.
- the symmetry boundary type has been specified for the face at the centre of the domain, extending from the rear end of the wedge to the end of the domain, parallel to the flow.
- the pressure outlet boundary type has been specified for the face at the upper end of the domain, transverse to the flow direction.
- the wall boundary type has been selected for the face at the left and right end of the domain, parallel and opposite to the symmetry plane.

Modelling the flow

The mesh extends to $0.2\,m$ in the z domain, yet the average water depth is $0.005\,m$, since the influence of this boundary to the flow is small. A point at this boundary, is where the reference pressure is set, in this case to atmospheric pressure, i.e. $101325\,Pa$.(The co-ordinates of this point are $x = 0\,m$,$y = 0\,m$, $z = 0.2\,m$, and is entered in the *Operating Conditions* panel.) This is the suggested procedure in FLUENT to include effects of the atmosphere or any reference pressure of the gaseous phase. The boundary at the top of the domain, i.e. open to the atmosphere is therefore modelled as a symmetry plane, with a slip condition, as opposed to a pressure inlet, which was the initial assumption. When running a simulation with the boundary condition set to be a pressure inlet, the solution does not converge.

Gravitational effects are included by selecting gravity and specifying the gravitational acceleration, in the *Operating Conditions* panel.

Air and water are the two materials present in the model, and are selected in the materials panel. Water is selected from the Fluent database of materials, as $water - liquid$. The convention in FLUENT when using the VOF method is that the lightest phase, normally the gas, is specified as the primary phase, and the heavier phase is specified as the secondary phase. In our case, *air* is the primary phase and $water - liquid$ is the secondary phase.

Also in the *Phases* panel, the surface tension and wall adhesion are specified. The surface tension for water is $73\,dyn/cm = 0.073\,N/m$ at $20\,^{\circ}\mathrm{C}$ [36], and this is the value used. The wall adhesion option is only checked at the

$Phases \rightarrow Interaction$ panel, but specified in the $BoundaryConditions$ panel. This is justified, recalling from section (5.3.2), that wall adhesion involves a solid phase in addition to the two fluid phases, and the effect of the solid phase is specified as wall type boundary condition in the boundary conditions panel.

Therefore in the boundary conditions panel, the surfaces where wall adhesion occur, are the glass surface and the aluminium wedge. The wall adhesion is entered in the $Momentum$ tab when setting the boundary conditions for the two surfaces. From section (5.3.2), the contact angle $\theta_{contact}$ is measured from the wall, to the tangent at the interface of the two phases (i.e. the water-air interface). The contact angle for the glass was chosen to be 30° and 45° for the aluminium wedge. These values are based purely on observation, as special apparatus is required to accurately measure the contact angle.

The other boundary conditions applied to the boundary types are as follows:

For the pressure inlet, open channel flow is selected and the free surface level is entered. This value is different for the different Froude numbers tested, and is the actual water depth for the respective experimental tests at the different Froude numbers. These water depths are close to $5\,mm$, the optimal depth. There are different ways of specifying the free surface level in FLUENT, but the chosen method measures the free surface level from the datum, so the actual water depth is entered, and the height at the datum is set to zero. The origin of the grid also coincides with the bottom level. The velocity of the flow is also entered in this panel, and again is dependent on the actual experimental velocity for the different test cases. The flow direction at the inlet is specified using the $Direction\,Specified\,Method \rightarrow Direction\,Vector$. Flow is in the positive-y direction, so the inputs are $x = 0$, $y = 1$ and $z = 0$.

At the pressure outlet panel, open channel flow is also selected. The free surface level is entered in the same way as with the pressure inlet boundary condition. The flow is in the same direction as for the pressure inlet, so the same direction vector values are entered.

For the actual flow on the water table, water flows off the side of the table, and simulations were done specifying the boundary condition at the sides of the table as a wall boundary condition. Therefore, to model the actual flow,

the wall boundary condition was changed to a pressure outlet, with the same inputs as the pressure outlet boundary condition at the original outlet (opposite to the inlet).

In FLUENT, for the VOF case, if a steady state solution is required, which applies to the stationary wedge case, the region where the liquid is, needs to be patched. In essence the domain is filled to the required depth with the liquid, before the simulation is started, and before the flow enters at the pressure inlet. To do this in FLUENT the region is first specified in the *Adapt* $\rightarrow$ *Region* panel. The domain extents of this region are $0\,m \leq x \leq 0.3\,m$, $0\,m \leq y \leq 0.8\,m$ and $0\,m \leq z \leq d\,m$, where d is the water depth applicable to the test case. This region is then patched with water in the *Solve* $\rightarrow$ *Initialize* $\rightarrow$ *Patch* panel, by setting the volume fraction of water to one for this region, i.e. totally filled with water. The flow velocity and direction is also patched after the liquid region has been patched, by setting the y-velocity to the same value as specified in the *Pressure Inlet* boundary condition panel.

Post-Processing

As mentioned for the gaseous phase, a plane $5\,mm$ (i.e. close to the wedge where wall adhesion effects are no longer significant) was used to compare the different cases, i.e. a standard comparison for all cases. Therefore a plane was created $5\,mm$ from the trailing edge of the wedge, parallel to the flow, in FLUENT by using a quadric surface. Knowing that the trailing edge of the wedge is $20\,mm$ (half the actual width of wedge at the trailing edge) from the symmetry plane, and the symmetry plane coincides with the y-axis, the plane to be created would be $25\,mm$ from the y-axis, parallel to the $z-y$ plane. The input to the quadric surface is therefore $1, 0$ and 0 for x, y and z respectively, and the distance is $0.025\,m$. Once the plane has been created, the contours of volume fraction for water are viewed for the plane, and the number of levels (the number of divisions the range of the variable will be divided into) are set to 2, i.e. only two colours, one for water, and one for air, are displayed, and at the interface of the two layers is the water surface. Height measurements were taken, and divided by the undisturbed water depth to give the depth ratio.

The entire step by step procedure for setting up the stationary wedge VOF case in FLUENT, is given in Appendix F.

9.2.3 Dynamic wedge

Grid generation

The grid for the dynamic case is larger than the mesh for the static case. The grid for the dynamic case had to account for the entire motion of the wedge, i.e. the motion of the wedge from start to finish had to be enclosed within the mesh domain. If this not done, and the wedge is still moving when it reaches the end of the domain, there is strong likelihood that the simulation will crash.

The domain extents are $-0.317\,m \leq x \leq 1\,m$, $0\,m \leq y \leq 0.3\,m$ and $0\,m \leq z \leq 0.2\,m$. The leading edge of the wedge is at the origin, which is $1\,m$ from the end of the domain, allowing for the wedge motion. The width of the wedge at the trailing edge is $20\,mm$, half its actual width. The grid has 130 210 cells in one cell zone. Due to the simple shape of domain, the grid is a structured grid, composed entirely of hexagonal cells, with minimum and maximum cell volumes of $4.12 \times 10^{-8}\,m^3$ and $1.03 \times 10^{-6}\,m^3$ respectively. The grid is shown in figure (9.9) below. The wedge moves from left to right and the origin is $0.317\,mm$ from the bottom left hand corner of the grid (at the apex of the wedge).

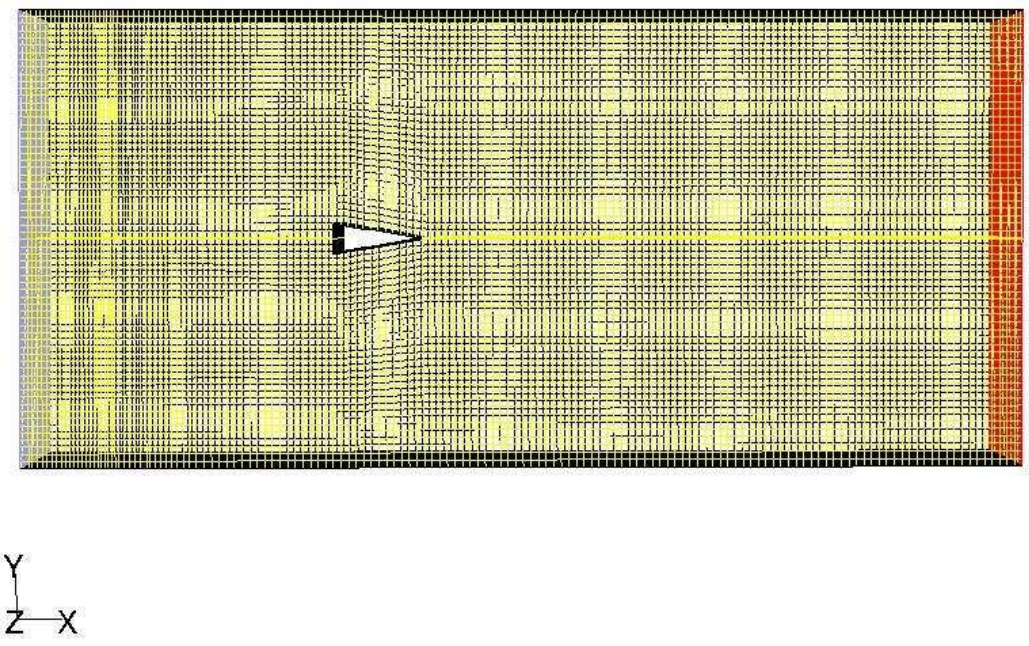

Figure 9.9: The grid for the dynamic wedge case

The initial grid was also modelled with uniform cell sizes like the stationary wedge case. Grid adaption is not available for dynamic layering, however, so the uniform cell sizes have the same effect as the static case, where cells are not small enough to detect flow patterns, because resulting waves are smaller than cell sizes. The mesh had to manually be adapted in GAMBIT to a similar adapted domain as the stationary wedge case, i.e. to a height in the z-domain of $10\,mm$, so as to detect the resulting flow patterns.

The imposed boundary types for the planes enclosing the domain, for the dynamic wedge case, are the same as for the stationary wedge case. The only difference is that the model has been rotated by $\frac{\pi}{2}$, so the wedge moves in the positive x-direction.

Modelling the flow

Since the boundary types are the same as the static wedge case, essentially the same boundary conditions are applied to these boundary types as with the static case. The only difference being that the water is stationary for the dynamic wedge case, so the velocity at the inlet is zero. Also, if reversed flow in cells is to be avoided, the pressure inlet and outlet can be swapped. This is because the motion of the wedge is opposite to the flow direction, compared to the static case, and as a result of the motion, the flow now exits at the inlet and enters at the exit.

The velocity of the wedge is entered into FLUENT using a velocity profile. This is simplest way of defining the velocity, and is only available if the motion is one-dimensional. If we imagine a velocity-time graph, the velocity profile is a collection of points describing the graph, and hence the motion. It consists of two arrays, of equal length, one for time and one for the velocity at the corresponding times.

Experimentally, the wedge is accelerated by dropping a weight connected to the wedge, with a string, through a pulley and rail system. The mass of this weight is $75\,g$ and it is subjected to gravitational acceleration. From Newton's second law the force from the falling weight is

$$F = ma \rightarrow F = (0.075\,kg)(9.81\,m/s^2) \rightarrow F = 0.74\,N \tag{9.15}$$

The weight of the wedge including attachments is $1.17\,kg$. When subjected to the force of the falling weight, the resulting acceleration is

$$F = ma, \therefore a = \frac{F}{m} \rightarrow a = \frac{(0.74\,N)}{(1.17\,kg)} \rightarrow a = 7.63\,m/s^2 \tag{9.16}$$

Since the wedge accelerates and then decelerates, it is assumed that the wedge accelerates with this acceleration for half the distance and then decelerates with same value of acceleration (i.e. negative acceleration) for the other half. The distance travelled by the wedge is $0.7\,m$, which is less than the domain extent. Therefore, when the wedge stops, the motion of the resulting waves moving through the remaining part of the domain, can be seen. The velocity profile is shown in Appendix (E.2.2).

Since we are dealing with a dynamic mesh, *Dynamic Mesh* is selected from the *Dynamic Mesh Parameters* in FLUENT. *Dynamic Layering* is then selected as this is the ideal dynamic mesh update method for the dynamic case in consideration. In the *Layering* panel, the split (α_s) and collapse (α_c) factors are entered, and also the ideal cell height (h_{ideal}). The ideal cell was chosen to be $7.25\,mm$ and the split and collapse factors were chosen to be 0.7 and 0.5 respectively. Recalling from section (5.4.1) on dynamic layering, and using equations (6.9) and (6.10), a cell layer will be split when the cell height is greater than $12.33\,mm$ and a cell layer will be merged when the cell height is less than $3.625\,mm$. The average cell height in the direction of motion, where dynamic layering occurs, is $10\,mm$.

In the *Solutions* tab more dynamic meshing parameters are entered. The maximum time step size is calculated by dividing the smallest cell size (cell length in the direction of motion, i.e. along the x-axis), by the maximum velocity,

$$\triangle t_{max} = \frac{\triangle s_{min}}{v_{max}} \tag{9.17}$$

The maximum velocity, v_{max}, is obtained from the velocity profile and is $0.66\,m/s$. The smallest cell size, $\triangle s_{min}$, is $0.01\,mm$. $\triangle t_{max}$, is therefore $0.015\,s$.

The total number of time steps is simply the total time divided by the maxi-

mum time step, $\triangle t_{max}$,

$$Total\,time\,steps = \frac{total\,time}{\triangle t_{max}} \tag{9.18}$$

The total time is obtained from the velocity profile, and is $2.12\,s$. The maximum time step size, $\triangle t_{max}$ from equation (9.17), is $0.015\,s$. The total number of time steps is therefore 140 time steps. This is only for the wedge motion though, and if the motion of the wave after the wedge stops is to be observed, the number of time steps is increased to 175 time steps.

Since the case is dynamic, it may be desirable to see how the flow varies with time, by animating the motion. The procedure is as follows, a new graphics window is opened, and a new animation sequence is defined in the $Solve \rightarrow Animate \rightarrow Define$ panel. Since the water surface is of concern, an iso-surface of volume fraction close to zero (0.05) is created. Any variable can be monitored, and the display seen in the graphics window is exactly what FLUENT will record. The change in this variable is then monitored by FLUENT by specifying the time step or number of iterations when an image of the domain should be saved. When the simulation is complete, the images can be saved in a different file format by specifying this in the *Hardcopy Options* panel, since the default image file format in FLUENT can only be used in FLUENT. These images can be combined to make a video clip of the animation.

The entire step by step procedure for setting up the dynamic wedge VOF case in FLUENT, is given in Appendix F.

9.3 Image Processing

Images were analyzed using commercially available MATLAB® software, more specifically the Image Processing Toolbox. A half cylinder made from perspex was used to calibrate the colour-slope relationship. All slopes are represented by the half cylinder and it is only necessary to encode a particular colour with a specific range of slopes. MATLAB recognizes a colour image as a RGB (Red Green Blue) image, where each pixel is specified by a combination of three values namely, the intensity of red, green and blue. In MATLAB, a RGB image

is represented as a $m \times n \times 3$ array, where the dimension of the array is the dimension of the image (in pixels), and there is one array for each colour i.e. red, green and blue.

Since a half cylinder has constant slopes along the length of the half cylinder, each circular colour band from the colour mask is represented as two bands of colour along the length of the half cylinder; one band on either side of the centre of the cylinder. Average values of intensity were taken for the two bands of colour, and a range of intensities coupled with a range of slopes for each colour was obtained. The values were corrected for water, using the refractive indices of the two materials. The MATLAB code for doing this procedure appear in Appendix E.

When using the calibrated values from the perspex cylinder with an image of the wedge in water, the correct slopes were not detected. The intensities from the image with water were different to the calibrated intensities from the perspex cylinder. Although, a particular colour encodes a particular range of slopes, a colour seen with the naked eye is that colour, but the range of intensities from calibration do not cover the entire range of that colour, but rather the intensities specifically in the optical medium of perspex. Considering that a RGB image is represented as a $m \times n$ array for each colour, it is accurate in distinguishing the different shades of each colour, better than what the naked eye would detect. Calibrating the optical system using water, would solve this problem.

The images were thus analyzed on the basis that a particular colour from calibration encodes a particular range of slopes, corrected for water. This assumption is valid provided there is no frequency shift of the light waves when passing through the cylinder, as would occur when white light passes through a prism to create a spectrum of coloured beams. If this were the case though, similar behavior can be expected with water, therefore calibrating using water would circumvent this problem.

The images were analyzed along the same profile ($5\,mm$ from the rear edge of the wedge) as with the CFD. Each interval of colour was measured along the profile, and the slopes from calibration, corrected for water, were used to find the heights at each interval. It is a continuous process where the next

height is determined from the previous height, coupled with the distance of the interval, and the slope. If a colour band, e.g. red, is surrounded on both sides by another colour, e.g. blue, indicating a smaller slope, then it is assumed that a peak occurs, within that colour band , i.e within the red colour band. The technique is not very accurate though, as it depends on human judgment, and the quality of the image, i.e. the image contrast, to accurately see where the colour changes from one band to the next, which indicates a change in slope. Another shortcoming of this method is that the plane of analysis is two-dimensional, and the actual slope is three-dimensional, therefore slopes transverse to the plane of analysis are not taken into consideration.

9.4 Analytical Determination of Flow Variables

Flow variables were determined for the fictitious gas case, where $\gamma = 2$, analytically using oblique shock wave relations (see Appendix G).

The shock angle is determined from the $\theta - \beta - M$ relation equation (G.27). The wedge angle, θ, the ratio of specific heats, γ, and the upstream Mach number, M_1, are known, with the only unknown being the shock angle, β.

$$\tan\theta = 2\cot\beta\left[\frac{{M_1}^2\sin^2(\beta) - 1}{{M_1}^2(\gamma + \cos(2\beta)) + 2}\right]$$

Once the shock wave angle is known, the density ratio is determined from equation (G.28).

$$\frac{\rho_2}{\rho_1} = \frac{(\gamma+1){M_1}^2\sin^2\theta}{(\gamma-1){M_1}^2\sin^2\theta + 2}$$

The same approach is used for the expansion wave, except that the downstream flow conditions from the shock wave now become the upstream conditions for the expansion wave. The expansion wave was also only taken so far as to return the flow to the freestream direction, since the actual turning angle at the rear is not known.

Chapter 10

Results

The test cases considered are:

1. Experimental (actual testing with the water table.)
2. CFD
   (i) Compressible gas with $\gamma = 2$
   (ii) VOF method with one of the following conditions:
      (a) a wall boundary condition for the face opposite the wedge (parallel to the flow; referred to as the "wall" case)
      (b) a pressure outlet boundary condition for the face opposite the wedge (parallel to the flow; referred to as the "no wall" case.)
      (c) one case for no surface tension, no wall.
3. Theoretical (analytical determination of flow variables using shock wave theory.)

The test conditions considered are Froude- or Mach number equal to:

(i) 2.38

(ii) 3.12

(iii) 4.31

Tests at Froude or Mach number equal to one were considered, but due to the difficulty of obtaining this Froude number on the water table, it was abandoned. It was difficult to obtain the required velocity, within a reasonable depth range, since the Froude number is dependent on both velocity and depth. The two extremes are that for a certain velocity, there is a required depth, but

the actual depth is much higher than this (because of the table inclination being too large), or much lower (due to the reduced flow rate by partially closing the inlet valve). The combination of depth and velocity to give a Mach number of one, could not be achieved.

10.1 Stationary Wedge

The Mach angles and respective wave angles were measured for the different cases. The results are as follows (the respective images are in Appendix H):

Table 10.1: Mach/Wave angles for the different test cases.

Froude/Mach number	**2.38**	**3.12**	**4.31**
Experimental	35°	29°	23°
VOF wall	40°	32°	25°
VOF no wall	41°	30°	23°
VOF, no surface tension	40°	-	-
Gas, $\gamma = 2$, CFD	36°	29°	23°
Gas, $\gamma = 2$, Theoretical	36°	29°	24°

The depth profiles along the plane(for 3D)/line(for 2D) of analysis (i.e. 25mm from the symmetry plane) for the different cases are shown in the figures below. The same images in Appendix H are applicable here. The plane is $5\,mm$ from the rear edge of the wedge (transverse to the flow), and the plane is parallel to the flow, extending $50\,mm$ from the leading and trailing edges of the wedge (parallel to the flow). Recall that this location of the plane was chosen, so that the effects of wall adhesion are not significant to the water depth, for the VOF and experimental cases. The plane in relation to the wedge is shown in figure (10.1). The distance along the plane of analysis where a specific bow wave at a given angle would intersect the plane of analysis, is shown as an additional scale on the distance axis.

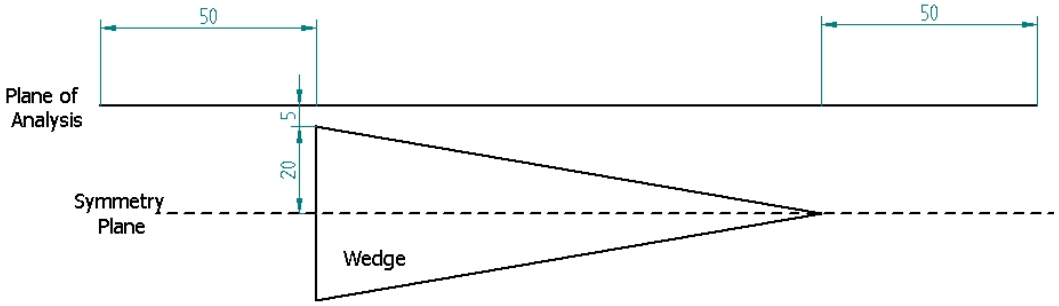

Figure 10.1: The plane of analysis.

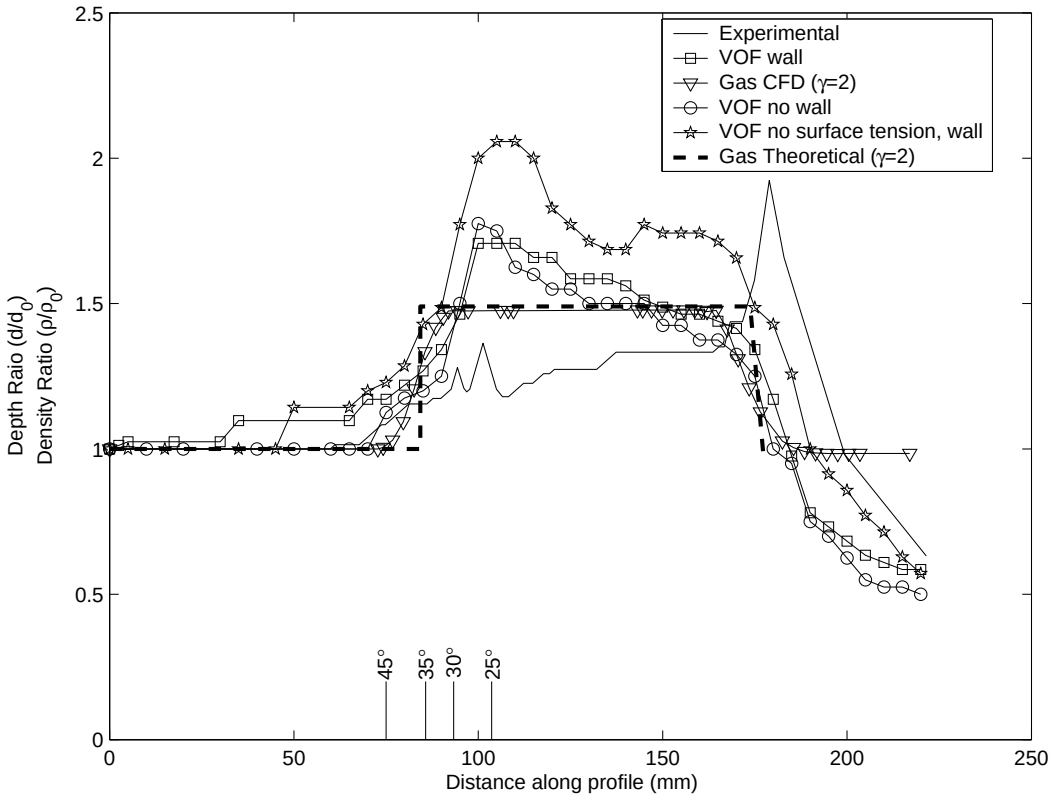

Figure 10.2: Fr or M = 2.38

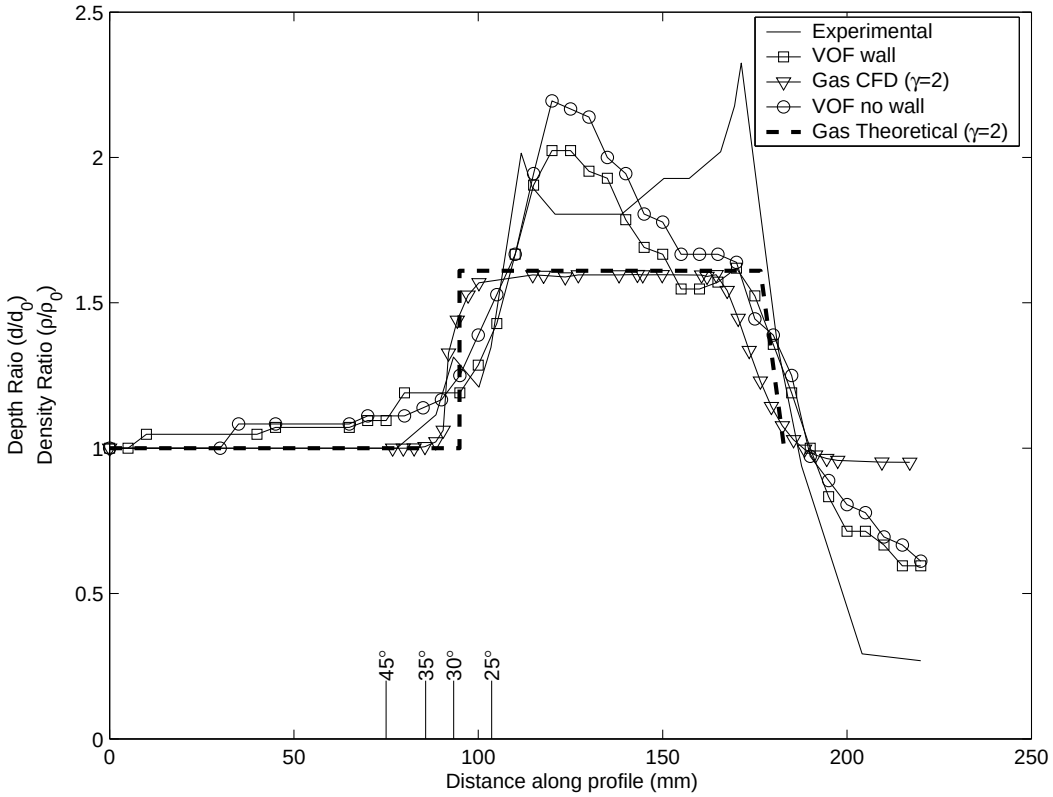

Figure 10.3: Fr or M = 3.12

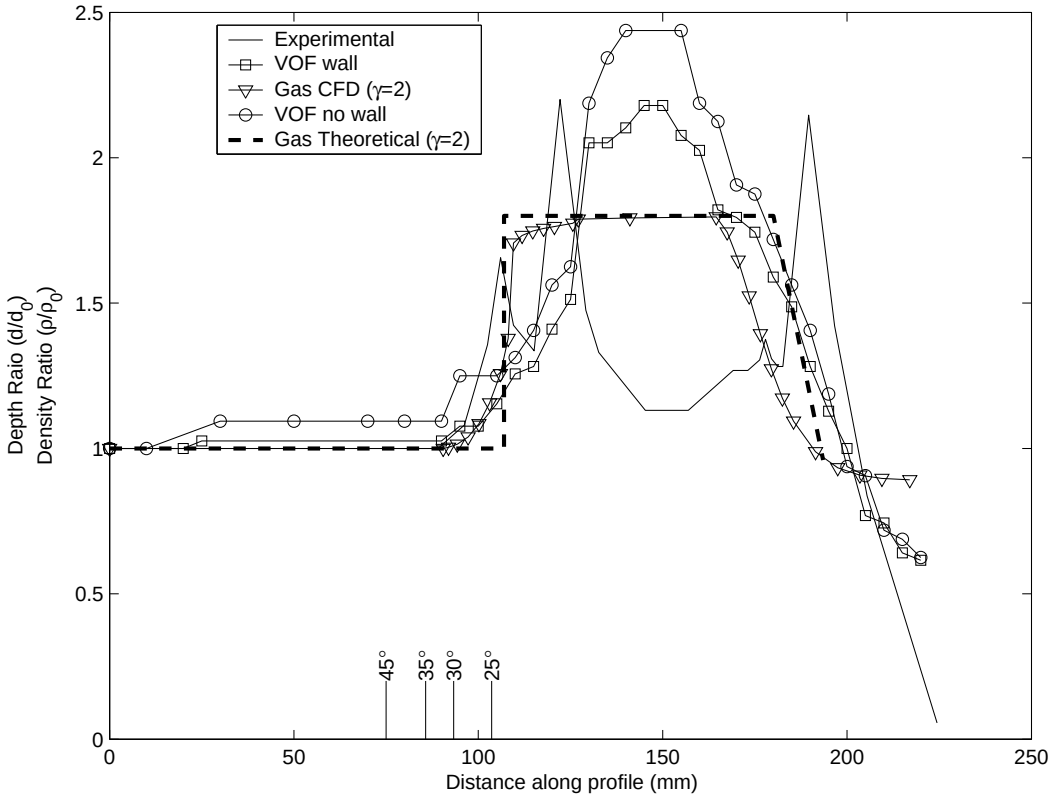

Figure 10.4: Fr or M = 4.31

10.2 Dynamic Wedge

The sequence of images from the experimental case are shown in the figures below. The sequence is limited to the field of view, therefore it starts with the wedge at maximum acceleration then decelerating until the wedge stops and the waves move out of the domain.

Figure 10.5: Experimental t=1.4 s

Figure 10.6: Experimental t=1.6 s

Figure 10.7: Experimental t=1.9 s

Figure 10.8: Experimental t=2.0 s

Figure 10.9: Experimental t=2.1 s

Figure 10.10: Experimental t=2.2 s

Figure 10.11: Experimental t=2.3 s

Figure 10.12: Experimental t=2.5 s

The sequence of CFD VOF dynamic images is show below. There are more images than the experimental case, since the entire wedge motion was modelled. The other three images at the end of the sequence, is when the wedge moves again for a short distance after being stopped.

The volume fraction of water for this sequence is equal to 0.05, i.e. close to the water surface, since at the air water interface the volume fraction of water approaches zero. Any value smaller than this does not yield good results. The videos of other animation sequences, with different volume fractions, and viewed from different angles are shown in Appendix **Y** (Compact Disk (CD) accompanying report). These animations are in Moving Picture Experts Group (MPEG) format.

Figure 10.13: VOF t=0.03 s

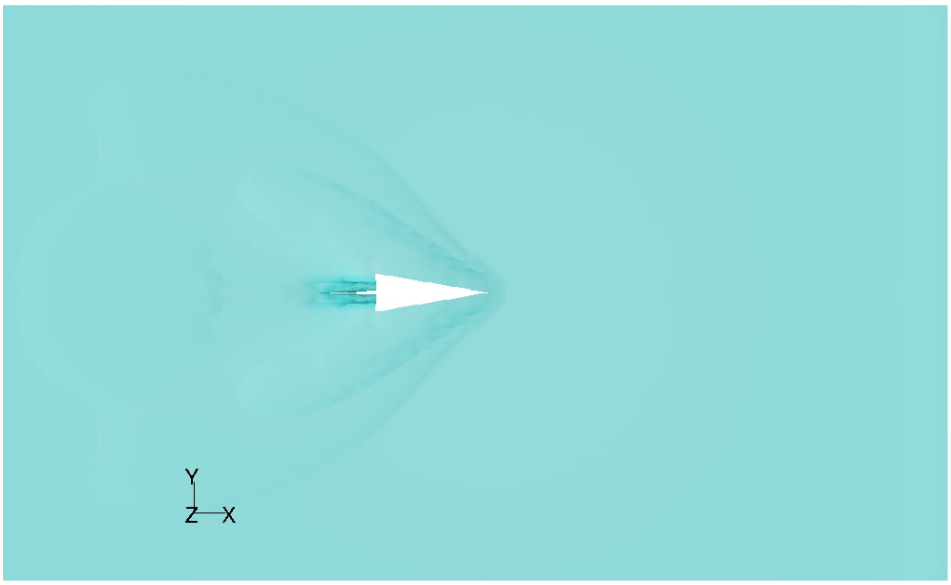

Figure 10.14: VOF t=0.99 s

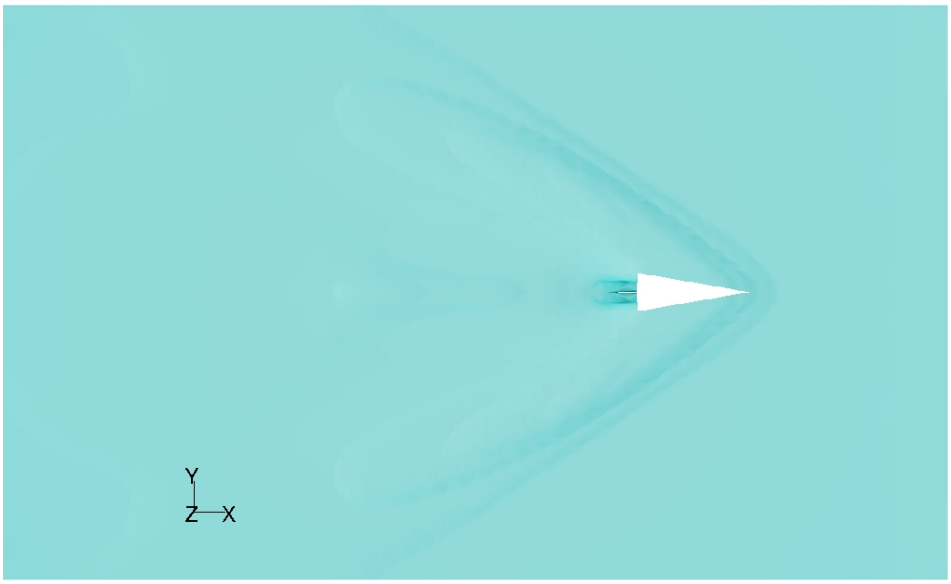

Figure 10.15: VOF t=1.5 s

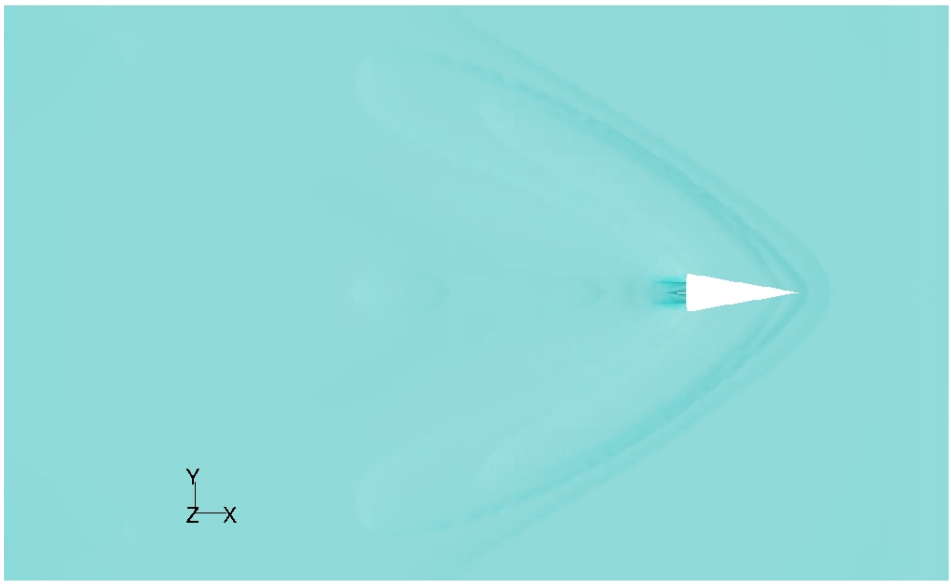

Figure 10.16: VOF t=1.65 s

Figure 10.17: VOF t=1.92 s

Figure 10.18: VOF t=2.01 s

Figure 10.19: VOF t=2.1 s

Figure 10.20: VOF t=2.28 s

Figure 10.21: VOF t=2.52 s

Figure 10.22: VOF t=2.64 s

Chapter 11

Discussion

11.1 Stationary Wedge

11.1.1 Flow Patterns

(Images appear in Appendix H.)
With regard to the Mach and hydraulic jump angles, although quantitative, they give an indication of the qualitative aspects of the flow, namely the flow patterns. At a Froude number of 2.38, the VOF method for all the test cases over-estimate the Mach/jump angle with a minimum difference of 5° for the wall case, and a maximum difference of 6° for the no wall case. The no surface tension test has a difference of 5°. The over-estimation of the Mach/jump angle would be much worse if the wave angles were measured further from the wedge, due to wave curvature. As the Froude numbers increase, the hydraulic jump angle estimation improves. When the Froude number increases to 3.12, the difference is 3° for the wall case and only 1° for the no wall case. At a Froude number of 4.31, there is an exact match for the no wall case and a difference of 2° for the wall case, which is within measurement uncertainty.

The fictitious gas CFD case with $\gamma = 2$, however, shows good agreement with a difference of only 1° at a Mach number of 2.38. There is an exact match for both Mach numbers 3.12 and 4.31.

The analytical determination of the shock angle shows good agreement with the experimental case. At Mach numbers of 2.38 and 4.31, the difference is only 1°. At a Mach number of 3.12 there is an exact match for the shock angles.

Therefore for the wave/jump angles, the fictitious gas case shows the best agreement to the experimental case across all Mach/Froude numbers. At higher Froude numbers the VOF cases show an improvement in the wave angle estimation to the experimental case. For the jump angles, there is no substantial difference between the models where a wall was modelled instead of an outlet, nor where surface tension was neglected.

The VOF wall case for $Fr = 2.38$ (figure H.2), shows reflection of the bow jump off the wall. The water depth increases at the point of reflection to a depth greater than that of the jump. There is a large convex wave which forms a short distance ahead of the outlet, nearly spanning the width of the domain. This wave is also present in the no surface tension, no wall case (figure H.5), although not as pronounced as in the wall case (figure H.2). There also appears to be a reflected wave, although smaller than the reflected wave of the wall case. This large wave at the rear of the domain is not present in the no wall case (figure H.3), although a smaller reflected wave similar to the reflected wave of the wall case is formed. Since the flow is supercritical, this large wave should not affect the flow upstream.

A cause for all these waves could be that the total outflow rate of the system is less than the total inflow rate. For the no wall cases, the reflected wave is smaller than the wall case, and if the outflow at the planes where an outflow instead of a wall is modelled, added to the outflow at the end of the domain, is less than the inflow, then these planes with no wall condition have a similar effect as a wall condition, since water cannot flow out of the domain quickly enough. The outflow parameter entered in FLUENT is a depth, and for all cases was chosen to be the inlet depth, assuming that normal flow conditions will occur after the jump. For the outlet depth to be the same as the inlet depth, especially where the actual depth is greater than this, like the depth at the jump, leads to restricted flow. It seems then that in FLUENT, at locations where the depth is greater than the specified outlet depth, the flow is forced to exit the outlet plane through a slit with a thickness of the specified outlet depth. This then causes the reflected waves, and the large wave before the domain exit, to form. For the experimental case, these effects are not present as the water flows freely at the outlet and the outflow is not restricted.

The no surface tension case also has this large convex wave, although not as

large as in the wall case, even though a no wall condition has been modelled for the planes at the sides of the domain, parallel to the flow. Since there is no surface tension, the intermolecular forces attracting molecules at the surface is much lower than in the surface tension case, and the resulting depth at the jump is higher than in the surface tension case, also modelled with a no wall condition. The specified outlet depth for the surface tension case is therefore not much lower than the depth at the interaction of the jump with the wall. The depth at the interaction of the jump with the wall for the no surface tension case is higher than the specified outlet depth causing the flow to be restricted and reflection to occur as if the wall has been modelled. If no surface tension is modelled coupled with a wall condition, the jumps and wave interactions are expected to be of greater depth than the surface tension case.

For the VOF wall case for $Fr = 3.12$ (figure H.7) there is a smaller reflected wave formed in each corner of the domain, where the bow jump interacts with the wall. This reflected wave is not present in the no wall case (figure H.8) at the same Froude number. The jump angles are smaller at this Froude number than the previous Froude number, so the jump is much longer, in the same domain, than the previous Froude number. The water depth has therefore decreased along the length of the jump, to a depth which is not much greater than the specified outlet depth, not causing any reflection due to flow restriction, for the no wall case. At a $Fr = 4.31$, the jump angle has decreased to an extent that the jump exits at the end of the domain, therefore the wall condition does not make such a significant contribution to the flow, hence the flow patterns are almost exactly the same (figures H.11 and H.12). The only difference being a small wave ahead of the jump, starting about midway across the jump length and extending to the end of the domain, caused by flow restriction from the wall.

The effect of surface tension is evident by comparing images with and without surface tension at a $Fr = 2.38$ (figures H.5 and H.3). For the no surface tension case, the flow pattern is smoother than the other two cases with surface tension. For the surface tension cases, the wavelets formed due to flow interaction can be seen behind the wedge toward the end of the domain. The no surface tension case also does not have any wall adhesion, and this explains the dry patch behind the wedge for this case, which is not present for the other two cases at this Froude number. At higher Froude numbers all cases have the dry

patch behind the wedge, and this is due to the flow velocity. This dry patch is also present in the experimental case. Surface tension effects are also more apparent in the experimental case with more capillary waves present in all the test cases considered.

For the fictitious gas cases (figures H.4, H.9 and H.13) the domain is much larger and the waves exit at the rear of the domain, therefore there is no reflection for any case considered. At Mach numbers of 3.12 and 4.31, the density reduces slightly in the region behind the tail wave.

11.1.2 Depth Profiles

(Figures (10.1)-(10.3))
Consider the case with a Froude or Mach number equal to 2.38. The bow shock/jump locations occur in similar regions for all the cases. The CFD case for the fictitious gas with $\gamma = 2$ shows very good agreement to the theoretical case, with respect to both shock location and density ratio. The location for both the bow and tail waves are in similar regions, the only difference being that the density rise across the shock does not occur over an infinitesimal distance for the CFD fictitious gas case. For the expansion fan, a gradual decrease in pressure is expected, and therefore there is much better agreement for the tail waves/jumps for these two cases. It should be noted that the rear of the wedge has been extended to the rear of the domain, for the CFD fictitious gas cases, therefore the data levels off prematurely due to the exclusion of the wake. Also, for the theoretical cases the graphs are terminated when the flow through the expansion fan is turned back to the freestream direction. There is however excellent agreement between the density ratios for these two cases, with a maximum density ratio of 1.47 for the CFD fictitious gas case and 1.49 for the theoretical case. These maximum depth ratios are less than the maximum depth ratios for all the other cases.

The jumps for the hydraulic cases, both experimental and VOF, also have the jumps in similar locations. The maximum depth ratio occurs for the no surface tension case, with a depth ratio of around 2.07. This may be due to the lack of, or reduced intermolecular forces acting on molecules at the surface. For all the VOF cases, the maximum depth ratio occurs at the bow jump, but for the experimental case the maximum depth ratio occurs at the tail wave, at a

depth ratio of 1.9. The average depth ratio across the wave of the experimental case is much lower than all the other cases, and capillary waves are evident at the bow wave. The wave gradually increases in depth, then remains constant until rapidly increasing at the tail wave. The VOF no wall and wall cases are similar with the only significant difference being the wavelet ahead of the bow jump, seen in the wave profile of the wall case. The no wall case has a lower depth ratio overall compared to the wall case, except for the bow jump, where the no wall case has a higher depth ratio at the peak of the jump.

At a Froude or Mach number of 3.12, the bow and tail shock/jumps occur in similar locations. The CFD fictitious gas case and the theoretical case again show very good agreement, both in wave location as well as density ratios. The bow shock for the CFD fictitious gas case is steeper than the case at a Mach number of 2.38, hence there is better agreement of the bow shock with the theoretical case at this Mach number. The tail wave shows similar behavior although the density drop for the CFD case occurs a short distance before the theoretical prediction of the density drop across the tail wave. The density drop also occurs over a greater distance for the CFD case as opposed to the theoretical case, since the gradient of the graph is higher for the theoretical case. The maximum density ratios again show very good agreement with a maximum density ratio of 1.59 for the CFD gas case and 1.61 for the theoretical case. These density ratios are lower than the maximum depth ratios for the hydraulic cases, with all the hydraulic cases having maximum depth ratios greater than 2. For all the cases considered, the wave profiles are now narrower, compared to the lower Froude/Mach number and hence the waves are steeper, with higher maximum depth ratios due to the increased flow speed. The wave profiles for the no wall and wall case, are again very similar, but the no wall case has a higher average depth ratio for this case. The experimental case has the highest depth ratio at this Froude number, and the bow jump is significantly steeper than the previous Froude/Mach number. The highest depth ratio occurs at the tail wave with a depth ratio of 2.33. The profiles for the VOF cases and the experimental case, again occur in the same region along the plane of analysis.

At a Froude or Mach number of 4.31 the waves again occur in similar locations. The CFD fictitious gas case again shows good agreement to the theoretical case. The bow waves show good agreement, and the tail wave shows

the best agreement from all the Mach numbers considered. The location of the tail wave for the CFD case is slightly ahead of the theoretical case, but the curves appear almost parallel at first, before the CFD case deviates from the theoretical case just before the end of the tail wave. The maximum density ratios show the best agreement of all the Mach numbers considered with a maximum density ratio of 1.79 for the CFD case and 1.8 for the theoretical case. All the waves are again steeper and narrower due to the increased flow speed. The maximum depth ratio is 2.4, and this is for the no wall case, with the wall case having a depth ratio of 2.16 and the experimental case having a depth ratio of 2.19. The waves for the experimental and VOF cases are also in a similar region, although the tail wave of the experimental case occurs further downstream. There is a steep rise at the bow jump, and then a rapid drop in depth, which then increases gradually until rapidly increasing at the tail wave. The VOF wall and no wall cases are similar, with the no wall case having the higher average depth ratio.

A shock wave has infinitesimal thickness, therefore the density profile should appear as a step as seen in the theoretical case, rather than a ramp, as it appears in all the figures ((10.1) to (10.3)) for the CFD fictitious gas case. An examination of the mesh revealed that the mesh resolution was too coarse to detect a shock wave and display it as a step. No adaption was done on the mesh after running the simulations, and some form of adaption, like gradient adaption (around the shock wave region), could allow a more accurate definition of the shock wave. This also applies to the VOF cases, coupled with the effect of surface tension. The slopes of the waves start increasing from zero ahead of the theoretical case due to surface tension. By examining the depth profiles, values given in table (10.1) are therefore more consistent than what they seem. The same applies to the tail waves.

The profiles for the experimental cases are not very smooth due to method of generating these profiles. The thicknesses of the colour bands were measured, and the slopes between the end points of colour bands, along the profile, were combined to generate the slopes. The divisions are based on colour, but more intervals with smaller distances between points would give a smoother profile. This explains the erratic profile generated for the experimental case. This is a shortcoming of the method used, due the inconsistencies in calibration of the intended method. As mentioned before, human error and the quality of

the image are factors in the accuracy of the slope determination, and hence the accuracy is limited. With better calibration, (i.e. using water instead of perspex), image processing software can be used to analyse the images, which would yield more accurate depth profiles for the experimental case. There would be more intervals, since the distance between points would be the width of one pixel, therefore the slope would have better definition and be more accurately represented.

The fictitious gas case has been modelled as inviscid. The dissipative transport processes of viscosity and thermal conduction are therefore neglected. A more representative model would be a model where viscosity is included. Also, only the density ratio was considered for the gaseous case, although from the analogy, temperature ratio is analogous to depth ratio, and pressure ratio is analogous to depth ratio squared. Contours for these variables are different for the gaseous phase, and coupled with the inclusion of viscosity, may produce results closer to the experimental case.

The relationship between the bow wave locations for the different cases is much better than suggested in Table (10.1).

11.2 Dynamic Wedge

A limitation to the experimental dynamic case is that the field of view is small. Recalling from section (9.1), that the size of the colour mask influences the field of view, this effect can be seen in the experimental images. The smallest ring diameter of the colour mask determines the area of the field of view, which is where all the colour rays overlap. In all the experimental images of the dynamic case, the first three colours of the mask, namely blue, red and green, are clearly visible. The first few bands of colour of the colour mask could be eliminated, increasing the area left clear in the centre of the colour mask, which would adversely affect the detection of low surface gradients. This is not as significant for the dynamic case as opposed to the static case though, as the dynamic case is purely for qualitative analysis.

Once the wedge starts moving, the wave starts to form around the leading edge(apex) of the wedge and only extends a short distance from the wedge. Once the wedge has accelerated to maximum velocity, the wave is fully at-

tached to the wedge and the wave now extends toward the end of the domain. The tail wave is also clearly discernible. When the wedge starts slowing down the bow wave starts to detach. As the wave continues slowing down, the wave becomes fully detached and moves ahead of the wedge as the wave speed is greater than the wedge speed. By the time the wedge stops the wave has moved well ahead of the wedge and the tail wave also detaches and moves ahead of the wedge. The wave continues until it moves out of the domain, dissipating as it continues.

The last three figures of the VOF case have no counterpart in the experimental case. After the wedge has stopped, it starts moving again for a short distance before eventually stopping. The wedge motion in the VOF model is frictionless, and the inertia of the water, filling the space left by the displaced water, could be causing the wedge to move again. For the experimental model the wedge does not move again, since there is friction in the system such as the friction between the string around pulley and the pulleys on rail(rust).

The reason for selecting a volume fraction of 0.05 is evident by looking at animations with a volume fraction different to 0.05 in Appendix I. The animations vf0_filled.mpeg and vf0_filled_top.mpeg, are for a volume fraction for water of 0, i.e. just above the water surface. The water surface is slightly distorted once the wedge reaches maximum velocity, and this is due to presence of air in cells at this volume fraction. The animations vf05_filled.mpeg and vf05_filled_front.mpeg, are for a volume fraction of 0.5. For this animation the surface waves are only slightly visible. There is also a large dry patch behind the wedge, indicating that cells in this region do not have a volume fraction of 0.5 at that particular instant, but rather a volume fraction less than 0.05. As the volume fraction decreases, the dry patch behind the wedge becomes smaller at each respective instant as seen in vf025_vf05_vf1_filled.mpeg and vf01_vf025_filled.mpeg. These two animations also show that a combination of different volume fractions does not improve the surface resolution. Since the surfaces are filled, only the top most surface is seen in these two animations. For the purpose of unsteady shallow water, where surface waves are of interest, a filled volume fraction of 0.05 yields the best results.

Chapter 12

Conclusion

The cause of the interference present in images from the experimental case was due to the orientation of the lens. The lens was placed facing the wrong direction. The optical system of the water table has therefore been optimized. With the set-up used, the field of view is limited for the dynamic case, although the use of a different colour mask could optimize the system for dynamic testing.

Qualitatively, with respect to flow features, the fictitious gas case shows the best agreement to the experimental case. The VOF cases shows good agreement at higher Froude numbers. Although wave reflection was not one of the intended objectives, the VOF model is quite capable of handling wave reflection. The VOF model is also quite capable of handling and including the effects of surface tension.

Quantitatively, with respect to the location of the wave along an identical profile, for all cases investigated, the VOF cases show better agreement to the experimental case. None of the models show an exact agreement to the actual depth profile of the wave, although for the VOF cases the waves form in similar regions.

Chapter 13

Recommendations

- The grid for the static case simulations can be adapted until the grid is mesh independent. For dynamic meshing however grid adaption is not available with dynamic layering, so any adaption would have to be done manually in GAMBIT.
- The VOF model could be modelled to be more like the experimental case. A more accurate prediction of the surface tension and wall adhesion for the water table, and also an edge over which water flows as is the case with the water table. A different depth at the outlet as opposed to the inlet so that the flow is restricted causing reflection.
- The calibration of the water table for image processing purposes can be done with water instead of perspex. A thin walled perspex pipe, or any thin walled transparent object that will enclose water and has a known curvature can be used for calibrating. The object should have a fairly large radius of curvature, as this will make calibrating steeper slopes easier.
- The colour mask for dynamic testing should be modified. The inner radius, left clear, should be increased to allow a larger field of view.

References

[1] D. C. Giancoli. *Physics for Scientists and Engineers*. Prentice Hall, Englewood Cliffs, New Jersey, U.S.A, second edition, 1989.

[2] R.A. Serway. *Physics for Scientists and Engineers with Modern Physics*. Saunders College Publishing, Philadelphia, U.S.A., fourth edition, 1996.

[3] Fresnel Technologies. *Fresnel Lenses*. Fresnel Technologies Inc., 2001. Obtained from www.fresneltech.com.

[4] B. Jähne. *Practical handbook on image processing for scientific applications*. CRC Press, 1997.

[5] Makarov B. P. Krishnan H. Rhee, S. H. and V. Ivanov. Assesment of numerical techniques in volume of fluid method for free-surface wave flows. In *9th Symposium on Practical Design of Ships and Other Floating Structures*, Luebeck-Travemuende, Germany, 2004.

[6] M. Carbonaro and V. Van der Haegen. Hydraulic analogy to supersonic flow. *Euravia Symposium*, 2002.

[7] Westley R. Yates A. H. Lilley, G. M. and J. R. Busing. Some aspects of noise from supersonic aircraft. *Journal of the Royal Aeronautical Society*, 57:396–414, June 1953.

[8] E. J. Klein. Interaction of a shock wave and a wedge: an application of the hydraulic analogy. *AIAA Journal*, 3(5):801–808, May 1965.

[9] W. Merzkirch. *Flow Visualization*. Academic Press, N.Y. U.S.A., 1974.

[10] W. Calarese and W. L. Hankey. Self-excited wave oscillations in a water table. *AIAA Journal*, 21(3):372–378, March 1983.

[11] B. W. Skews. Colour encoded visualization applied to the hydraulic analogy for supersonic flow. *8th International Symposium on Flow Visualization*, 1998.

[12] E. Mach. Photography of projectile phenomena in air. *Sitzungberichte der Wiener Akademie*, 95:164, 1887.

[13] E. Joughet. Quelque probleme d'hydrodynamic generale. *Journal de Mathematiques Pures et Appliquees*, 3.1:1, 1920.

[14] D. Riabouchinsky. On the hydraulic analogy to flow of a compressible fluid. *Comptes Rendus de l'Academie des Sciences*, 195:998, 1932.

[15] E. Prieswerk. Application to the methods of gas dynamics to water flows with free surface,part i. flows with no energy dissipation. *N.A.C.A. T.M.*, (934), 1940.

[16] E. Prieswerk. Application to the methods of gas dynamics to water flows with free surface,part ii. flows with momentum discontinuities (hydraulic jumps). *N.A.C.A. T.M.*, (935), 1940.

[17] Linder N. J. Orlin, W. J. and J. G. Bitterly. Application of the analogy between water flow with a free surface and two-dimensional compressible gas flow. *N.A.C.A. T.N.*, (875), 1946.

[18] J. Black and O. P. Mediratta. Supersonic flow investigations with a "hydraulic analogy" water channel. *The Aeronautical Quarterly*, 2:227, 1951.

[19] T. J. Mueller and W. L. Oberkampf. Hydraulic analog for the expansion deflection nozzle. *AIAA Journal*, 5(6):1200–1202, June 1997.

[20] E. V. Laitone. A study of transonic gas dynamics by the hydraulic analogy. *Journal of Aeronautical Sciences*, 19:265–272, 1952.

[21] A. H. Shapiro. Free surface water table. *Princeton Series in High Speed Aerodynamics and Jet Propulsion*, 9:309–321, 1954.

[22] O. P. Gupta. An analytical method for evaluating the optimum depth in hydraulic analogy experiments. *AIAA Journal*, 3(10):1953–1954, October 1965.

[23] C. W. Matthews. The design, operation and uses of the water channel as an instrument for the investigation of compressible flow phenomena. *N.A.C.A. T.N.*, (2008), 1950.

[24] A. K. Pal and B. Bose. Simple method of supersonic flow visualization using water table. *AIAA Journal*, 33(1):181–182, 1995.

[25] Arakeri J. H. Rao, A. Wave structure in the radial film flow with a circular hydraulic jump. *Experiments in Fluids*, 31:542–549, 2001.

[26] K. Kawamata Yamamoto and A. S. Nomoto. Visualization of surface wave by inclined grid moiré topography. In *Flow Visualization, Proceedings of the Fourth International Symposium on Flow Visualization*, pages 791–796, Paris, France, 1987. Hemisphere.

[27] S. L. Rani and M. S. Wooldridge. Quantitive flow visualization using the hydraulic analogy. *Experiments in Fluids*, 27:165–169, 2000.

[28] Lang A. Roesgen, T. and M. Gharib. Fluid surface imaging using microlens arrays. *Experiments in Fluids*, 25:126–132, 1998.

[29] X. Zhang and C. S. Cox. Measuring the two-dimensional structure of a wavy water surafce optically: A surface gradient detector. *Experiments in Fluids*, 17:225–237, 1994.

[30] J. D. Jr. Anderson. *Computational Fluid Dynamics, The Basics with Applications*. MacGraw-Hill, New York, U.S.A., 1995.

[31] J.H. Ferziger and M. Perić. *Computational Methods for Fluid Dynamics*. Springer-Verlag, Berlin, Germany, third edition, 2002.

[32] E.H. Harlow and J.E. Welch. Numerical calculation of time dependent viscous incompressible flow with free surface. *Physics of Fluids*, 8:2182–2189, 1965.

[33] C.W. Hirt and B.D. Nichols. Volume of fluid method for dynamics of free boundaries. *Journal of Computational Physics*, 39:201–221, 1981.

[34] Smereka P. Sussman, M. and S. Osher. A level set approach for computing solutions to incompressible two-phase flow. *Journal of Computational Physics*, 114:146–159, 1994.

[35] FLUENT. *FLUENT 6.2.16 Documentation*. FLUENT Inc., January 2005. Accompanies FLUENT 6.2.16 software. Can also be found at www.fluent.com.

[36] I. N. Levine. *Physical Chemistry*. MacGraw-Hill, New York, U.S.A., fifth edition, 2002.

[37] Saiva G. Archer R. D. Beaton, R. H. and R. A. A. Bryant. Direct diabatic hydraulic analogy. *AIAA Journal*, 4(2):2229–2231, December 1966.

[38] B.W. Skews. *Gas Dynamics Lecture Notes*. University of the Witwatersrand, Johannesburg, South Africa, 2003.

Appendix A

Applications of the Hydraulic Analogy

To illustrate the wide range of applicability of the hydraulic analogy to two-dimensional compressible gas flow, a few examples are mentioned below.

Complex shock interactions can be investigated with the hydraulic analogy. Klein [8] has used the hydraulic analogy to investigate the two-dimensional flow patterns for (i) a strong shock wave striking a wedge in supersonic motion, which has weak attached shocks, (ii) a weak shock wave striking a wedge in supersonic motion which has strong attached shocks, and (iii) a strong shock wave striking a wedge at varying angles of incidence. The experimental flow patterns are compared with theoretical aerodynamic features, showing good overall agreement. Cases (ii) and (iii) are shown in the figures below.

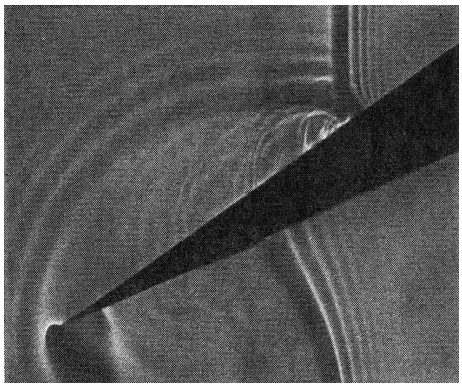

Figure A.1: Stationary wedge, strong incident jump [8]

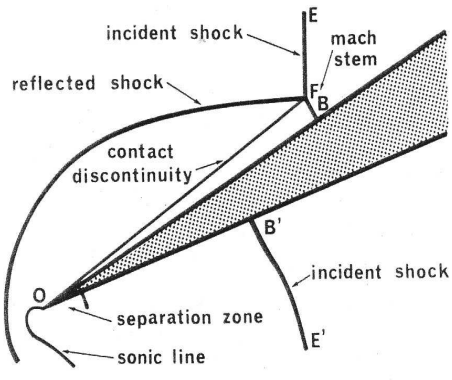

Figure A.2: Stationary wedge, strong incident shock [8]

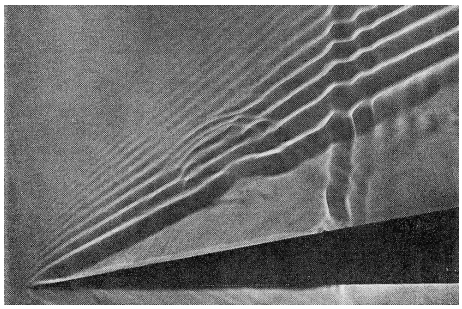

Figure A.3: Strong attached jump, weak incident jump [8]

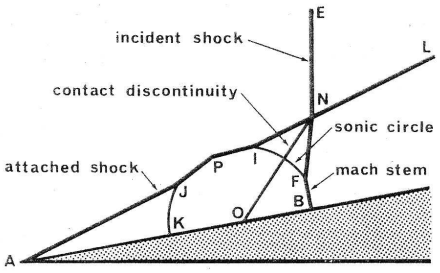

Figure A.4: Strong attached shock, weak incident shock [8]

Mueller and Oberkampf [19] have investigated the flow field of an expansion-deflection nozzle, particularly the separated flow region within the expansion deflection nozzle. Due to the separated flow region, the problem becomes complex, and is more a physical problem, than a mathematical problem, to which the hydraulic analogy is well suited. Similar data for air was not available at the time, so the interpretation of the results, using the hydraulic analogy, provided the only means of describing this type of flow.

Beaton et al. [37] have extended the analogy to investigate thermodynamic effects. They noted that continuous spatially varied open channel flow, where liquid is injected at the base of the channel (i.e. at $d = 0$), is analogous to continuous gas flow with heat addition or extraction taking place over a finite distance. This thermodynamic analogy is only valid under certain conditions, though.

Appendix B

Radiometry

This section is from Jahne [4], *Practical Handbook on Image Processing for Scientific Applications.*

Radiometry is a branch of optics, which describes and measures radiation and its interaction with matter. Geometrical optics only tells us the location of the image of an object, while radiometry tells us how much radiant energy has been collected from an object.

Radiant Energy

Radiation is a form of energy, and can therefore do work. A body absorbing the radiation is heated up, and set free electric charges in a suitable material designed to detect radiation. Radiant energy is denoted by Q and has units of Ws (J) or number of particles (photons).

Radiant Flux

The radiant energy per unit time is the radiant flux. It is important for describing the total energy emitted by a light source per unit time. The radiant flux, Φ is given by,

$$\Phi = \frac{dQ}{dt}$$

Radiant Flux Density

The radiant flux per unit area is the radiant flux density. If the radiant flux is incident upon a surface per unit area, then it is known as irradiance. If the radiation is emitted from a surface the radiant flux density is called the

excitance. Irradiance, E, and excitance, M is given by

$$E = M = \frac{d\Phi}{dA_0}$$

Units are Wm^{-2} or $m^{-2}s^{-1}$.

Solid Angle

The concept of the solid angle, Ω, is best described by understanding the angular distribution of radiation. If a small source of radiation is placed at the center of a sphere, it will emanate radiation in a cone toward the sphere. The source will thus project an area made by the cone on the sphere. The solid angle is this area divided by the square of the radius of the sphere, and is measured in steradians (sr). It is a dimensionless quantity but advisable to be used with radiometry.

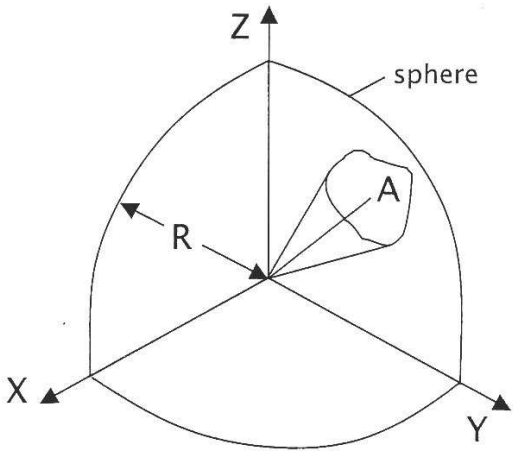

Figure B.1: The solid angle[4]

Radiant Intensity

The total radiant flux per solid angle emitted by a source is called the radiant intensity. This term applies only to point sources, i.e. when the distance from the source is much larger than its extent. Radiant intensity is given by

$$I = \frac{d\Phi}{d\Omega}$$

with units of W/sr or $s^{-1}sr^{-1}$.

Radiance

The radiance is the area and solid angle density of the radiant flux. In simpler terms it is the radiant flux in a specific direction at a specified point on the surface per area projected and per solid angle. The radiation can be incident to, emitted from or pass through a surface. The radiance therefore depends on the angle of incidence to the surface and the azimuth angle. The radiance is therefore described per projected area, which effectively increases with the angle of incidence. The radiance is given by,

$$L = \frac{d^2\Phi}{dA\, d\Omega} = \frac{d^2\Phi}{dA_0\, cos\theta\, d\Omega}$$

Radiance should not be confused with irradiance, even though they have the same dimensions. The radiance describes the angular distribution of radiation while the irradiance integrates the radiance distribution incident on surface element over a solid angle range covering all directions under which it can receive radiation.

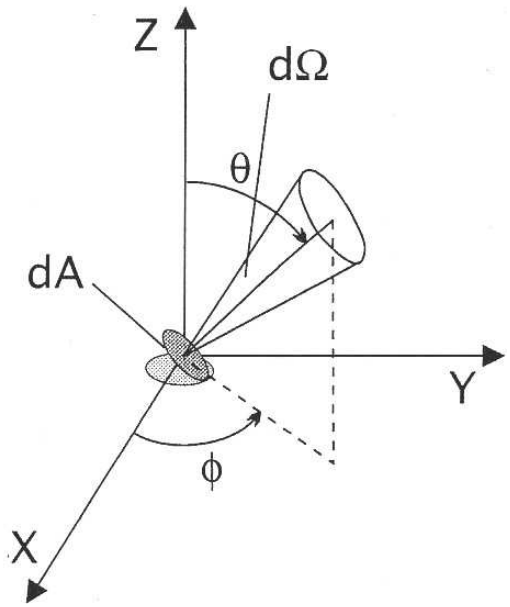

Figure B.2: The concept of radiance[4]

Appendix C

Navier-Stokes Equations

$$\frac{\partial(\rho u)}{\partial t} + \nabla \cdot (\rho u \mathbf{V}) = \frac{\partial p}{\partial x} + \frac{\partial \tau_{xx}}{\partial x} + \frac{\partial \tau_{yx}}{\partial y} + \frac{\partial \tau_{zx}}{\partial z} + \rho f_x \tag{C.1}$$

$$\frac{\partial(\rho v)}{\partial t} + \nabla \cdot (\rho v \mathbf{V}) = \frac{\partial p}{\partial y} + \frac{\partial \tau_{xy}}{\partial x} + \frac{\partial \tau_{yy}}{\partial y} + \frac{\partial \tau_{zy}}{\partial z} + \rho f_y \tag{C.2}$$

$$\frac{\partial(\rho w)}{\partial t} + \nabla \cdot (\rho w \mathbf{V}) = \frac{\partial p}{\partial z} + \frac{\partial \tau_{xz}}{\partial x} + \frac{\partial \tau_{yz}}{\partial y} + \frac{\partial \tau_{zz}}{\partial z} + \rho f_z \tag{C.3}$$

where:

ρ = density
u, v, w = component of velocity
$\mathbf{V}$ = velocity vector
τ_{xx} = normal stress
τ_{xy} = shear stress
f_z = body force per unit mass
p = pressure

Appendix D

Static Experimental Results

Each set of results is given for the table at a specific inclination. This inclination is represented with reference to the base of the collection channel, which is 0 on the masking tape used for reference measurements. The table rotates and thus moves in an arc, but since the angles of inclination are relatively small, a small angle approximation can be applied, and the measurements suffice as a reference.

At a table height of 20.5 cm, when 4 pumps are used, the water height increases and is difficult to measure. There is also a hydraulic jump at the inlet, and the velocity slows down considerably.

Table D.1: Table inclination = 7.5 cm

Number of pumps	5 Pumps	4 Pumps	3 Pumps	2 pumps
Water Height, h (mm)	4.81	4.73	4.23	3.27
Propagation Velocity $\sqrt{gh}$	0.22	0.22	0.20	0.18
Velocity, v (m/s)	0.80	0.93	0.89	0.79
Froude number, Fr	3.69	4.31	4.37	4.44

Table D.2: Table inclination = 12 cm

Number of pumps	5 Pumps	4 Pumps	3 Pumps	2 pumps
Water Height, h (mm)	6.11	5.62	5.34	4.25
Propagation Velocity $\sqrt{gh}$	0.25	0.24	0.23	0.20
Velocity, v (m/s)	0.66	0.76	0.714	0.67
Froude number, Fr	2.70	3.24	3.12	3.28

Table D.3: Table inclination = 13.5 cm

Number of pumps	5 Pumps	4 Pumps	3 Pumps	2 pumps
Water Height, h (mm)	6.14	5.88	5.40	5.06
Propagation Velocity $\sqrt{gh}$	0.25	0.24	0.23	0.20
Velocity, v (m/s)	0.70	0.67	0.68	0.69
Froude number, Fr	2.84	2.78	3.37	3.30

Table D.4: Table inclination = 15 cm

Number of pumps	5 Pumps	4 Pumps	3 Pumps	2 pumps
Water Height, h (mm)	6.75	6.31	5.92	4.5
Propagation Velocity $\sqrt{gh}$	0.257	0.249	0.240	0.210
Velocity, v (m/s)	0.712	0.729	0.645	0.657
Froude number, Fr	2.77	2.93	2.68	3.13

Table D.5: Table inclination = 17 cm

Number of pumps	5 Pumps	4 Pumps	3 Pumps	2 pumps
Water Height, h (mm)	8.21	7.95	7.58	7.11
Propagation Velocity $\sqrt{gh}$	0.277	0.279	0.273	0.264
Velocity, v (m/s)	0.560	0.597	0.546	0.571
Froude number, Fr	2.02	2.14	2.00	2.16

Table D.6: Table inclination = 20.5 cm

Number of pumps	5 Pumps
Water Height, h (mm)	6.11
Propagation Velocity $\sqrt{gh}$	0.25
Velocity, v (m/s)	0.66
Froude number, Fr	2.70

Appendix E

MATLAB Code

E.1 Ray Tracing

```
n1=1;                %refractive index of air
n2=1.49;             %refractive index of lens
n3=1.52;             %refractive index of glass
n4=1.33;             %refractive index of water
r=input('Enter radius of light ray at the source (mm): ')
f=784
theta1=atan(r/f)
%this is angle in the vertical plane of the source ray
theta1_degrees=theta1*180/pi%incidence angle
theta2=(asin((n1/n2)*sin(theta1)))%at the air/lens interface
theta2_degrees=theta2*180/pi
theta3=(asin((n2/n1)*sin(theta2)))%at the lens/air interface
theta3_degrees=theta3*180/pi
theta4=(asin((n1/n3)*sin(theta3)))%at the air/glass interface
theta4_degrees=theta4*180/pi
theta5=(asin((n3/n4)*sin(theta4)))%at the glass/water interface
theta5_degrees=theta5*180/pi
ws=input('Enter the slope of the water at the surface (degrees):')
%where ws is the water slope
if ws==0
    theta6=(asin((n4/n1)*sin(theta5)))%at the water/air interface
    theta6_degrees=theta6*180/pi
else
```

```
    theta5_prime_degrees=theta5-ws
%angle of the beam just beneath the water surface
%measured from the normal to the water surface slope
    theta5_prime=theta5_prime_degrees*pi/180
    theta6=(asin((n4/n1)*sin(theta5_prime)))
%at the water/air interface, i.e. theta exit
    theta6_degrees=theta6*180/pi
end
%Distances between each element in the optical system
a=784;
b=6;
c=3.175;
d=200;
e=12;
f=5;
l1=a*tan(theta1); %theta1 is in degrees
l2=b*tan(theta2);
l3=c*tan(theta3);
l4=c*tan(theta4);
l5=c*tan(theta5);
l6=c*tan(theta6);
rexit=r-(l1+l2+l3+l4+l5+l6)
```

E.1.1 Maximum angle apparatus can detect

```
R=450;
f=784;
n1=1;%refractive index for air
n2=1.52;%refractive index for glass
n3=1.33;%refractive index for water
n4=1;%refractive index for air
beta=atan(R/f);
theta2=asin((n1/n2)*sin(beta));
theta3=asin((n2/n3)*sin(theta2))
theta3degrees=theta3*180/pi
thetaw=atan((n3/n4)*sin(theta3)/(n3/n4*cos(theta3)-1))
thetawdegrees=thetaw*180/pi
```

E.2 Fictitious Gas Properties

E.2.1 Assuming M to find c_p

```
clear all
clc
g=2
Rmol=8.3143
cpmol=g*Rmol/(g-1)
cvmol=Rmol/(g-1)
R=0.287
%M=28.97 having R or M constant is the same thing
%R=Rmol/M
M=Rmol/R
cp=cpmol/M
cv=cvmol/M
```

E.2.2 Assuming c_p to find M

```
clear all
clc
g=2
cp=1.00643
cv=cp/2
R=cp-cv
Rmol=8.3143
M=Rmol/R
```

E.2.3 Total Pressure and Temperature

```
%this code works out the temperature and pressure
%at a given Mach number for gamma=2
clear all
clc
M=input('Enter the Mach Number:  ')
p0=101325*(1+0.5*M^2)^2
T0=(1+0.5*M^2)*300
```

E.3 Image Processing

To calibrate the perspex half cylinder, we need the intensities of each band of colour. Since there are two bands for each colour, one on either side of the cylinder, we find the intensities for each band and get the range of intensities for that particular colour.This procedure is done for each colour.
Intensity for the first colour band.

```
%First file to be used, with the file 'recognition1'
%following this one. Generates intensity matrices
%for the colour bar on one side of the cylinder,
%and recognition1 does the other side.
clear all,
clc
I=imread('C3a.bmp');
imshow(I)
whos %Info about the image
info = imfinfo('C3a.bmp') %Info about the image
c1=improfile(86)%The different intensities for
%r,g,b along a line selected with a mouse.
%In this case the line would be on the colour
%bar of interest on the perspex half-cylinder.
%c1 is a set of three matrices of intensities
%for each colour.
```

Intensity for the second colour band.

```
%second file to be used, following 'recognition'.
%Generates intensity matrices for the colour
%bar on the other side of the cylinder,
%and recognition does the first side.
clc
I=imread('c3a.bmp');
imshow(I)
whos%Info about the image
info = imfinfo('c3a.bmp')%Info about the image
c2=improfile(86)%intensity matrices
```

The minimum and maximum intensity ranges for each colour are then taken from the `c1` and `c2` matrices. Starting with the clear band in the centre of

the half-cylinder,since there is only one band, the intensity range is found as follows. There is one matrix for red, one for green and and one for blue, so the range is found for each matrix.

```
max11=max(c1(:,:,1))
min11=min(c1(:,:,1))
max12=max(c1(:,:,2))
min12=min(c1(:,:,2))
max13=max(c1(:,:,3))
min13=min(c1(:,:,3))
```

For the rest of the colour bands, each colour having two bands, the intensity range is found, again from `c1` and `c2`.

```
max11=max(c1(:,:,1));
min11=min(c1(:,:,1));
max12=max(c1(:,:,2));
min12=min(c1(:,:,2));
max13=max(c1(:,:,3));
min13=min(c1(:,:,3));
max21=max(c2(:,:,1));
min21=min(c2(:,:,1));
max22=max(c2(:,:,2));
min22=min(c2(:,:,2));
max23=max(c2(:,:,3));
min23=min(c2(:,:,3));
max1=max(max11,max21)
min1=min(min11,min21)
max2=max(max12,max22)
min2=min(min12,min22)
max3=max(max13,max23)
min3=min(min13,min23)
```

Since the dimensions of the half-cylinder are known, the range of slopes for each colour band can be found.

```
%Slope-Colour Calibration
%total length=69mm
%measured length=98 units
%therefore each unit = 69/.98 mm
```

```
clear all,clc
af=69/0.98
a1=[0 .1 .14 .18 .23 .28 .35 .44 .49 .56 .6 .66
.73 .78 .82 .86 .9 .98]
A1=af.*a1 %actual distance in mm
a2=A1+.5 % since perspex is only 69mm at the base,
%but diameter of the perspex cylinder is 70.
%You would therefore not be able to use the
%radius in calculations.If the range was from
%0 to 70 then the cylinder can be placed at
%the origin starting from 0 to 70 and
%the radius can be used. We therefore correct
%the x-values first.
%x=[0 0.5000    7.5408   10.3571   13.1735
16.6939   20.2143   25.1429   31.4796
35.0000   39.9286   42.7449 46.9694
51.8980   55.4184   58.2347   61.0510
63.8673   69.5000 70]
%x now across the entire range from 0 to 70.
x=[0 7.5408   10.3571   13.1735   16.6939
20.2143   25.1429   31.4796   35.0000
39.9286   42.7449 46.9694   51.8980
55.4184   58.2347   61.0510   63.8673   70]
r=35
%Using pythagoras, the y co-ordinate can be found.
if x<=35
y=(r^2-x.^2).^(1/2)
else
    y=(r^2-(x-35).^2).^(1/2)
end
X=diff(x);%Calculates differences between
%adjacent elements of X. If X is a vector,
%then diff(X) returns a vector, one element
%shorter than X, of differences between
%adjacent elements: [X(2)-X(1) X(3)-X(2)...
% ... X(n)-X(n-1)]
Y=diff(y);same as with x.
```

```
s=Y./X;
slope=atan(s);
slope_degrees_perspex=slope.*(180/pi)
slope_degress_water=slope_degrees_perspex*1.138
%where 1.138 is the average conversion factor
%for a ray exiting perspex to find the equivalent
%exit from water.
%The conversion is done as follows:
warning off MATLAB:divideByZero
theta1_degrees=-90:10:90
theta1=theta1_degrees*pi/180
theta2_p=asin(sin(theta1)/1.49)
theta2_w=asin(sin(theta1)/1.33)
t2=theta2_w./theta2_p
t1=[1.1565    1.1547    1.1497    1.1433
1.1367    1.1309    1.1262    1.1229
1.1210    1.1210   1.1229    1.1262
1.1309    1.1367    1.1433    1.1497
1.1547    1.1565]
t=mean(t1)
```

We then find the colour corresponding to each slope.

```
for r=1:86

    if  ((116<c1(r,1) & c1(r,1)<133) &
     (114<c1(r,2) & c1(r,2)<131) &
     (124<c1(r,3) & c1(r,3)<148))
disp('Colour=Clear. Therefore slope
3.2847<=slope_degrees<-4.6061')

elseif ((94 < c1(r,1) & c1(r,1) < 125) &
 (95 < c1(r,2) & c1(r,2) < 126) &
 (127 < c1(r,3) & c1(r,3) < 172))
    disp('Colour=Blue. Therefore slope
     12.5922<=slope_degrees<3.28474
     or -4.6061<=slope_degrees<-11.8805')

elseif ((121<c1(r,1) & c1(r,1)<160) &
```

```
(85<c1(r,2) & c1(r,2)<126) &
(86<c1(r,3) & c1(r,3)<125))
    disp('Colour=Red. Therefore slope
     23.5264<=slope_degrees<12.5922
     or -11.8805<=slope_degrees<-18.65301')

elseif ((106<c1(r,1) & c1(r,1)<128) &
(115<c1(r,2) & c1(r,2)<143) &
(78<c1(r,3) & c1(r,3)<116))
    disp('Colour=Green. Therefore slope
     32.1628<=slope_degrees<23.5264
     or -18.6530<=slope_degrees<-27.8048')

elseif ((122<c1(r,1) & c1(r,1)<144) &
(103<c1(r,2) & c1(r,2)<121) &
(91<c1(r,3) & c1(r,3)<129))
    disp('Colour=Orange. Therefore slope
     39.8962<=slope_degrees<32.1628
     or -27.8048<=slope_degrees<-36.7331')

elseif ((108<c1(r,1) & c1(r,1)<135) &
(99<c1(r,2) & c1(r,2)<116) &
(105<c1(r,3) & c1(r,3)<151))
    disp('Colour=Purple. Therefore slope
     47.4182<=slope_degrees<39.8962
     or -36.7331<=slope_degrees<-43.9740')

elseif ((107<c1(r,1) & c1(r,1)<138) &
(101<c1(r,2) & c1(r,2)<133) &
(69<c1(r,3) & c1(r,3)<124))
    disp('Colour=Yellow. Therefore slope
     54.8712<=slope_degrees<47.4182
     or -43.9740<=slope_degrees<-51.0360')

elseif ((100<c1(r,1) & c1(r,1)<122) &
(92<c1(r,2) & c1(r,2)<117) &
(84<c1(r,3) & c1(r,3)<131))
```

```
    disp('Colour=Pink. Therefore slope
     80.6153<=slope_degrees<54.8712
     or -51.0360<=slope_degrees<-58.9862')

elseif ((92<c1(r,1) & c1(r,1)<117) &
(87<c1(r,2) & c1(r,2)<108) &
(93<c1(r,3) & c1(r,3)<122))
    disp('Colour=Black. Therefore slope
    90<slope_degrees<80.6153 or
    -58.9862<=slope_degrees<-90')
else
    disp('Not within calibrated range!!')
end

end
```

Appendix F

FLUENT

F.1 Setting up the stationary wedge case

1. FLUENT Version → 3D
2. Read → Case → real wedge.msh (read mesh file into FLUENT)
3. Grid → Check
4. Grid → Scale → mm (depending on the units the mesh was created in)
5. Define → Models → Solver
    - Solver → Segregated
    - Formulation → Implicit
    - Space → 3D
    - Time → Steady
    - Velocity Formulation → Absolute
    - Gradient Option → Cell Based
    - Porous Formulation → Superficial Velocity
6. Define → Models → Multiphase
    - Model → Volume of Fluid
    - Number of Phases → 2
    - VOF Parameters → VOF Scheme → Implicit, check Open Channel Flow
    - Body Force Formulation → Implicit Body Force

7. Define → Materials
    - Fluent Database → select *water-liquid [h20 <l>]* from the drop-down list
    - Copy
    - click Change/Create in the Materials window
8. Define → Phases
    - primary-phase → Set...
        - Name → air
        - Phase Material → air → OK
    - Interaction
        - check Wall Adhesion
        - Surface Tension → 0.07305
    - secondary-phase → Set...
        - Name → water
        - Phase Material → water-liquid → OK
    - Interaction
        - check Wall Adhesion
        - Surface Tension → 0.07305
9. Define → Operating Conditions
    - Pressure → Operating Pressure (Pascal) → 101325
    - Reference Pressure Location
        - X(m)→ 0
        - Y(m)→ 0
        - Z(m)→ 0.2
    - Gravity
        - check Gravity
        - Gravitational Acceleration
            * X (m/s^2) → 0
            * Y (m/s^2) → 0
            * Z (m/s^2) → -9.81

- Variable-Density Parameters
  - check Specified Operating Density
  - Operating Density (kg/m^3) → 1.225

10. Define → Boundary Conditions
    - Inlet → Pressure Inlet → Set
      - check Open Channel
      - Secondary Phase for Inlet → water
      - Flow Specification Method → Free Surface Level and Velocity
      - Free Surface Level (m) → enter water depth (e.g. 0.005)
      - Bottom Level (m) → 0
      - Velocity Magnitude → enter velocity magnitude → constant
      - Direction Specification Method → Direction Vector
      - Coordinate System → Cartesian (X,Y,Z)
      - Y-component of Flow Direction → 1 (X and Z are 0)
    - Outlet → Pressure Outlet → Set
      - check Open Channel
      - Pressure Specification Method → Free Surface Level
      - Free Surface Level (m) → enter water depth (e.g. 0.005)
      - Bottom Level (m) → 0
      - Backflow Direction Specification Method → Direction Vector
      - Coordinate System → Cartesian (X,Y,Z)
      - Y-component of Flow Direction → 1 (X and Z are 0)
    - **NB** The surface parallel to the water surface and open to the atmosphere should be specified as a symmetry plane and **not** a pressure inlet.

11. Solve → Controls → Solution
    - Equations → select both Flow and Volume Fraction
    - Pressure-Velocity Coupling → SIMPLE
    - Under Relaxation Factors → set between 0.2 and 0.5.
    - Discretization
      - Pressure → Body Force Weighted or PRESTO!

  - Momentum → First Order Upwind
  - Volume Fraction → Modified HRIC, Second Order Upwind or QUICK.

12. Adapt → Region
    - from (0; 0; 0) to (0.2; 0.8; 0.005)
    - Mark
13. Solve → Initialize → Initialize ...
    - Compute From → Inlet
    - Apply → Init
14. Solve → Initialize → Patch
    - Setting the Volume Fraction
      - Phase → Water
      - Select Volume Fraction
      - Value → 1
      - Registers to Patch → hexahedron-r0 (from marked region in step 11)
      - Patch
    - Setting the Velocity
      - Phase → Mixture
      - Select Y-Velocity
      - Value → of velocity (if in -y direction then negative)
      - Zones to Patch → fluid
      - Patch
15. Solve → Monitors → Residual ...
    - Plot
    - Reduce convergence criteria to 1e-09
16. Solve → Iterate → 5000 iterations → Apply
17. File → Write → Case and Data ... → OK
18. Solve → Iterate → Iterate

F.1.1 Post Processing

To create a plane 25 mm from the rear end of the wedge, parallel to the flow:

- Surface → Quadric
  - $ix = 1$
  - $iy = 0$
  - $iz = 0$
  - $distance = 0.025\,m$
- Specify a surface name
- Create

To view the depth profile along the plane created:

- Display → Contours
  - Contours of → Phases... → Volume Fraction
  - Phase → Water
  - Surface → Select the plane created
- Display

F.2 Dynamic wedge case

F.2.1 Velocity Profile

The motion of the wedge is one-dimensional and FLUENT allows the motion to be described by a velocity profile i.e. the points from a velocity-time graph. Once the velocity profile has been found, the velocity and corresponding times are defined. The profile used for this simulation was based on a falling weight accelerating the wedge, as is the case for experimentation. For experimentation, the wedge is accelerated by a falling weight, both being connected to the pulley and rail system. Thus the motion that is modelled is very similar to the actual motion.

```
((wedge_stop 5 point)
(time 0
0.53
1.06
1.59
2.21)
(v_x 0
0.33
0.66
0.33
0)
)
```

F.2.2 Setting up the dynamic wedge case

The set up for the dynamic wedge case is essentially the same as the stationary wedge case,with the following additional steps.

1. After reading the mesh file,
   Read → Profile → Files of type → All files → *filename*.txt (e.g. wedge.txt, name of text file of velocity profile)

2. Define → Dynamic Mesh → Parameters ...

   - Models → Check Dynamic Mesh
   - Mesh Methods → Layering
   - Layering Tab
     - Options → Select Constant Height
     - Split Factor → 0.7
     - Collapse Factor → 0.5
   - OK

3. Define → Dynamic Mesh → Zones ...
   The Zones which need to be defined are *fluid*, *wedge*, *inlet* and *outlet*.

   - For the zones *fluid* and *wedge*:
     - Type → Rigid Body
     - Motion UDF/Profile → *filename* (e.g. wedge, from name of text file of velocity profile)

- Center of Gravity Location → can enter centre of gravity location (will be mesh dependent), not necessary since there is no rotation.

- For the zones *inlet* and *outlet*:
  - Type → Stationary
  - Meshing Options → Cell Height (m) → Enter ideal cell height (e.g. 0.00725)

4. Solve → Mesh Motion ...

   - Time Step Size (s) → 0.015 (mesh dependent)
   - Number of Time Steps → 175 (velocity profile dependent)

F.2.3 Animating the Motion

If an image is saved of the motion at a specified time or iteration, a series of frames for the motion will be created. These images can then be combined to make an animation. The wave patterns can then be seen in real-time. ImageMagick software was used to do this. ImageMagick is open source software and can be downloaded, at no cost, from http://www.imagemagick.org/.

Procedure in FLUENT

The dynamic wedge case has to be set up in FLUENT first before the procedure below can be done. What is required from FLUENT is that the images be saved in a format which can be used by ImageMagick to make the animation.

1. Display Options

   - Graphics Window
     - Active Window → 1 → Open

2. Solve → Animate → Define
   Solution Animation

   - Enter a name for the sequence
   - Specify the number of iterations or time steps when a frame is saved.
   - Define
     - Storage Type → PPM Image

- Display Type → Select what you want to see
  For this example an iso-surface of volume fraction for water equal to 0.05 was created. The reason being that close to the air-water interface, the volume fraction of water approaches 0 and the surface waves are of interest, from the analogy. Then Contours → Phases → Volume Fraction → Select only the iso-surface for volume fraction = 0.05 → check Filled → click Display → Adjust the Display window to the desired view of the wedge.
- Window → 1 → Set
- OK

3. The procedure can be repeated to have as many Animation Sequences as is desired.

4. After the simulation is complete
   Solve → Animate → Playback

   - Select the Sequence
   - Write/Record Format → Hardcopy Files
   - Hardcopy Options ...
     - Format → Tiff
     - Colouring → Colour
     - Options → check Landscape Orientation
     - Resolution
       Width → 1024
       Height → 768
     - Apply
     - Save → Filename ending with %i or %t.tif for iteration or time step respectively.
   - Write (the images will be saved where specified or the default is in the same folder as the case/data files.)

Procedure in ImageMagick

NB This assumes ImageMagick®has already been installed.

1. Open the Command Prompt
   (In Windows 2000) Start → Programs → Accessories → Command Prompt
   Make sure that the images are in the working directory else you have to change directories or copy the images to the working directory. Also ensure that enough memory is available in the chosen directory.

2. In the Command Prompt Window, type:

   ```
   mogrify -format gif *.tif
   ```

   This converts the TIFF files created in FLUENT to GIF files.

3. Then type:

   ```
   convert -adjoin *.gif animation_name.mpeg
   ```

   This joins all the GIF files to an animation named *animation_name.mpeg*. The animation can be given any name in place of *animation_name*, and the extension *.mpeg* can also be changed to *.avi*.

4. An animation should now be created in the same directory as the images.

Appendix G

Oblique Shock Waves

This section is taken from Skews [38].

Oblique shock waves occur when a supersonic compressible floe is turned into itself. consider the situation in figure (G.1). An initially supersonic compressible flow is turned through a finite angle θ by a corner. Since the presence of the corner cannot be sensed by the flow upstream, the flow adjusts to the change in direction imposed by the wall across an oblique shock wave. Since the flow is being turned into itself by the wall, the oblique shock is a compressive shock wave and generates higher static temperatures and pressures while at the same time causing a drop in the Mach number.

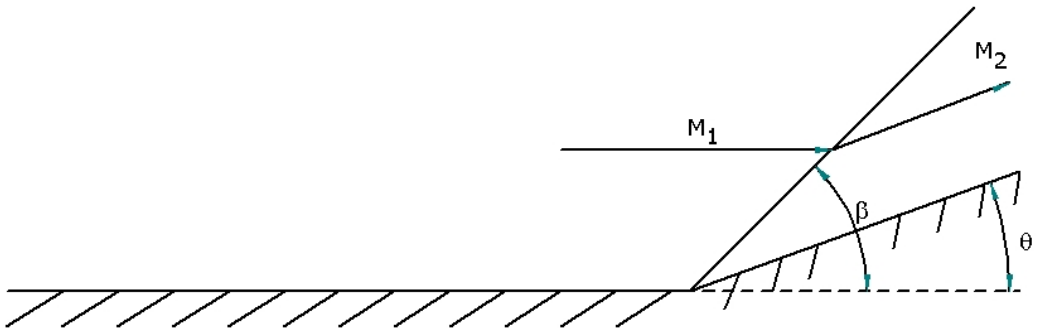

Figure G.1: Supersonic flow over a concave corner

If the flow is turned away from itself, an expansion fan is generated. Consider the situation sketched in figure (G.2). The expansion wave fans out, away from the surface. An expansion wave is the opposite of an oblique shock wave and the flow through the expansion fan is continuous and adjusts smoothly to the downstream conditions. The Mach number increases across the expansion

wave with an associated decrease in the static temperature and pressure.

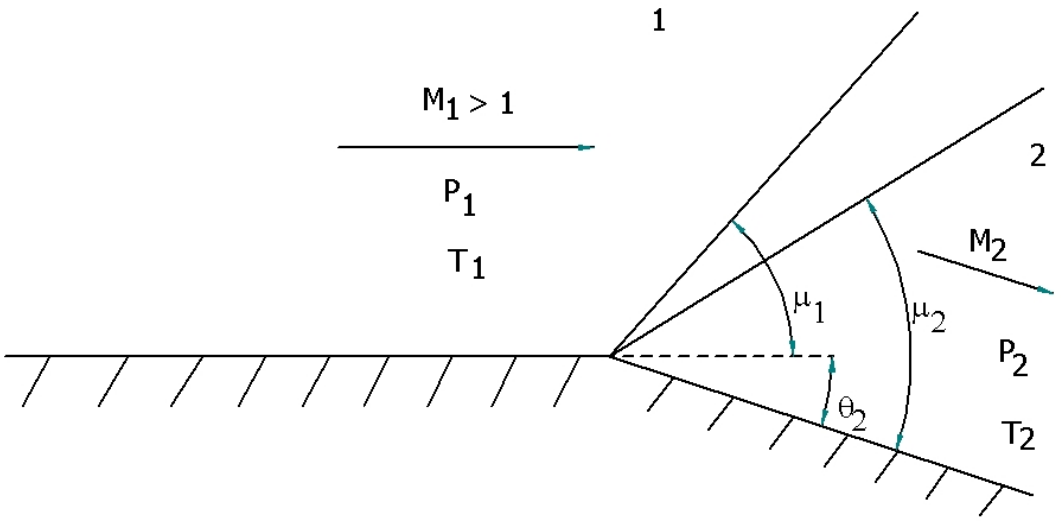

Figure G.2: Supersonic flow around a convex corner

G.1 Derivation of the fundamental equations for oblique shock waves

In order to derive the governing equations, we make use of the control volume shown in figure (G.3). The governing equations can be derived by application of the Reynolds Transport Theorem to the control volume.

G.1.1 Conservation of Mass

$$0 = \iint \rho(\vec{V} \cdot \vec{n}) dA \tag{G.1}$$

Since there is no mass flux across the sides of the control volume, the double integral collapses into the following algebraic equation:

$$0 = \rho_2 V_{n2} A - \rho_1 V_{n1} A \tag{G.2}$$

where V_{n1} and V_{n2} are the normal components of velocity as seen in figure (G.3). Conservation of mass across the oblique shock is the same as that across a normal shock in one dimensional flow, only here it is the normal component of velocity that contributes:

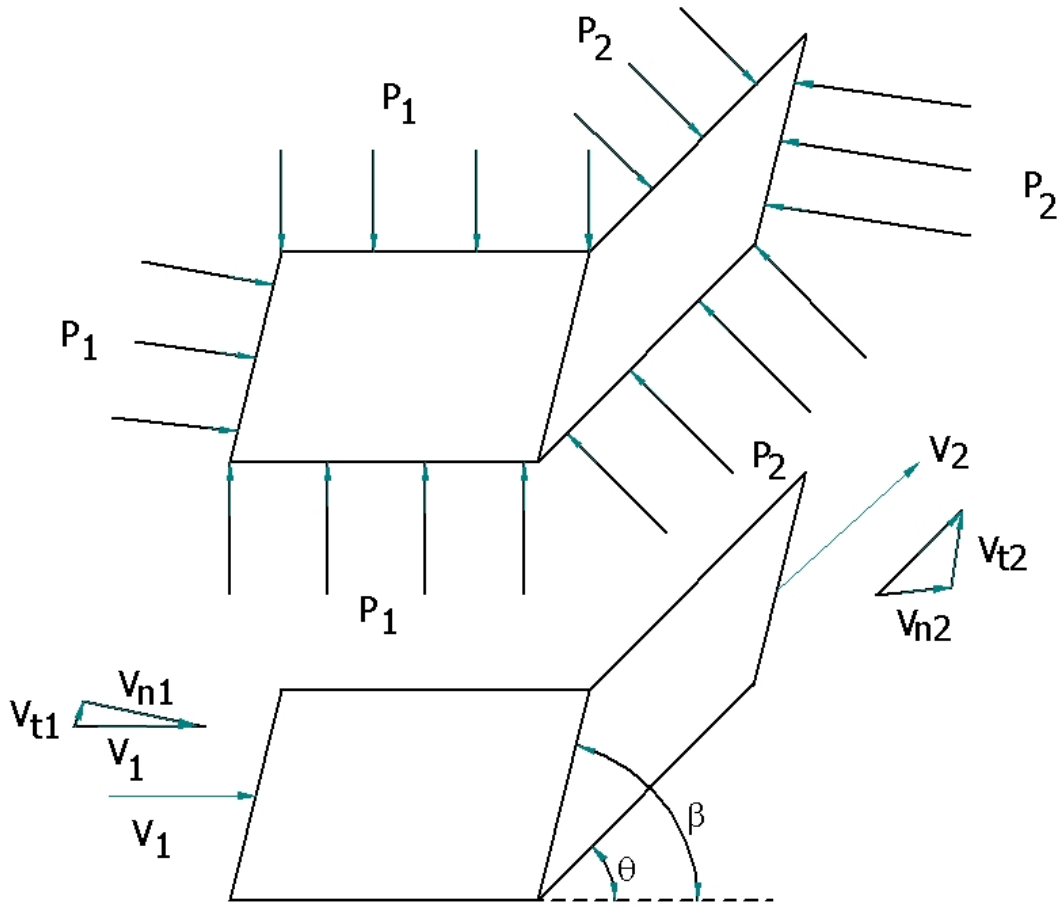

Figure G.3: Control volume for oblique shock analysis

$$\rho_1 V_{n1} = \rho_1 V_{n2} \tag{G.3}$$

G.1.2 Conservation of Linear Momentum

$$\sum \vec{F} = \iint \rho \vec{V}(\vec{V} \cdot \vec{n}) dA \tag{G.4}$$

This vector equation can be separated into two components, one normal to the oblique shock and one tangential to the oblique shock. The scalar equation tangential to the oblique shock becomes:

$$\sum F_t = \rho_2 V_{t2} V_{n2} A - \rho_1 V_{t1} V_{n1} A \tag{G.5}$$

Noting that there is no component of force in the tangential direction and using the continuity equation, this reduces to:

$$V_{t2} = V_{t1} \tag{G.6}$$

Thus there is no change in the tangential component of velocity across the oblique shock.
The scalar equation normal to the shock wave becomes:

$$\sum F_n = \rho_2 V_{n2}^2 A + \rho_1 V_{n1}^2 A \tag{G.7}$$

Performing the force balance gives:

$$P_1 A - P_2 A = \rho_2 V_{n2}^2 A + \rho_1 V_{n1}^2 A \tag{G.8}$$

Eliminating the area which is clearly the same on both sides of the equations gives the more familiar equation:

$$P_1 + \rho_1 {V_{n1}}^2 = P_2 + \rho_2 {V_{n2}}^2 \tag{G.9}$$

Note the similarity between the momentum conservation equation for the one dimensional flow and that for the oblique shock. They are identical except that the normal component of velocity appears in the case of the oblique shock.

G.1.3 Conservation of Energy

The energy equation for steady adiabatic flow across an oblique shock becomes:

$$\delta m(h_1 + \frac{{V_1}^2}{2}) = \delta m(h_2 + \frac{{V_2}^2}{2}) \tag{G.10}$$

Where the conditions at position 1 refer to the flow entering the left hand face of the control volume and conditions at position 2 refer to conditions leaving the right hand face of the control volume. Since the mass flux across these faces is identical (there is no mass flux across the sides of the control volume), we can cancel the differential mass term:

$$h_1 + \frac{{V_1}^2}{2} = h_2 + \frac{{V_2}^2}{2} \tag{G.11}$$

Where V_1 is the magnitude of the inlet velocity and V_2 is the magnitude of the exit velocity. We can write the velocity terms as:

$${V_1}^2 = V_{n1}^2 + V_{t1}^2 \tag{G.12}$$

$${V_2}^2 = V_{n2}^2 + V_{t2}^2 \tag{G.13}$$

Noting that the tangential component of velocity does not change across the shock wave, the energy equation becomes:

$$h_1 + \frac{V_{n1}^2}{2} = h_2 + \frac{V_{n2}^2}{2} \tag{G.14}$$

The Reynolds Transport Theorem yields three relations which represent the fundamental conservation principles for an oblique shock. These are:

Continuity

$$\rho_1 V_{n1} = \rho_2 V_{n2} \tag{G.15}$$

Momentum

$$P_1 + \rho_1 {V_{n1}}^2 = P_2 + \rho_2 {V_{n2}}^2 \tag{G.16}$$

Energy

$$h_1 + \frac{{V_{n1}}^2}{2} = h_2 + \frac{{V_{n2}}^2}{2} \tag{G.17}$$

These relations are identical to those used for the normal shock in a one di-

mensional flow, the only difference being that it is the normal component of velocity that appears in the equations. In other words the normal shock tables will hold for the normal component of flow across the oblique shock. The concept of transforming an oblique shock into a normal shock is outlined in figure (G.4). From the figure it is clear that:

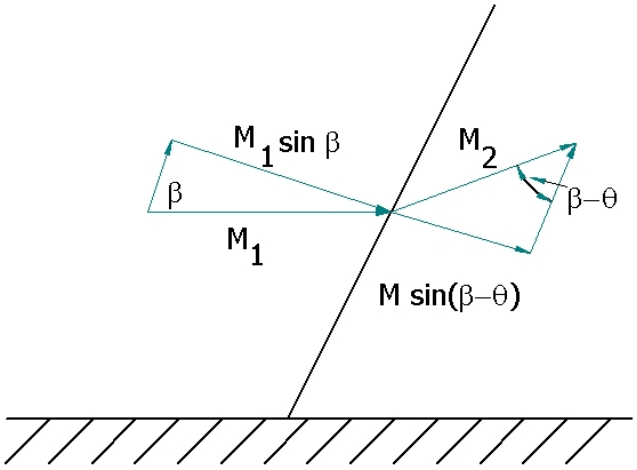

Figure G.4: Transforming an oblique shock into a normal shock

$$M_{n1} = M_1 \sin(\beta) \tag{G.18}$$

$$M_{n2} = M_2 \sin(\beta - \theta) \tag{G.19}$$

We can derive the equations governing the flow across an oblique shock by manipulating the continuity, momentum and energy equations. Starting with the momentum equation:

$$\frac{P_1}{P_2} = \frac{1 + \gamma {M_2}^2 \sin^2(\beta - \theta)}{1 + \gamma {M_1}^2 \sin^2 \beta} \tag{G.20}$$

The energy equation can also be manipulated to give:

$$\frac{T_1}{T_2} = \frac{[1 + \frac{\gamma-1}{2} {M_2}^2 \sin^2(\beta - \theta)]}{1 + \frac{\gamma-1}{2} {M_1}^2 \sin^2 \beta} \tag{G.21}$$

These equations can be combined with the continuity equation, as was done for the normal shock, to give the relation between the upstream and downstream Mach numbers.

$$M_2 \sin(\beta - \theta) = \left[\frac{\frac{2}{\gamma-1} + {M_1}^2 \sin^2 \beta}{\frac{2\gamma}{\gamma-1} {M_1}^2 \sin^2 \beta - 1} \right]^{\frac{1}{2}} \tag{G.22}$$

We can thus determine all the downstream properties, provided that the angles β and θ are known. The angle θ will usually be determined by the physical geometry, but is do we solve for β? If we make use of the geometry it is clear that:

$$\tan(\beta) = \frac{V_{n1}}{V_{t1}} \tag{G.23}$$

$$\tan(\beta - \theta) = \frac{V_{n2}}{V_{t2}} \tag{G.24}$$

Noting that there is no change in the tangential component of velocity across the shock wave, we can write:

$$\frac{\tan \beta}{tan(\beta - \theta)} = \frac{V_1 \sin \beta}{V_2 \sin(\beta - \theta)} \tag{G.25}$$

This can be written as:

$$\frac{\tan \beta}{tan(\beta - \theta)} = \frac{M_1 \sin \beta}{M_2 \sin(\beta - \theta)} \sqrt{\frac{T_1}{T_2}} \tag{G.26}$$

If the term $\frac{T_1}{T_2}$ is eliminated (by using the energy equation) then the following relation can be obtained:

$$\tan \theta = 2 \cot \beta \left[\frac{{M_1}^2 sin^2(\beta) - 1}{{M_1}^2(\gamma + \cos(2\beta)) + 2} \right] \tag{G.27}$$

This is known as the $\theta - \beta - M$ relation and specifies θ as a unique function of M_1 and β.

Knowing the shock wave angle, allows the density to be determined. Since an oblique shock acts as a normal shock to the flow perpendicular to it, the relations for normal shocks are applicable provided M_1 and M_2 are replaced by their normal components, $M_1 \sin \beta$ and $M_2 \sin(\beta - \theta)$. Therefore the density is given by,

$$\frac{\rho_2}{\rho_1} = \frac{(\gamma + 1){M_1}^2 \sin^2 \beta}{(\gamma - 1){M_1}^2 \sin^2 \beta + 2} \tag{G.28}$$

Appendix H

Stationary Wedge Images

For all the VOF cases, a volume fraction of 0.05 is used to display the results, just as with the dynamic case. The contours shown for the fictitious gas are contours of pressure.

H.1 Fr or M = 2.38

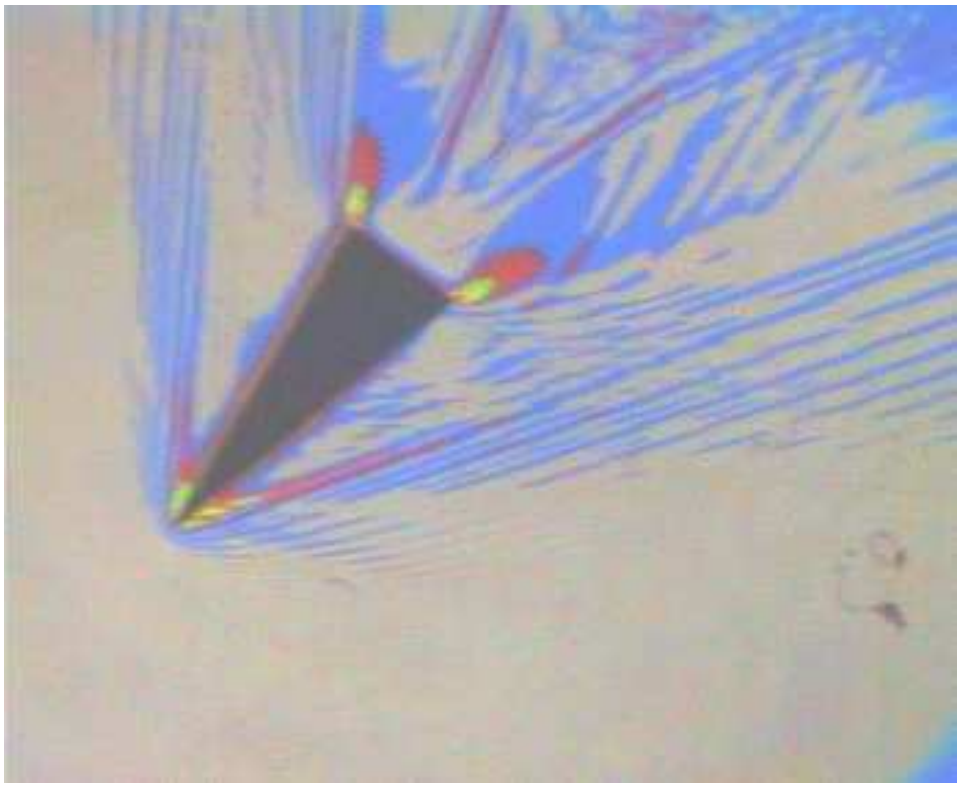

Figure H.1: Experimental

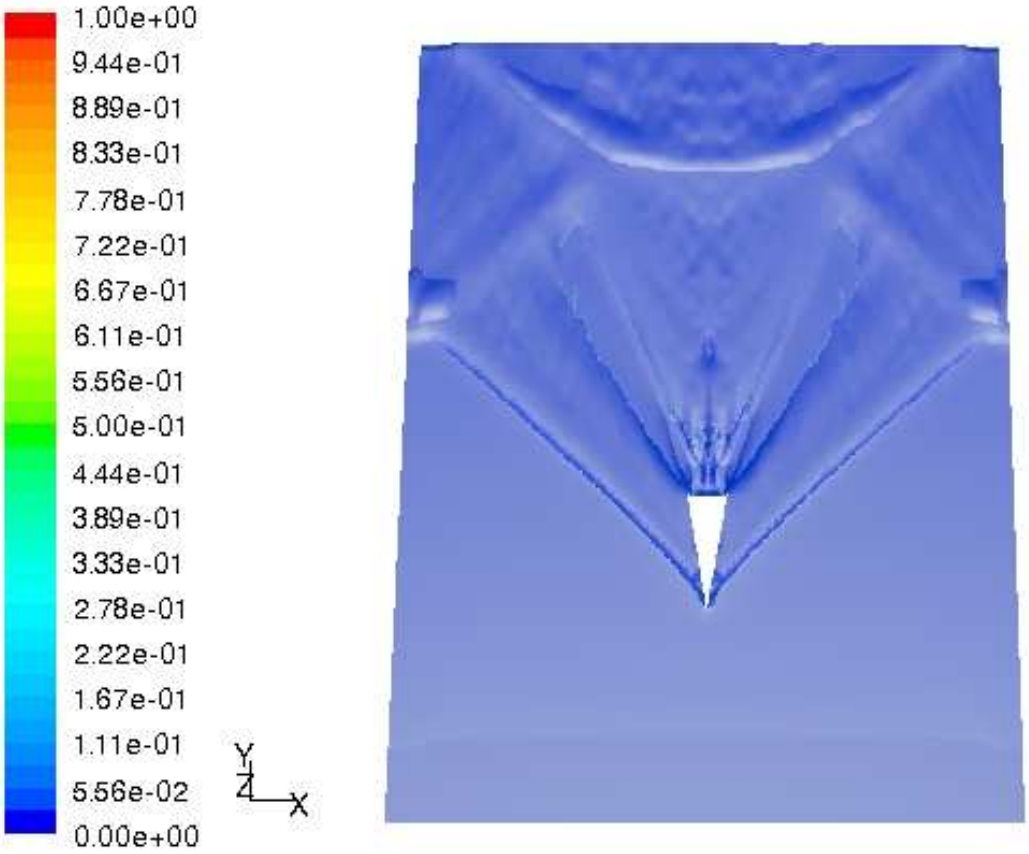

Figure H.2: VOF wall

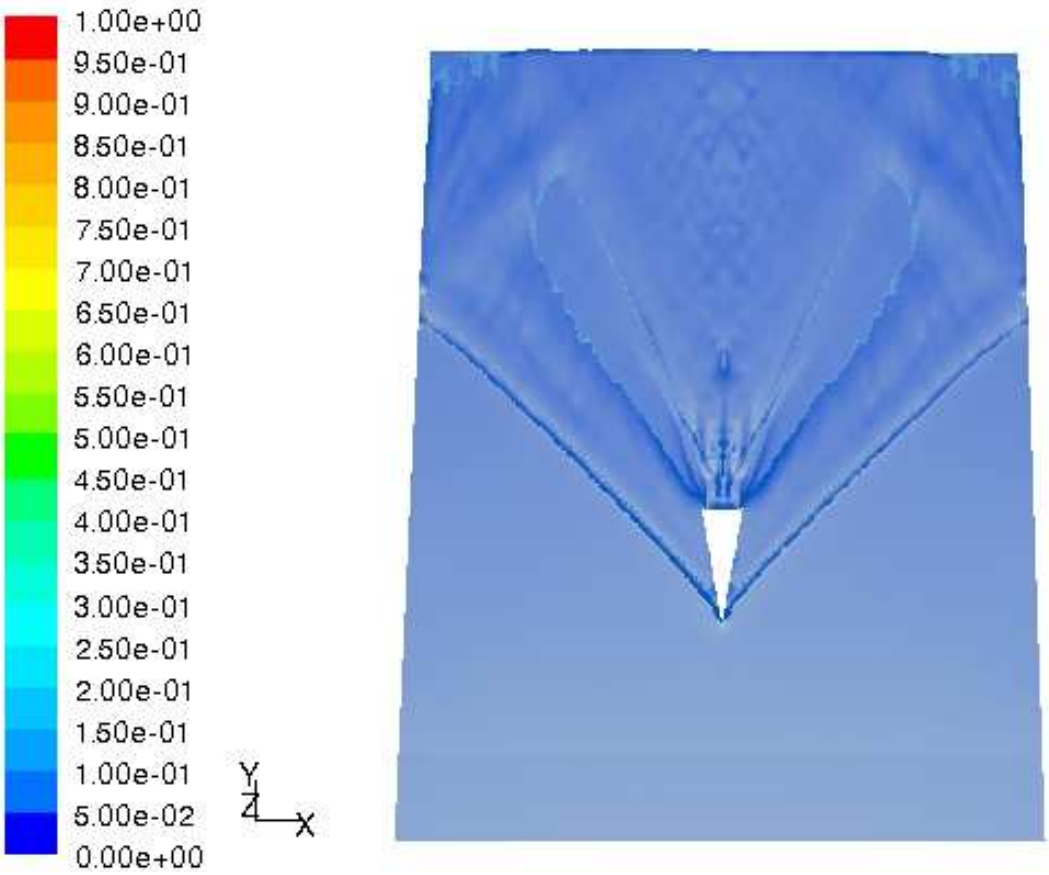

Figure H.3: VOF no wall

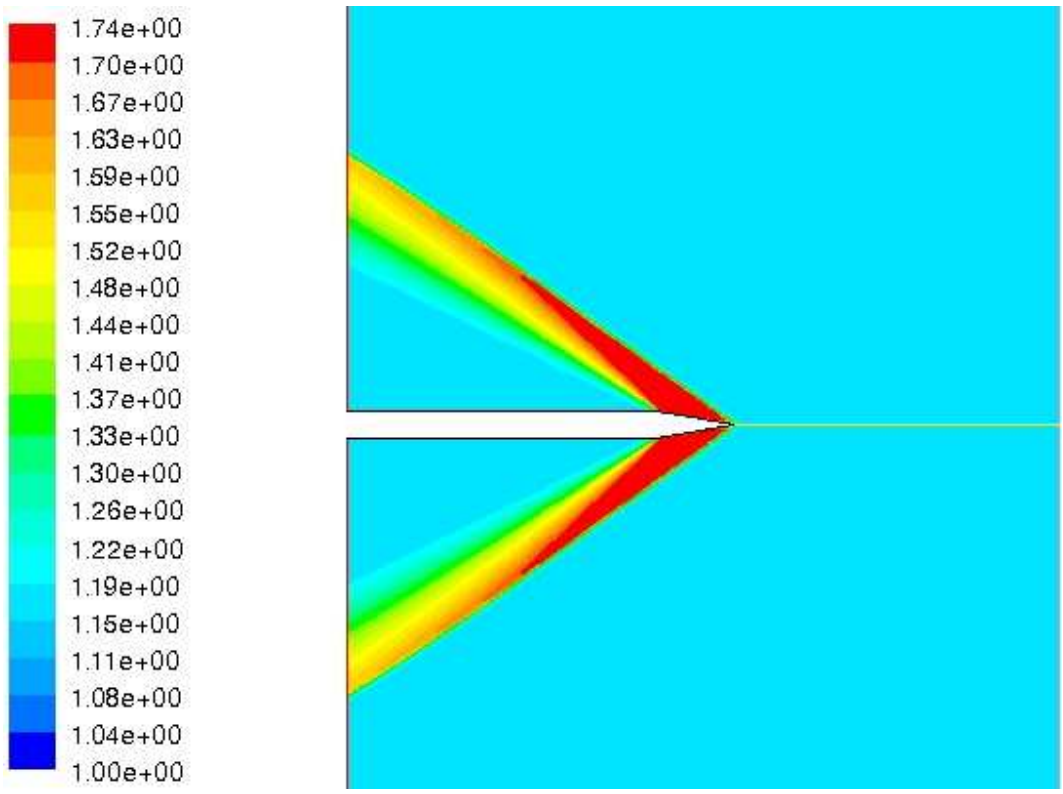

Figure H.4: Fictitious gas $\gamma = 2$

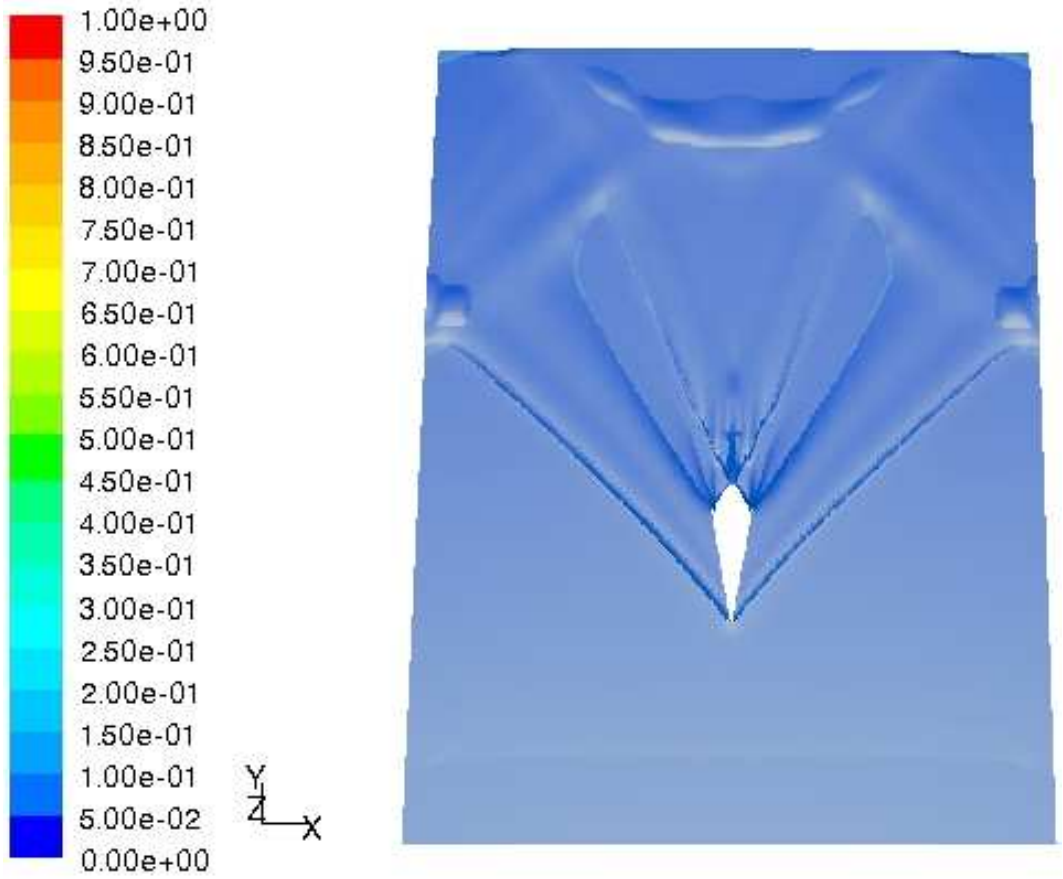

Figure H.5: VOF no surface tension no wall

H.2 Fr or M = 3.12

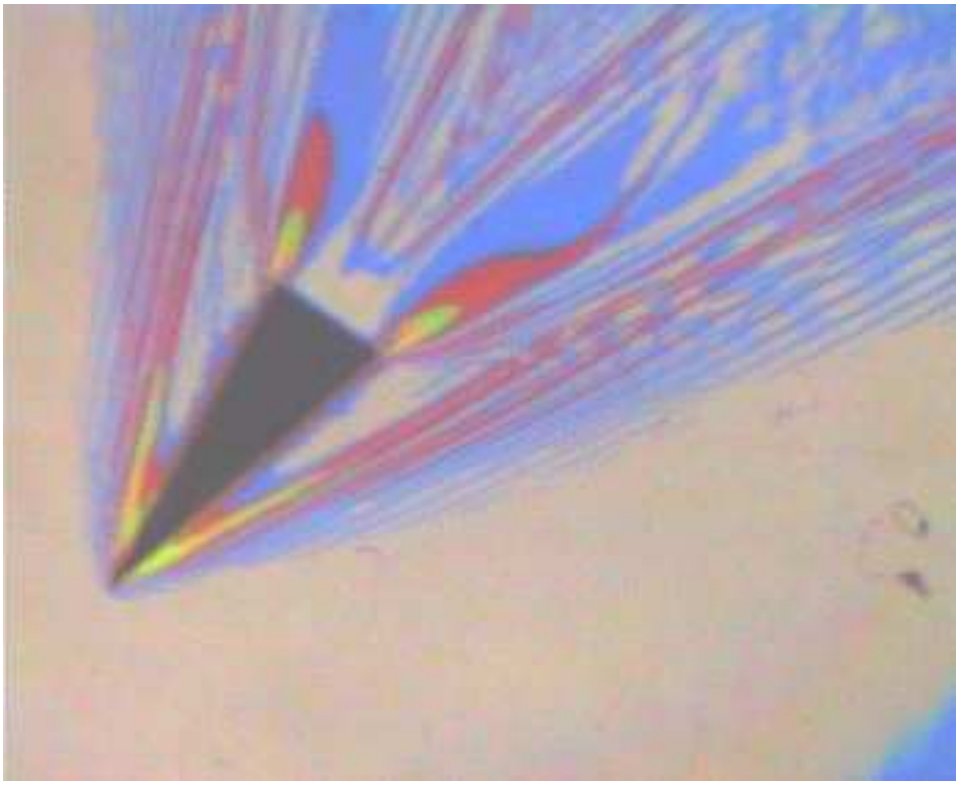

Figure H.6: Experimental

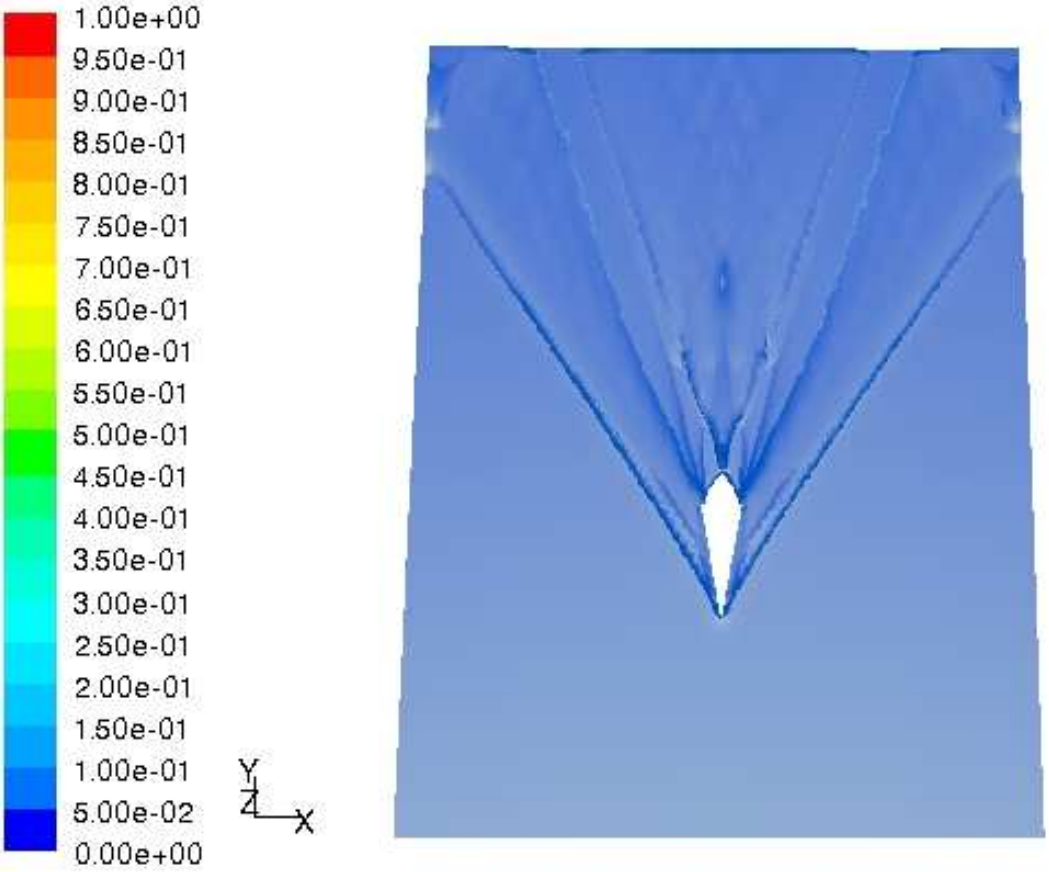

Figure H.7: VOF wall

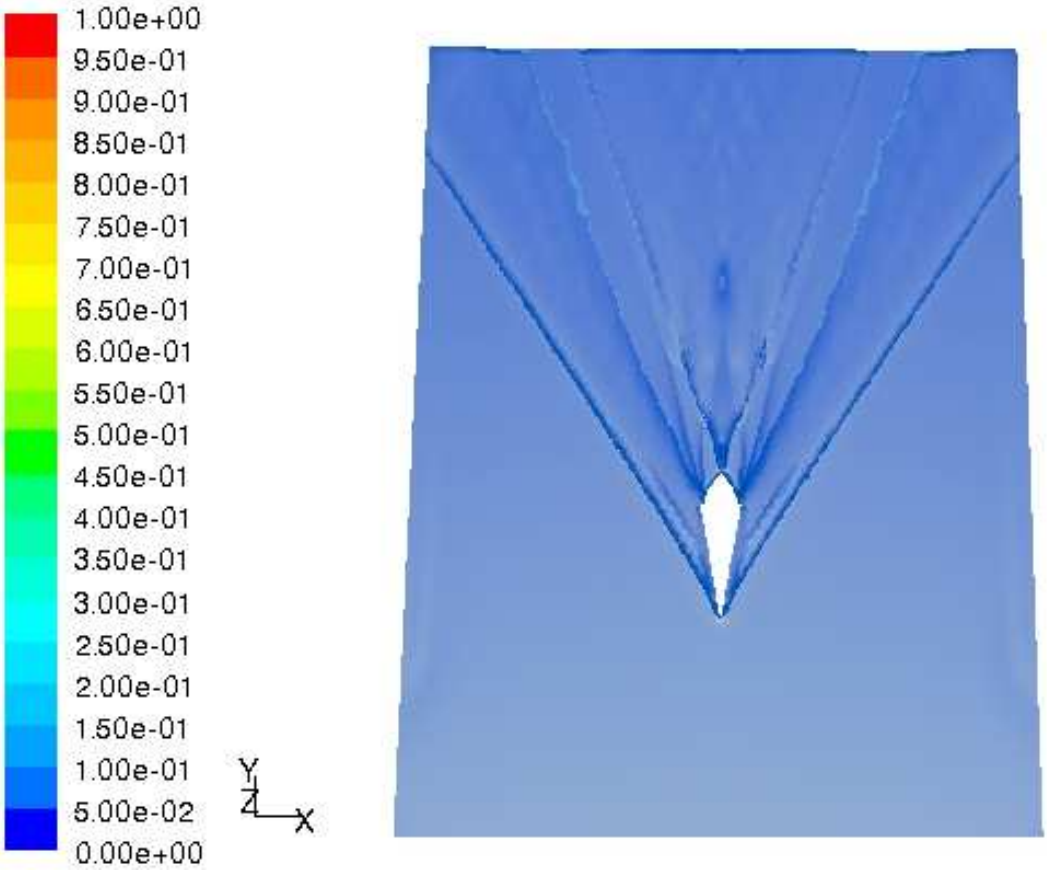

Figure H.8: VOF no wall

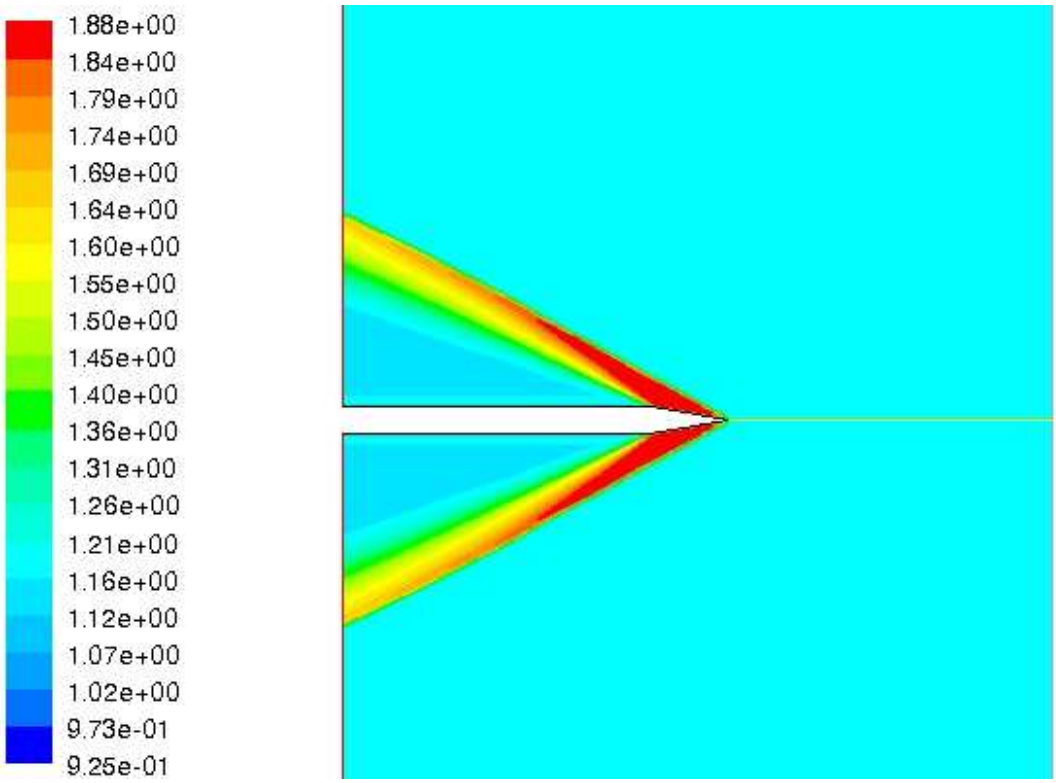

Figure H.9: Fictitious gas $\gamma = 2$

H.3 Fr or M = 4.31

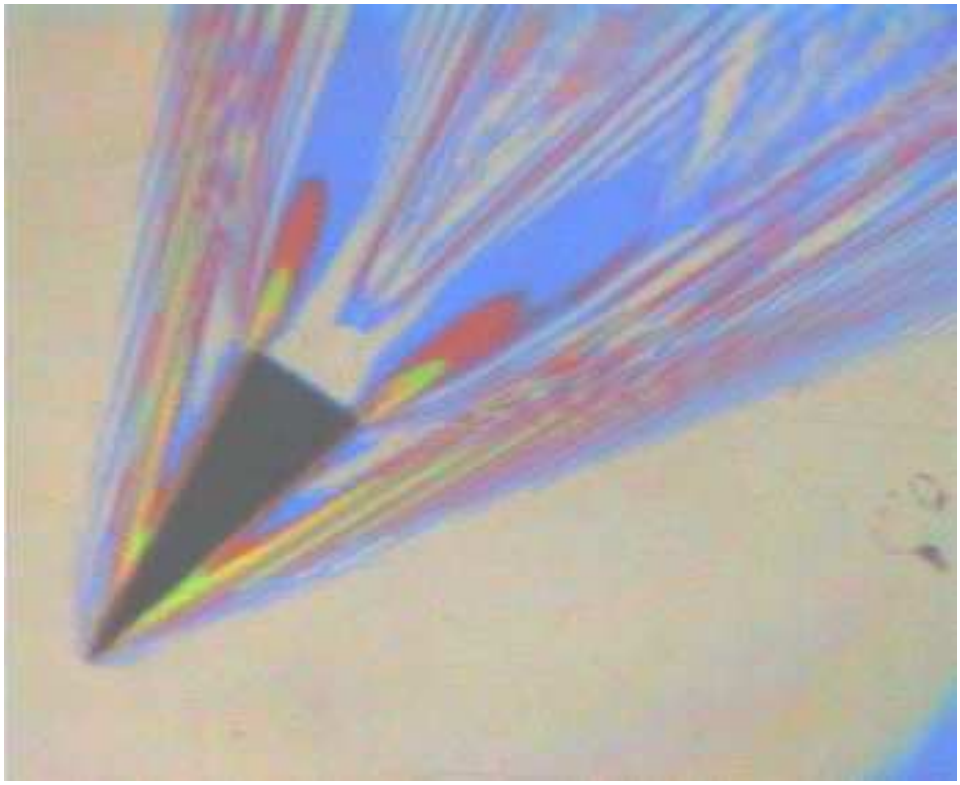

Figure H.10: Experimental Fr=4.31

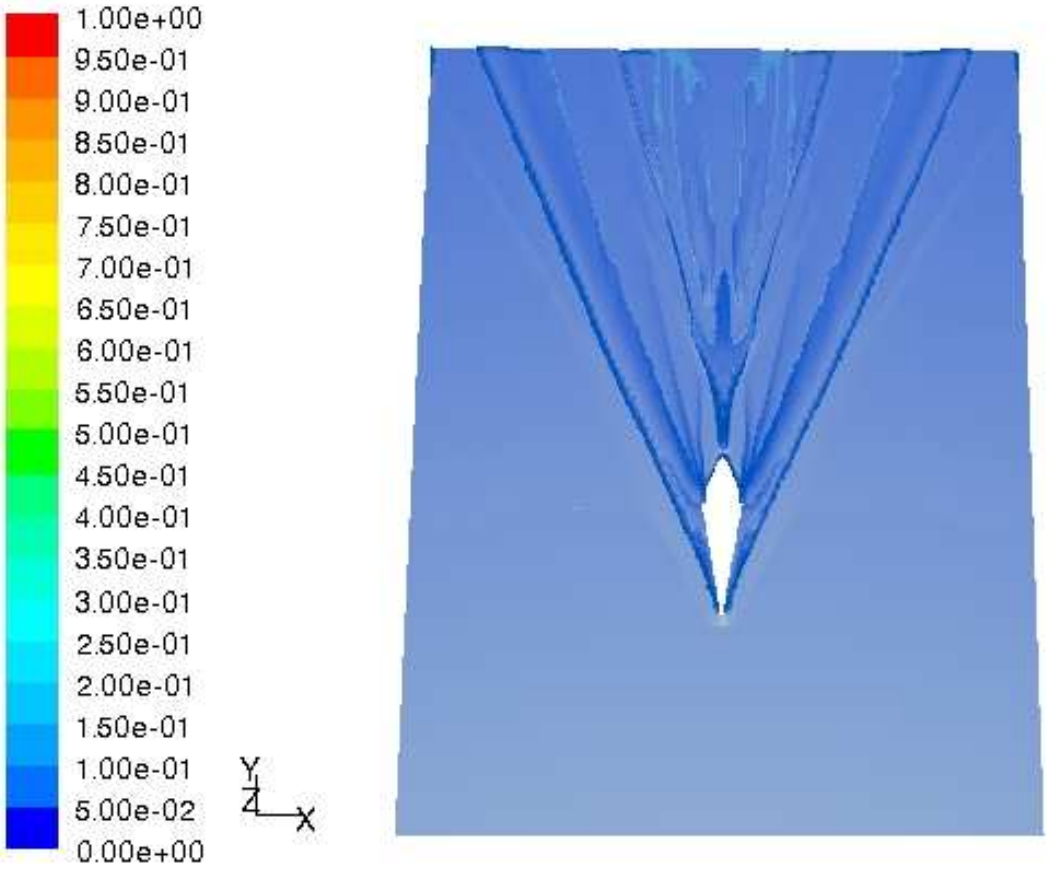

Figure H.11: VOF wall

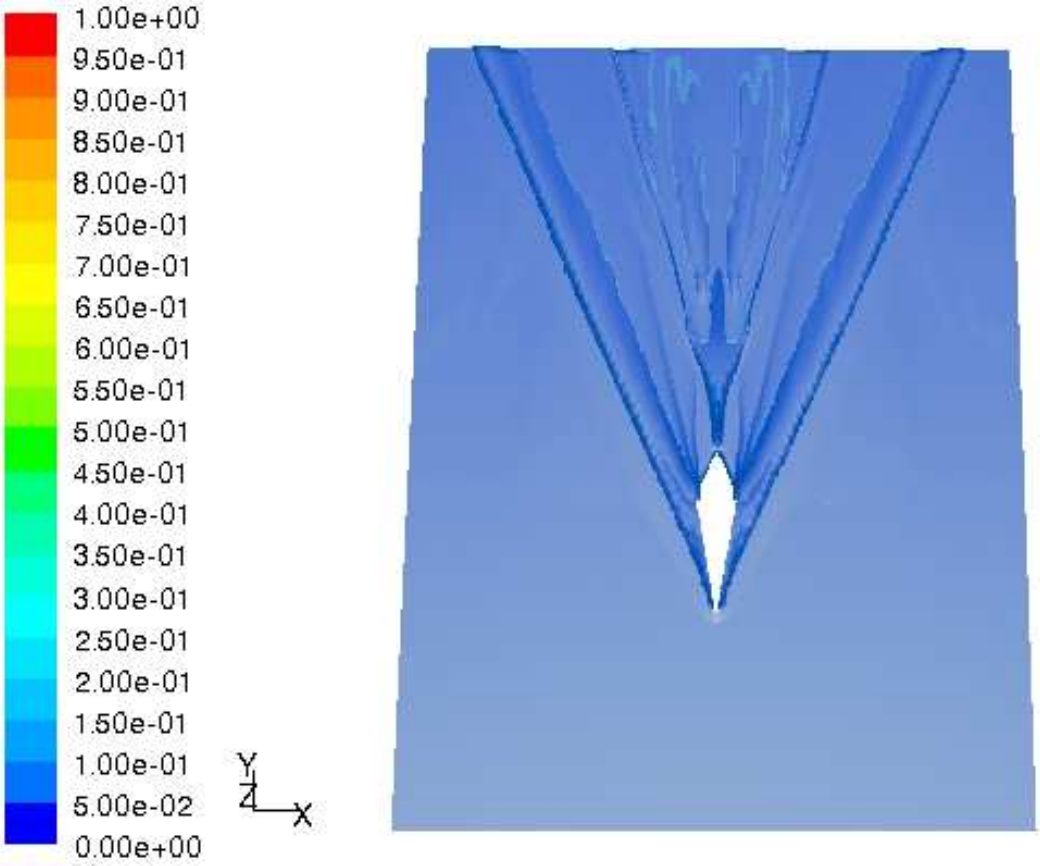

Figure H.12: VOF no wall

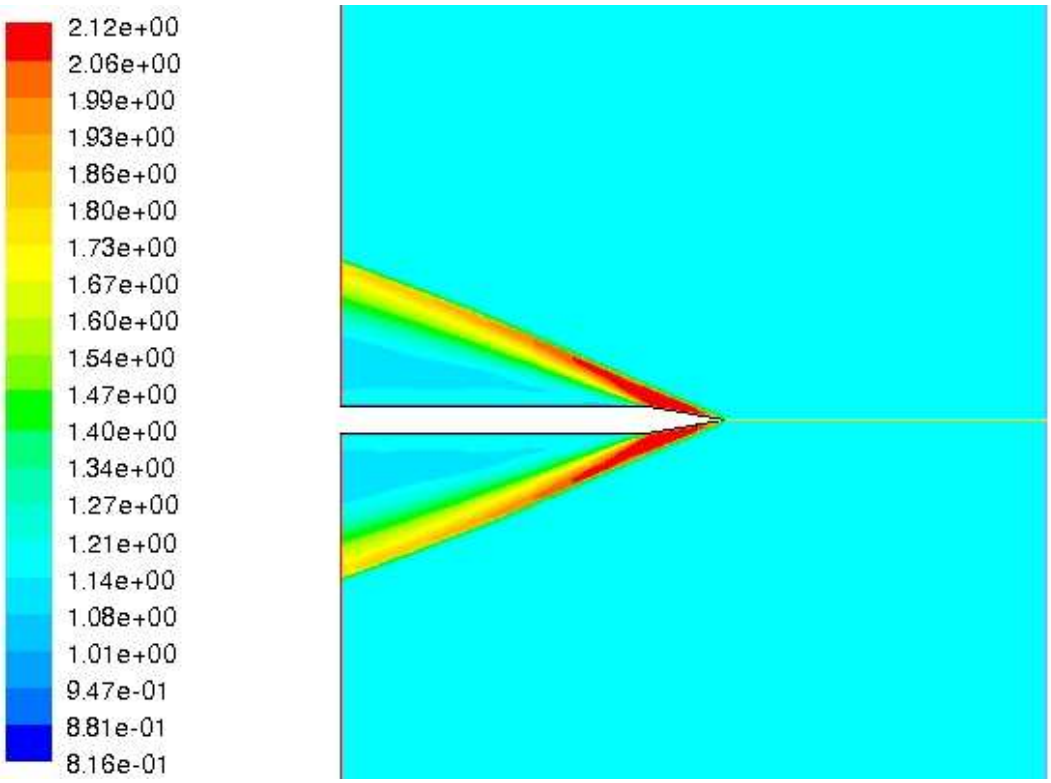

Figure H.13: Fictitious gas $\gamma = 2$

Appendix I

Animations

The naming conventions for animations on the CD are as follows:

- vf refers to the volume fraction and the number following it is the respective volume fraction, when one decimal place is moved to the right i.e. vf005 means a volume fraction of 0.05.
- filled and not filled refer to whether the contours are filled or not.
- For the same cases of volume fraction, but different colours/lighting/zoom, are differentiated by a letter at the end of the filename.

Otherwise filenames are self-explanatory.